Topological Interpretations of Open-Field Magnetic Helicity

DAINING XIAO

Topological Interpretations of Open-Field Magnetic Helicity

Daining Xiao

A thesis presented for the degree of
Doctor of Philosophy

Department of Mathematical Sciences
University of Durham

May 2024

Topological Interpretations of Open-Field Magnetic Helicity

Daining Xiao

Submitted for the degree of Doctor of Philosophy

May 2024

Abstract:

In ideal magnetohydrodynamics, magnetic helicity is a conserved dynamical quantity and a topological invariant closely related to Gauß linking numbers. However, for open magnetic fields with non-zero, normal boundary components, which are common in astrophysical settings, magnetic helicity is not uniquely defined and varies with the non-unique choices of the magnetic vector potentials or gauges.

An explicit interpretation of open-field magnetic helicity based on the entanglement of magnetic field lines has only been known for open Euclidean domains by Prior & Yeates (2014) *Astrophys. J.* 787 (2). In this thesis, this is proven to be generalisable to open spherical and periodic domains such that open-field magnetic helicity is equivalent to the total, flux-weighted winding of magnetic field lines, an intrinsic measure of magnetic topology. This is achieved by (i) formally constructing novel measures of spherical and periodic winding of open curves and (ii) identifying a particular gauge choice, called the winding gauge from the Hodge decomposition theorem on surfaces in the proof of the generalised poloidal-toroidal decomposition of magnetic fields. The theoretical findings are supplemented and confirmed by a numerical case study on solar observations.

The results obtained will contribute significantly to the field of topological fluid dynamics, by providing a novel topological interpretation to open-field magnetic helicity using the winding of magnetic field lines and the domain-specific generalised Green's functions for Laplacian. As open spherical and periodic domains are routinely used in the analytical modelling and numerical simulations for magnetically active regions, the geometry-adapted expressions can improve the modelling accuracy.

Contents

List of Figures

List of Tables

Declaration

The work in this thesis is based on research undertaken by the author in the Department of Mathematical Sciences at the University of Durham from October 2021 to March 2024. No part of this thesis has been submitted elsewhere for any degree or qualification.

Published Contents

This thesis contains materials from the following journal articles:

(i). D. Xiao, C. B. Prior, and A. R. Yeates (2023a). "Spherical winding and helicity". In: *J. Phys. A: Math. Theor.* 56, p. 205201

(ii). D. Xiao, C. B. Prior, and A. R. Yeates (2023b). "Computation of Winding-Based Magnetic Helicity and Magnetic Winding Density for SHARP Magnetograms in Spherical Coordinates". In: *Solar Phys.* 298, p. 116

(iii). D. Xiao, C. B. Prior, and A. R. Yeates (2024). "Winding and Magnetic Helicity in Periodic Domains". In: *(under review)*

In the above documents, I developed methodology and formalism, performed all analytical and numerical calculations, and wrote and edited the original manuscripts, under the supervision of Dr C. B. Prior and Professor A. R. Yeates.

Acknowledgement

First, I would like to express my sincerest gratitude to my supervisors, Chris Prior and Anthony Yeates, for their unwavering passion, encouragement, and support. In the past two and a half years, our weekly meetings have always been inspiring and enjoyable, even if we sometimes argued fiercely (in good faith). I must also thank John Sherwood (DAMTP, Cambridge) for his enthusiastic yet rigorous supervision classes from which I have greatly benefited since undergraduate years.

I thank my friends who have accompanied and motivated me throughout this journey, in particular I thank Bohan, Jiajie, Phoebe, Xiao, and Zihan. I am forever grateful to my parents and family for their steadfast love and generous support, for the past nine years in England and for my life to date. I am truly indebted to my Liyuan without whom I would not have been the person I am - you have always empowered me to explore the unknown fearlessly.

In the ancient cathedral city of Durham, it is the ultimate privilege to glimpse at the secrets of Creation by my heavenly Father.

He telleth the number of the stars;
He calleth them all by their names.
Great is our Lord, and of great power:
His understanding is infinite.

— Psalm 147 : 4-5

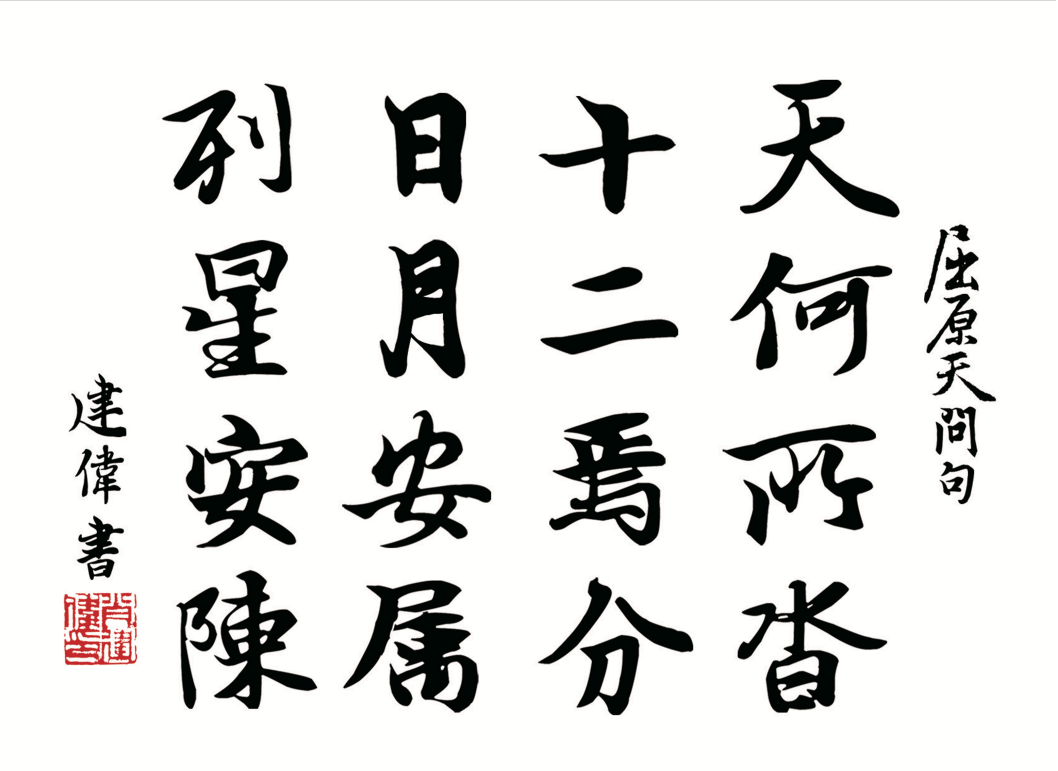

屈原天問句	Extracts from *Heavenly Questions*[a] by Qu Yuan (c.340 BC - 278 BC)
天何所沓	On what rests Heaven above?
十二焉分	How did twelve hours divide?
日月安屬	And Sun and Moon shed rays?
列星安陳	And stars in fine arrays?
建偉書（章）	Calligraphy by Jianwei[b] (Seal)

[a] Translated by Yuanchong Xu (許淵沖, 1921 - 2021)
[b] a.k.a. my Dad

Chapter 1

Introduction

This chapter presents the general background information for this thesis. In §1.1, we highlight key events in the historic development of our scientific understanding of magnetism. In §1.2, we introduce the equations governing ideal magnetohydrodynamics that describe the interaction between magnetic fields and fluid flows. In §1.3, we review the definitions and properties of magnetic helicity, the integral invariant that will be studied extensively herein. In §1.4, we provide an overview of this thesis.

1.1. Magnetism: A Historic Overview

> *Examining a person's words resembles using a magnet to attract an iron needle. (Original [a]: 其察言也不失，若磁石之取鍼。)*
>
> [a] See e.g., https://zh.wikisource.org/wiki/鬼谷子/卷01#反應第二
>
> — Guiguzi (鬼谷子) , c. 500 BC

In the History of Science Museum in Oxford sits an imposing stone surrounded by a gilt coronet, as shown in Figure 1.1(a). Known as "The Countess of Westmorland's Magnet", this enormous piece is reportedly (Kell 1996) capable of levitating objects with weight of 160 pounds without being in physical contact.

Such an example demonstrates the mystifying *magnetism*, which has been discovered and employed since antiquity (Stern 2002[1]). The ancient Greeks arguably coined the name "magnets" after the region of Magnesia (of modern Türkiye) where naturally occurring magnetic stones were found. The geomagnetic compass (Figure 1.1(b)), which in its primitive form is a freely-rotating, magnetised iron needle, is now believed to be first invented in ancient China between the first century BC and the second century AD (Needham 1959), enabling maritime navigation and contributing directly to the Age of Discovery.

The systematic scientific treatment of magnetism was initiated by the English natural philosopher William Gilbert (1544?-1603). In *De Magnete*, he surveyed the known theory of magnetism and argued that the Earth is a giant magnet (*terrella*). The French physicist Charles-Augustin de Coulomb (1736-1806) measured, using his torsional balance, that the strength of (static) magnetic forces was inversely proportional to the distance squared. The first direct link between magnetism and electricity was found by the Danish physicist Hans Christian Oersted (1777-1851), who observed the deflection of compass needles near a current carrying wire. The investigations were succeeded by the French physicists André-Marie Ampère (1775-1836), Jean-Baptise Biot (1774-1862), and Félix Savart (1791-1841) who proposed the governing equations for magnetic forces produced by electric currents (now called the *Ampère* and *Biot-Savart Laws*).

In 1831, Michael Faraday (1791-1867), an English scientist, discovered that momentary (electric) currents can be generated when a magnet passes through a coil (see e.g., Maxwell 1861), now known as *electromagnetic induction*. In explaining this phenomenon, he hypothesised the existence of invisible "lines of force" produced by the magnet in its surrounding space, as shown in Figure 1.1(c) by his iron-filing experiment. Faraday's revolutionary idea prompted the systematic study of magnetism as *magnetic fields*, himself coining the term "field" (Faraday 1852). That is, magnetic (and similarly electric) forces are exerted by the magnetic field generated from some source. Note that, however, the concept of fields, or force-at-a-distance, had been strongly objected to by Sir Isaac Newton (1643-1727).

The pinnacle of classical electromagnetism was achieved by the Scottish mathemati-

[1]Stern 2002 and references therein serve as a general source of reference for this section.

cian and physicist James Clerk Maxwell (1831-1879) in four simple equations (Maxwell 1865), shown in Figure 1.1(d). Maxwell's equations imply the unification of magnetic and electric fields into a single *electromagnetic field* from their identical speed of propagation. Such a speed was later found to coincide with that of light in vacuum, which led Maxwell to postulate that light is precisely electromagnetic fields. German physicist Heinrich Hertz (1857-1894) verified Maxwell's theory by experimentally producing radio waves[2], marking the start of telegraphy (see e.g. Buchwald 1994).

Into the twentieth century, Maxwell's theory largely inspired Albert Einstein (1879-1955) to formulate his special theory of relativity and its subsequent incorporation with electromagnetism (Einstein 1905b), or *electrodynamics*, based on the invariance of speed of light. Electrodynamics remains the definitive, classical theory of magnetism, and in particular magnetism is shown to be the relativistic effect of electricity. Meanwhile, the emerging quantum theory initiated by the German physicist Max Planck (1858-1947) led Einstein to explain the photoelectric effect from the particle nature of light (Einstein 1905a). This perspective was ultimately developed into *quantum electrodynamics* (QED), with Sin-Itiro Tomonaga (Japanese, 1906-1979), Julian Schwinger (American, 1918-1994), and Richard Feynman (American, 1918-1988) recognised as the main contributors in the Nobel Prize for physics in 1965 (Nobel Prize Outreach AB 2024). Nowadays, QED is the latest and most successful theory for the dynamics of photons and electrons, with electromagnetic fields (or more precisely their potential fields) understood as gauge fields.

[2]low-frequency electromagnetic waves

Figure 1.1: (a) The Countess of Westmorland's Magnet, c. 1728. [Courtesy of History of Science Museum, University of Oxford] (b) Painted Pottery Figurine Holding a Geomagnetic Compass, c. 960-1279. [Fuzhou Museum Archives, Jiangxi Province, China] (c) An iron-filing diagram created by Faraday, demonstrating magnetic lines of force, c. 1929. [Wellcome Trust Corporate Archive] (d) Plate showing Maxwell Equations affixed to the statue of James Clerk Maxwell in Edinburgh.

1.2. Magnetic Fields in Electrically Conducting Fluids

> How could a rotating body such as the Sun become a magnet?[a]
>
> [a] *Report for the British Association for the Advancement of Science*, 1919, pp. 159-160
>
> — Joseph Larmor (1857-1942)

Magnetic fields can exist not only in free space, but also in any macroscopic media such as electrically conducting fluids such as liquid metal or ionised gas (or plasma). Two examples of the latter scenario are illustrated in Figure 1.2; Aurora Borealis (or Northern lights) caused by charged particles interacting with geomagnetic fields within the atmosphere, and coronal loops generated by solar magnetic fields in the photosphere (lower solar atmosphere). Also, the answer to Larmor's opening quote, i.e., the origin and maintenance of solar magnetic fields, also rely on the magneto-hydrodynamics (MHD) of the solar interior, a branch called dynamo theory (see e.g., Moffatt and Dormy 2019). Furthermore, one of the most promising approaches of achieving artificial nuclear fusion is to confine strong magnetic fields in ultra-hot plasma (see e.g., Sheffield 1994).

The classical description of magnetic fields in electrically conducting fluids is often depicted by a set of nonlinear partial differential equations, known as the *ideal magneto-hydrodynamics equations*. These were pioneered in the 1940s by Swedish physicist Hannes Alfvén (1908-1995) in studying electromagnetic-hydrodynamic waves (Alfvén 1942), now called "Alfvén waves" in his honour. Treating the bulk fluids as a single-species, inviscid continuum with density ρ, pressure p, velocity $\boldsymbol{u}$, specific entropy s, gravitational potential Φ, and magnetic field $\boldsymbol{B}$ (with vacuum permeability μ_0), the ideal MHD equations read as follows, (e.g., Ogilvie 2016; Priest 2014),

$$\frac{\partial \rho}{\partial t} + \boldsymbol{\nabla} \cdot (\rho \boldsymbol{u}) = 0 \,, \tag{1.1}$$

Figure 1.2: (Top) Aurora Borealis glowing in multiple hues captured on 10 May 2024 in Cambridge, UK. [Courtesy of Jingbiao Mei] (Bottom) Coronal loops made of superheated, magnetised plasma following a solar eruption, imaged in extreme ultraviolet on 15 January 2014 by Solar Dynamical Observatory; see also https://sdo.gsfc.nasa.gov/assets/gallery/movies/Lovelyloops_best.mpg for a movie. [NASA/SDO]

$$\rho\left(\frac{\partial \boldsymbol{u}}{\partial t}+\boldsymbol{u}\cdot\boldsymbol{\nabla}\boldsymbol{u}\right)=-\boldsymbol{\nabla}p-\rho\boldsymbol{\nabla}\Phi+\frac{1}{\mu_0}(\boldsymbol{\nabla}\times\boldsymbol{B})\times\boldsymbol{B}\,, \tag{1.2}$$

$$\frac{\partial s}{\partial t}+\boldsymbol{u}\cdot\boldsymbol{\nabla}s=0\,, \tag{1.3}$$

$$\frac{\partial \boldsymbol{B}}{\partial t}=\boldsymbol{\nabla}\times(\boldsymbol{u}\times\boldsymbol{B})\,, \tag{1.4}$$

$$\boldsymbol{\nabla}\cdot\boldsymbol{B}=0\,; \tag{1.5}$$

supplemented, if required, with some equation of state for s, Poisson[3]'s equation of gravitation for Φ, etc. The conservation of mass and momentum is respectively enforced by the continuity equation (1.1) and the Navier[4]-Stokes[5] equation (1.2), whereas equation (1.3) describes the adiabatic evolution of thermal energy. The effects of the magnetic field $\boldsymbol{B}$ manifest in the Lorentz[6] force term $(\boldsymbol{\nabla}\times\boldsymbol{B})\times\boldsymbol{B}/\mu_0$ in equation (1.2), the induction equation (1.4), as well as the solenoidal constraint (1.5) which prohibits the existence of magnetic monopoles.

Although ideal MHD equations can explain myriad phenomena, which are assumed throughout this thesis, they are not without limitations. First, the fluid may not be ideal, and more realistic models have to incorporate effects such as (i) non-zero fluid viscosity and/or magnetic diffusivity, (ii) non-adiabatic heating or cooling and (iii) MHD turbulence, etc. Second, ideal MHD equations assume Galilean or Newtonian mechanics, so any relativistic effect would invalidate the formulation, e.g., when fluid speed is of comparable magnitude to that of light, or there exists a strong gravitational field in the vicinity. Last but not least, the validity of the continuum hypothesis may be violated, e.g., when microscopic particles are not sufficiently collisional (when collision timescale comparable is to MHD timescale).

[3]Siméon Denis Poisson, French, 1781-1840
[4]Claude-Louis Navier, French, 1785-1836.
[5]George Stokes, Irish, 1819-1903.
[6]Hendrik Lorentz, Dutch, 1853-1928

1.3. Magnetic Helicity in Magneto-Hydrodynamics

My soul is an entangled knot,

Upon a liquid vortex wrought. [a]

[a] *A parody of Shelley as 'A Paradoxical Ode (1878)'*, quoted by Campbell, L. and Garnett, W., *The Life of James Clerk Maxwell*, 1882, pp. 649-650, Cambridge University Press

— James Clerk Maxwell (1831-1879)

A higher level of non-linearity is displayed in ideal MHD equations, (1.1)-(1.5), through the feedback process between the fluid and magnetic fields (fluid advection of magnetic fields and magnetic forces exerted on the bulk fluid). Thus, it is essential to study symmetries and conservation laws to obtain understanding of such systems. One important dynamical invariant is the *(magnetic) helicity*[7],

$$H(\boldsymbol{B}) \equiv \int_V \boldsymbol{A} \cdot \boldsymbol{B} \, \mathrm{d}V \,, \tag{1.6}$$

first discovered in Woltjer 1958; see e.g., §3.1.1 of Moffatt and Dormy 2019 or §6.4.1 for a proof of its conservation. Here, $\boldsymbol{A}$ is some *vector potential* for $\boldsymbol{B}$ such that

$$\boldsymbol{B} = \boldsymbol{\nabla} \times \boldsymbol{A} \,, \tag{1.7}$$

whose existence is guaranteed by the Poincaré[8] Lemma[9] for a simply-connected Euclidean domain $V \subset \mathbb{E}^3$; this will be assumed henceforth in this chapter. An analogous invariant for ideal barotropic fluid was established in Moreau 1961, the *kinetic helicity*

$$H(\boldsymbol{u}) \equiv \int_V \boldsymbol{u} \cdot \boldsymbol{\omega} \, \mathrm{d}V \,, \tag{1.8}$$

where $\boldsymbol{\omega} = \boldsymbol{\nabla} \times \boldsymbol{u}$ is the fluid vorticity.

Note that in resistive, or non-ideal, MHD evolution helicity $H(\boldsymbol{B})$ often remains con-

[7] The term "helicity" was coined in Moffatt 1969 inspired by its use in particle physics.
[8] Henri Poincaré, French, 1854-1912.
[9] See cf. equations (4.8)-(4.9) in §4.1.2.

served to a good approximation as long as resistivity is small and/or localised (Berger 1993). Further, Kudryavtseva 2016 and Enciso, Peralta-Salas, and Lizaur 2016 showed, respectively, that helicity, magnetic or kinetic, is the only[10] regular integral invariant with, respectively, a continuous derivative in the C^1-topology and of volume-preserving transformations of the underlying domain. As applications, helicity has been widely used in solar physics in modelling and predicting solar eruptions (see e.g., Berger 1999; also Figure 1.2) and in understanding the mechanisms of MHD turbulence (see e.g., Biskamp 2003).

1.3.1. Gauge Dependence of Open-Field Helicity

Given any scalar field χ, the *gauge transformation*,

$$\boldsymbol{A} \mapsto \boldsymbol{A}' \equiv \boldsymbol{A} + \boldsymbol{\nabla}\chi \,, \tag{1.9}$$

yields another admissible vector potential $\boldsymbol{A}'$ for $\boldsymbol{B}$, i.e.,

$$\boldsymbol{B} = \boldsymbol{\nabla} \times \boldsymbol{A}' = \boldsymbol{\nabla} \times \boldsymbol{A} \,, \tag{1.10}$$

but helicity $H(\boldsymbol{B})$ in general acquires an extra boundary integral since

$$H(\boldsymbol{B}) \mapsto H(\boldsymbol{B}) + \int_V \boldsymbol{\nabla}\chi \cdot \boldsymbol{B} \, \mathrm{d}V \tag{1.11}$$

$$= H(\boldsymbol{B}) + \int_V \boldsymbol{\nabla} \cdot (\chi \boldsymbol{B}) \, \mathrm{d}V \tag{1.12}$$

$$= H(\boldsymbol{B}) + \int_{\partial V} \chi \boldsymbol{B} \cdot \hat{\boldsymbol{n}} \, \mathrm{d}A \,, \tag{1.13}$$

where in the second and last equalities we respectively applied the solenoidal condition (1.5) and the divergence theorem (with $\hat{\boldsymbol{n}}$ being the unit outward unit normal on ∂V).

When

$$\boldsymbol{B} \cdot \hat{\boldsymbol{n}}\Big|_{\partial V} \equiv 0 \quad \text{for all } \boldsymbol{x} \in \partial V \,, \tag{1.14}$$

[10] i.e., any other invariant is a function of helicity.

we call V *(magnetically) closed* or $\boldsymbol{B}$ a *closed (magnetic) field* (with respect to V). In this case, the additional boundary integral in (1.13) vanishes and helicity $H(\boldsymbol{B})$ is invariant under any gauge transformation. Also, $H(\boldsymbol{B})$ then provides a lower bound for the magnetic energy,

$$E(\boldsymbol{B}) \equiv \int_V \frac{1}{2}|\boldsymbol{B}|^2 \, \mathrm{d}V \ , \tag{1.15}$$

via the Arnold inequality (Arnol'd 1974),

$$|H(\boldsymbol{B})| \leq q^{-1} E(\boldsymbol{B}) \, , \tag{1.16}$$

where q is a constant (with dimension $[\mathrm{L}]^{-1}$) determined from the scale, topology, and geometry of V.

By contrast, when V is *(magnetically) open* or $\boldsymbol{B}$ is an *open (magnetic) field* (with respect to V), i.e., when

$$\boldsymbol{B} \cdot \hat{\boldsymbol{n}}\Big|_{\partial V} \neq 0 \quad \text{for some } \boldsymbol{x} \in \partial V \, , \tag{1.17}$$

the value of helicity $H(\boldsymbol{B})$ is gauge dependent and can thus be arbitrary using different gauges. This has caused controversy since open fields are common in astrophysical settings, e.g., coronal magnetic fields that typically penetrate the photosphere, as shown in Figure 1.2(b). Hence, it is crucial to have alternative definitions of open-field helicity that are immune to gauge ambiguities. Before discussing possible resolutions, we first review the topological interpretation of closed-field helicity.

1.3.2. Topological Interpretation of Closed-Field Helicity

Arguably, the most striking property of ideal MHD equations (1.1)-(1.5) is the conservation of topological structures in $\boldsymbol{B}$. Alfvén 1943 proved that (also Alfvén 1950), now known as *Alfvén's theorem*, magnetic lines of force ($\boldsymbol{B}$*-lines*), or the integral curves of $\boldsymbol{B}$, are "frozen-in" to the bulk fluid. More precisely, the induction equation (1.4) implies that the evolutionary equation for $\boldsymbol{B}$-lines coincides with that for a material line element $\delta\boldsymbol{x}$, i.e.,

(see e.g., Ogilvie 2016 for a proof)

$$\frac{\mathrm{D}}{\mathrm{D}t}\left(\frac{\boldsymbol{B}}{\rho}\right) \equiv \frac{\partial}{\partial t}\left(\frac{\boldsymbol{B}}{\rho}\right) + \boldsymbol{u}\cdot\boldsymbol{\nabla}\left(\frac{\boldsymbol{B}}{\rho}\right) = \left(\frac{\boldsymbol{B}}{\rho}\right)\cdot\boldsymbol{\nabla}\boldsymbol{u}\,. \tag{1.18}$$

In Alfvén's own words (Alfvén 1943), this can be stated that

> " ... every motion (perpendicular to the field) of the liquid in relation to the [magnetic] lines of force is forbidden ... Thus the matter of the liquid is "fastened" to the [magnetic] lines of force ... "

In the closed-field case, magnetic configurations can have their helicity $H(\boldsymbol{B})$ preserved by Alfvén's theorem (Arnol'd 1974; Moffatt 1969). Provided that $\boldsymbol{B}$ is sufficiently localised, we can find its Coulomb or Biot-Savart gauge $\boldsymbol{A}^{\mathrm{C}}$, given by (see e.g., Cantarella, DeTurck, and Gluck 2001; Moffatt and Dormy 2019)

$$\boldsymbol{A}^{\mathrm{C}}(\boldsymbol{x}) \equiv \frac{1}{4\pi}\int_V \boldsymbol{B}(\boldsymbol{x}')\times\frac{\boldsymbol{x}-\boldsymbol{x}'}{|\boldsymbol{x}-\boldsymbol{x}'|^3}\,\mathrm{d}^3\boldsymbol{x}' \implies \boldsymbol{\nabla}\cdot\boldsymbol{A}^{\mathrm{C}} = 0\,, \tag{1.19}$$

which can be substituted in the defining equation (1.8) to give

$$H(\boldsymbol{B}) = \frac{1}{4\pi}\int_V\int_V \boldsymbol{B}(\boldsymbol{x})\cdot\boldsymbol{B}(\boldsymbol{x}')\times\frac{\boldsymbol{x}-\boldsymbol{x}'}{|\boldsymbol{x}-\boldsymbol{x}'|^3}\,\mathrm{d}^3\boldsymbol{x}'\mathrm{d}^3\boldsymbol{x}\,. \tag{1.20}$$

Written in this form, helicity $H(\boldsymbol{B})$ can be related to a fundamental topological invariant called the *Gauß*[11] *linking number*, first proposed in Gauß's 1833 notes (now published as Gauss 2011; see also Berger and Prior 2006; Ricca and Nipoti 2011). For a pair of closed curves C, C', the Gauß linking number $L^{\mathrm{G}}(C,C')$ is defined, in modern notations, as

$$L^{\mathrm{G}}(C,C') \equiv \frac{1}{4\pi}\oint_C\oint_{C'}\mathrm{d}\boldsymbol{x}\cdot\mathrm{d}\boldsymbol{x}'\times\frac{\boldsymbol{x}-\boldsymbol{x}'}{|\boldsymbol{x}-\boldsymbol{x}'|^3}\,. \tag{1.21}$$

Figure 1.3 illustrates examples of Gauß linking. Note that $L^{\mathrm{G}}(C,C')$ is always integer-valued and invariant under continuous, non-intersecting deformations of C and C'.

Comparing (1.21) with (1.20), closed-field helicity acquires the topological interpretation as the total, flux-weighted Gauß linking number of $\boldsymbol{B}$-lines (e.g., Moffatt and Dormy 2019;

[11] Carl Friedrich Gauß, German, 1777-1855

Moffatt and Ricca 1992), which holds in general gauges as closed-field helicity is invariant under gauge transformations. This was further generalised in Arnol'd 1974; Arnold and Khesin 1998 to include the case of ergodic $\boldsymbol{B}$-lines using asymptotic linking numbers, which are beyond the scope of this thesis. In the open-field case, however, such an interpretation becomes invalid as the Coulomb gauge $\boldsymbol{A}^{\mathrm{C}}$ fails to be a vector potential for $\boldsymbol{B}$ (Cantarella, DeTurck, and Gluck 2001). In this thesis, an analogous, topological interpretation will be proposed from choosing a suitable vector potential.

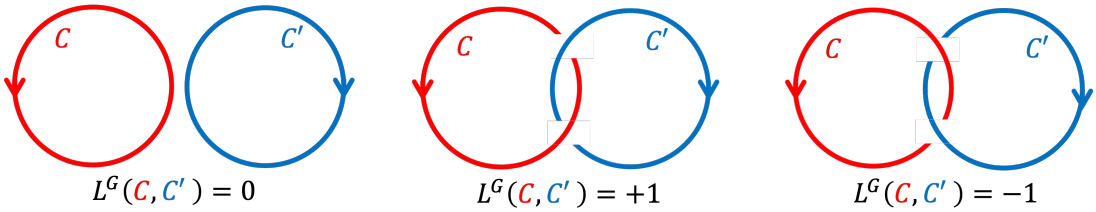

Figure 1.3: Examples of Gauß linking number $L^{\mathrm{G}}(C, C')$ for two circles C and C'.

1.3.3. Relative Magnetic Helicity

The most popular alternative for open-field helicity is *relative (magnetic) helicity*, first introduced by Berger and Field 1984, and its equivalent formulation by Finn and Antonsen 1985 will be reviewed below (see §2.2 of Prior and Yeates 2014 for a recent derivation).

For an open field $\boldsymbol{B}$ in some simply-connected Euclidean domain $V \subset \mathbb{E}^3$, let $\boldsymbol{B}_{\mathrm{ref}}$ be some reference magnetic field satisfying the matching boundary conditions on ∂V:

$$(\boldsymbol{B} - \boldsymbol{B}_{\mathrm{ref}}) \cdot \hat{\boldsymbol{n}}\Big|_{\partial V} = 0\,. \tag{1.22}$$

Then, relative helicity, written as the Finn-Antonsen formula, is defined by

$$H(\boldsymbol{B}; \boldsymbol{B}_{\mathrm{ref}}) \equiv \int_V (\boldsymbol{A} + \boldsymbol{A}_{\mathrm{ref}}) \cdot (\boldsymbol{B} - \boldsymbol{B}_{\mathrm{ref}})\, \mathrm{d}V\ , \tag{1.23}$$

where $\boldsymbol{A}$ and $\boldsymbol{A}_{\mathrm{ref}}$ are the respective vector potentials of $\boldsymbol{B}$ and $\boldsymbol{B}_{\mathrm{ref}}$. Note that, (1.23) is manifestly invariant of gauge transformations of both $\boldsymbol{A}$ and $\boldsymbol{A}_{\mathrm{ref}}$ given (1.22).

In astrophysical applications, the reference field is normally chosen to be the unique,

energy-minimising potential field $\boldsymbol{B}_{\mathrm{ref}} = \boldsymbol{B}_{\mathrm{p}}$ satisfying (1.22) on ∂V (see Démoulin 2007 for a review). However, there is no mathematically *a priori* argument for such a choice and the potential field is neither "static" nor "universal" as it evolves under the ideal MHD equations and its configuration can sometimes vary significantly given slightly different boundary conditions. This could render the potential field inappropriate for any time-series analysis (e.g., those in Thalmann, Dumbović, et al. 2023) or parametric study (e.g., those in Rice and Yeates 2023). Furthermore, the use of relative helicity lacks an explicit interpretation analogous to (1.20) which may be unable to quantify topological changes in the open-field case. All three limitations will be addressed in this thesis by an more intrinsic formulation of open-field helicity.

1.3.4. Topological Interpretation of Open-Field Helicity in Euclidean Domains

For *open* Euclidean domains foliated by infinite parallel planes, i.e.,

$$V_{\mathrm{E}} \equiv \mathbb{R}^2 \times [0,1]\,. \tag{1.24}$$

Berger 1985 proposed the first topological interpretation of open-field helicity. He showed that, for a given choice of $\boldsymbol{B}_{\mathrm{ref}}$, relative helicity $H(\boldsymbol{B};\boldsymbol{B}_{\mathrm{ref}})$ can be written into a topological form similar to (1.20); see later (1.27).

More generally, Prior and Yeates 2014 identified a (family of) vector potential in V_{E}, called the *winding gauge* and denoted $\boldsymbol{A}^{\mathrm{W}}$, that satisfies

$$\boldsymbol{\nabla}_S \cdot \boldsymbol{A}^{\mathrm{W}} = 0\,, \quad \text{where} \quad \boldsymbol{\nabla}_S \equiv (\partial_x, \partial_y, 0)\,, \tag{1.25}$$

on each planar surface at height w, $S_w \equiv \mathbb{R}^2 \times \{w\}$, using Cartesian coordinates (x, y, w). Substituting $\boldsymbol{A}^{\mathrm{W}}$ in (1.8) yields the *winding (magnetic) helicity*,

$$H^{\mathrm{W}}(\boldsymbol{B}) \equiv \int_{V_{\mathrm{E}}} \boldsymbol{A}^{\mathrm{W}} \cdot \boldsymbol{B}\, \mathrm{d}V\,, \tag{1.26}$$

which can be written as (see also Prior and MacTaggart 2020),

$$H^{\mathrm{W}}(\boldsymbol{B}) = \frac{1}{2\pi}\int_0^1 \int_{S_w}\int_{S_w} \boldsymbol{B}[\boldsymbol{x}(w)]\cdot\boldsymbol{B}[\boldsymbol{x}'(w)] \times \frac{\boldsymbol{x}(w)-\boldsymbol{x}'(w)}{|\boldsymbol{x}(w)-\boldsymbol{x}'(w)|^2}\,\mathrm{d}^2\boldsymbol{x}'\mathrm{d}^2\boldsymbol{x}\,\mathrm{d}w\ . \tag{1.27}$$

Note that for closed-domain boundary conditions, open-field winding helicity (1.27) reduces to (1.20) from gauge invariance and Theorem 2.1 in §2.3 (see also Berger and Prior 2006). Topologically, it is precisely the total, flux-weighted winding of $\boldsymbol{B}$-lines, an intrinsic quantity associated with the field configuration. To see this, for w-parameterised, non-intersecting curves $\boldsymbol{x}(w) = (x, y, w)$ and $\boldsymbol{x}'(w) = (x', y', w)$ in V_{E}, let ω_{E} be the *Euclidean winding rate* given by (see Chapter 2 for details)

$$\omega_{\mathrm{E}}(w;\boldsymbol{x},\boldsymbol{x}') \equiv \frac{\mathrm{d}}{\mathrm{d}w}\arctan\left(\frac{y-y'}{x-x'}\right) = \frac{(x-x')(\dot{y}-\dot{y}')-(\dot{x}-\dot{x}')(y-y')}{(x-x')^2+(y-y')^2}\,, \tag{1.28}$$

where $\dot{(\,)} \equiv \mathrm{d}/\mathrm{d}w$. Using this, (1.27) can be further simplified to, writing $B_w \equiv \hat{\boldsymbol{e}}_w\cdot\boldsymbol{B}$,

$$H^{\mathrm{W}}(\boldsymbol{B}) = \frac{1}{2\pi}\int_0^1 \int_{S_w}\int_{S_w} \omega_{\mathrm{E}}[w;\boldsymbol{x}(w),\boldsymbol{x}'(w)]B_w(\boldsymbol{x})B_w(\boldsymbol{x}')\,\mathrm{d}^2\boldsymbol{x}'\mathrm{d}^2\boldsymbol{x}\,\mathrm{d}w\ . \tag{1.29}$$

In addition, the canonical status of $\boldsymbol{A}^{\mathrm{W}}$ among all possible vector potentials in V_{E} has been argued from variational principles (Yeates 2020; Yeates and Page 2018). Also, the use of winding helicity was extended to open Euclidean tubular domains that are homeomorphic to V_{E} (Prior and Yeates 2021).

1.4. Thesis Outline

This thesis generalises the topological interpretation of open-field magnetic helicity from Euclidean domains (cf. §1.3.4) to spherical and periodic domains. That is, in all three of open Euclidean, spherical, and periodic domains, the winding magnetic helicity $H^{\mathrm{W}}(\boldsymbol{B}) \equiv \int_V \boldsymbol{A}^{\mathrm{W}}\cdot\boldsymbol{B}\,\mathrm{d}V$ is equivalent to the total, flux-weighted winding of $\boldsymbol{B}$-lines (see Theorem 6.1 in Chapter 6). Before proving this, two fundamental results are first established:

(i). Novel winding measures of open curves are constructed for both spherical domains in Chapter 3 and periodic domains in Chapter 4, based on a comprehensive review and

formalisation of Euclidean winding quantities in Chapter 2.

(ii). The winding gauge $\boldsymbol{A}^{\mathrm{W}}$ is identified from a new proof of the generalised poloidal-toroidal decomposition of magnetic fields in Chapter 5, using the Hodge decomposition theorem on surfaces for magnetic vector potentials.

In Chapter 7, spherical winding magnetic helicity is applied to solar observations (SHARP magnetograms), which confirms quantitatively the impact of spherical curvature on helicity computation. Chapter 8 gives possible directions for future works and concludes the thesis.

For reference, the organisation of this thesis is summarised in Figure 1.4.

Figure 1.4: Organisation of this thesis.

Chapter 2

Winding of Open Curves in Euclidean Domains

This chapter introduces one of the central concepts of this thesis, winding of open curves, in the familiar Euclidean domains to prepare readers for its generalisation to spherical domains (Chapter 3) and periodic domains (Chapter 4). §2.1 surveys the definitions and representations of angles and angular velocities (or winding rates) in two dimensions as well as the mathematical techniques involved. A formal construction of the Euclidean winding rates of open curves is provided in §2.2[1] from both the Euclidean winding coordinates and Green's functions for Laplacians. We summarise, in §2.3, existing results on Euclidean winding numbers of curves including its relationship with Gauß linking numbers and its topological invariance.

[1]Adapted from Chapter 4, D. Xiao, C. B. Prior, and A. R. Yeates (2023a). "Spherical winding and helicity". In: *J. Phys. A: Math. Theor.* 56, p. 205201.

2.1. Angular Velocity in Two Dimensions

2.1.1. Angles & Planar Polar Coordinates

The concept of *angles* is one of the most ancient in mathematics. In two-dimensional Euclidean geometry, an angle is formed by two rays, or *sides*, that share a common endpoint, or *vertex*. The *angular measure* or *size* of an angle can be defined statically against a circle whose centre coincides with the vertex. As shown in Figure 2.1(a), the size of the angle AOB, in the units of degrees, is

$$\theta \equiv \frac{\overset{\frown}{AB}}{2\pi r} \times 360^\circ \,, \tag{2.1}$$

or equivalently, in the units of radians (assumed henceforth), as

$$\theta \equiv \frac{\overset{\frown}{AB}}{r} = \frac{\overset{\frown}{AB}}{2\pi r} \cdot 2\pi \text{ rad} \,, \tag{2.2}$$

where r is the (arbitrary) radius of the circle O and $\overset{\frown}{AB}$ is the shorter arclength of AB. Note that in the definitions (2.1) or (2.2), the angular measure has a limited range, namely, $\theta \in [0, 360^\circ]$ or $[0, 2\pi]$.

Alternatively, an angle can be defined dynamically as the object formed by rotating some initial ray about its endpoint, or *centre of rotation*, to a final position about a positive direction (usually anticlockwise). This allows the angular measure to be any real number, as illustrated in Figure 2.1(b). If the rotational process is unknown then ambiguity also arises since an angle θ will be indistinguishable from $\theta + 2k\pi$ for any integer k.

Practically, neither is useful in determining angles, which has, since antiquity, led to the concepts of *trigonometric functions*. Trigonometric functions relate angles to ratios of lengths that are measured more easily, and they are classically defined using a unit circle centred at the origin of a Cartesian coordinate system with coordinates (x, y), as shown in Figure 2.2(a).

Conversely, the inverses to the trigonometric functions, in particular a version of the

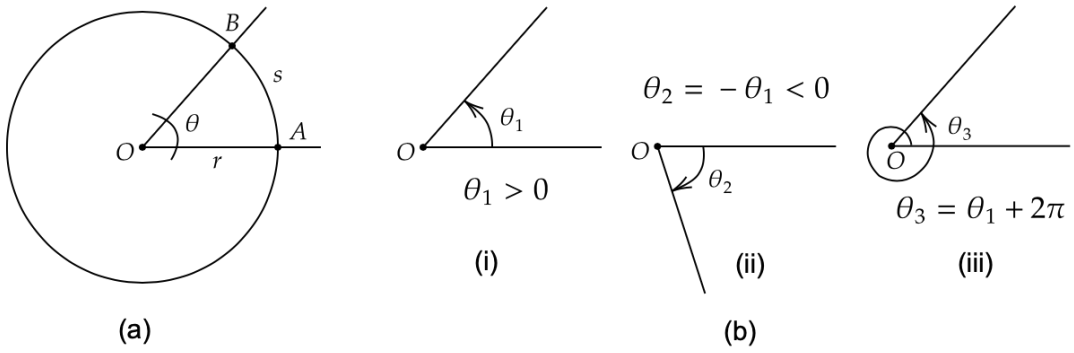

Figure 2.1: (a). Static and (b). dynamic definitions of angular measures.

inverse tangent function, can represent the *(polar) angle* θ of a point with respect to a reference direction (OA) and a reference point (O), i.e.,

$$\theta \equiv \texttt{atan2}(y, x) \iff \begin{cases} x = \cos\theta\,, \\ y = \sin\theta\,. \end{cases} \tag{2.3}$$

The relative difficulty in defining (2.3) is no coincidence due to the restricted range of the usual $\arctan$ function, hinting at the advantage of re-defining θ from its differential $\mathrm{d}\theta$, which will be a recurring theme of this thesis. Nevertheless, (2.3) allows the conversion between Cartesian coordinates (x, y) and *polar coordinates* (r, θ), shown in Figure 2.2(b), and the latter are more convenient in describing rotational motions, or *winding*.

2.1.2. Angular Velocity — Four Representations

For a particle moving in two dimensions with trajectory $\boldsymbol{x}(t) = (r(t), \theta(t)) \neq \mathbf{0}$ in polar coordinates, the temporal rate of change of its polar angle, or more commonly known as its *angular velocity*, is defined as

$$\omega \equiv \frac{\mathrm{d}\theta}{\mathrm{d}t}\,, \tag{2.4}$$

which is independent of its radial coordinate r. In this thesis, we also refer to ω as the *(Euclidean) winding rate* (up to a sign, see later in §2.2), since it measures how rapidly the particle winds or rotates about the origin.

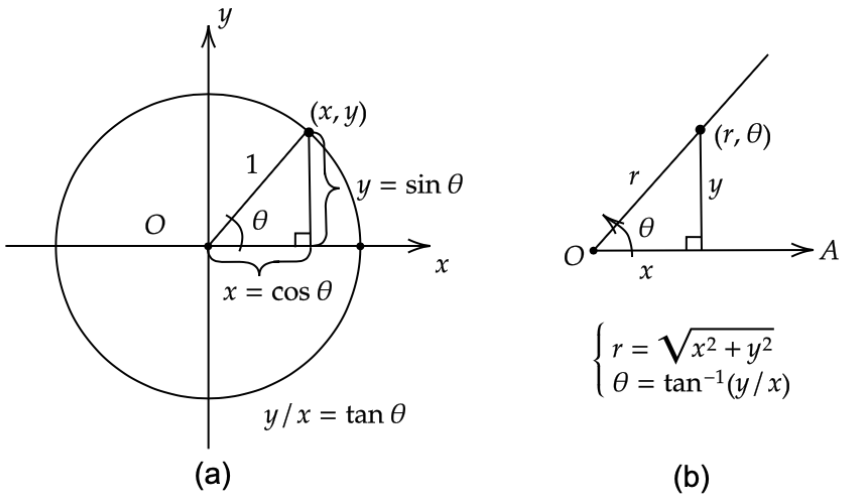

Figure 2.2: (a) Definitions of common trigonometric functions using a unit circle and (b) polar coordinates (r, θ) from Cartesian coordinates (x, y), showing the origin O and the initial line OA.

The definition (2.4) of angular velocity ω can also be computed if the particle's path is expressed in some Cartesian coordinates, $\boldsymbol{x}(t) = (x(t), y(t)) \neq \mathbf{0}$. Using the transformation rule (2.3), it follows that (see also Prior and MacTaggart 2020)

$$\omega = \frac{\mathrm{d}}{\mathrm{d}t}\left[\tan^{-1}\left(\frac{y}{x}\right)\right] = \frac{x\,\mathrm{d}y/\mathrm{d}t - y\,\mathrm{d}x/\mathrm{d}t}{x^2 + y^2}\,. \tag{2.5}$$

It is easy to check that (2.5) can be written coordinate-free by using vectors, i.e.,

$$\omega = \hat{\boldsymbol{e}}_w \cdot \frac{\boldsymbol{x}}{|\boldsymbol{x}|^2} \times \frac{\mathrm{d}\boldsymbol{x}}{\mathrm{d}t}\,, \tag{2.6}$$

where $\hat{\boldsymbol{e}}_w$ is the unit vertical[2] vector normal to the plane containing the particle's path.

A compact representation of ω can be obtained by identifying the particle's trajectory as a path in the complex plane, i.e., in the Euler or polar form as $z(t) = r(t)\mathrm{e}^{\mathrm{i}\theta(t)}$, given that $\theta(t)$ is defined continuously on a Riemann surface (see e.g., Conway 1978). Taking the complex logarithm of $z(t)$ and differentiating it with respect to t gives

$$\ln z(t) = \ln r(t) + \mathrm{i}\theta(t) \implies \frac{1}{z}\frac{\mathrm{d}z}{\mathrm{d}t} = \frac{1}{r}\frac{\mathrm{d}r}{\mathrm{d}t} + \mathrm{i}\frac{\mathrm{d}\theta}{\mathrm{d}t}\,. \tag{2.7}$$

[2]The use of the usual symbol z is henceforth reserved for that of a general complex variable.

It then follows by equating the imaginary part of both sides that (see e.g., Berger 1994),

$$\omega = \mathrm{Im}\left(\frac{1}{z}\frac{\mathrm{d}z}{\mathrm{d}t}\right). \tag{2.8}$$

Finally, it is also possible to derive (2.8) from the Cartesian representation (2.5) using the Cartesian form of the complex variable $z(t) = x(t) + \mathrm{i}y(t)$. Note that

$$\bar{z}\frac{\mathrm{d}z}{\mathrm{d}t} = (x - \mathrm{i}y)\left(\frac{\mathrm{d}x}{\mathrm{d}t} + \mathrm{i}\frac{\mathrm{d}y}{\mathrm{d}t}\right) = \left(x\frac{\mathrm{d}x}{\mathrm{d}t} + y\frac{\mathrm{d}y}{\mathrm{d}t}\right) + \mathrm{i}\left(x\frac{\mathrm{d}y}{\mathrm{d}t} - y\frac{\mathrm{d}x}{\mathrm{d}t}\right), \tag{2.9}$$

and since $|z|^2 = z\bar{z} = x^2 + y^2$, we have, by comparing with (2.5),

$$\omega = \frac{1}{|z|^2}\,\mathrm{Im}\left(\bar{z}\frac{\mathrm{d}z}{\mathrm{d}t}\right) = \mathrm{Im}\left(\frac{1}{z}\frac{\mathrm{d}z}{\mathrm{d}t}\right). \tag{2.10}$$

2.1.3. Angles Revisited & Winding Number

Using any of the representations of the angular velocity ω of a moving particle from $t = 0$ along some smooth path, we can define the *(cumulative) angular change* $\Delta\theta$ as

$$\Delta\theta(t) \equiv \int_0^t \omega(\tilde{t})\ \mathrm{d}\tilde{t}\ . \tag{2.11}$$

Given some initial angle $\theta(0)$, the total angle is thus

$$\theta(t) = \theta(0) + \Delta\theta(t)\,, \tag{2.12}$$

if defined continuously. In the case when $\Delta\theta(t)$ is confined to the range of principal argument $[-\pi, \pi)$, (2.12) can be equivalently written as

$$\theta(t) = \theta(0) + \Delta\theta(t) + 2\pi N(t)\,, \tag{2.13}$$

where $N(t)$ is an integer called the *(net) winding number* measuring the (signed) number of times the particle winds around the origin (see e.g., Conway 1978, also for subsequent discussions on complex analysis). Such a (re-)definition of winding angles accounts for

the particle's full trajectory and it is also numerically easier to compute without needing to adjust for branch cuts.

The winding number $N(t)$ is crucial to complex analysis and to complex integration in particular. Define $N(\gamma; z_0)$ as the total winding number of a closed contour γ around $z = z_0$. A fundamental result is that

$$\oint_{C_\epsilon} \frac{\mathrm{d}z}{z} = 2\pi\mathrm{i}\,, \quad \text{where} \quad C_\epsilon : t \in [0,1] \mapsto \epsilon \mathrm{e}^{2\pi\mathrm{i}t}\,. \tag{2.14}$$

That is, winding anticlockwise once around $z = 0$ (a simple pole) generates a winding number of $N(C_\epsilon, 0) = +1$. This can be used to prove the *residue theorem*: the contour integral of a meromorphic function $f(z)$ over a closed contour γ is given by

$$\oint_\gamma f(z)\,\mathrm{d}z = 2\pi\mathrm{i} \sum_{k=1}^{n} \mathrm{Res}(\gamma; z_k)\,, \tag{2.15}$$

where $z_1, \cdots, z_k$ are the poles of f inside γ and $\mathrm{Res}(f; z_k)$ is the *residue* of f at $z = z_k$ defined as

$$\mathrm{Res}(f; z_k) \equiv \frac{1}{2\pi\mathrm{i}} \int_{C_\epsilon} f(z)\,\mathrm{d}z\,, \quad \text{where } C_\epsilon : t \in [0,1] \mapsto z_k + \epsilon \mathrm{e}^{2\pi\mathrm{i}t},\ \epsilon \to 0\,. \tag{2.16}$$

2.2. Euclidean Winding Rates

In §2.2.1, the concept of winding coordinates in Euclidean domains is developed to derive the angular velocity in two dimensions, or Euclidean winding rates. Also, we review, in §2.2.2, the link between the Euclidean winding rates and the Green's functions for Laplacians. This formalism prepares readers for generalisations in the spherical domains in Chapter 4.

2.2.1. Winding Rates from Winding Coordinates

Let $\boldsymbol{x}$ and $\boldsymbol{x}'$ be distinct points on the Euclidean plane $\mathbb{E}^2$ (as embedded in $\mathbb{E}^3$ as $w =$ constant). We define the following (moving) polar coordinates, called *Euclidean winding*

coordinates, i.e., the right-handed, orthonormal basis vectors $\{\hat{\boldsymbol{e}}_\xi, \hat{\boldsymbol{e}}_\chi, \hat{\boldsymbol{e}}_w\}$ centred at $\boldsymbol{x}$ and $\{\hat{\boldsymbol{e}}'_\xi, \hat{\boldsymbol{e}}'_\chi, \hat{\boldsymbol{e}}'_w\}$ centred at $\boldsymbol{x}'$ given by

$$\hat{\boldsymbol{e}}_\xi \equiv \frac{\boldsymbol{x}' - \boldsymbol{x}}{|\boldsymbol{x}' - \boldsymbol{x}|}, \quad \hat{\boldsymbol{e}}_\chi \equiv \hat{\boldsymbol{e}}_w \times \hat{\boldsymbol{e}}_\xi\,; \quad \hat{\boldsymbol{e}}'_\xi \equiv \frac{\boldsymbol{x} - \boldsymbol{x}'}{|\boldsymbol{x} - \boldsymbol{x}'|}, \quad \hat{\boldsymbol{e}}'_\chi \equiv \hat{\boldsymbol{e}}'_w \times \hat{\boldsymbol{e}}'_\xi\,; \tag{2.17}$$

where $\hat{\boldsymbol{e}}_w = \hat{\boldsymbol{e}}'_w$ coincides with the unit normal vector of $\mathbb{E}^2$. These sets of basis vectors may be respectively called the $\boldsymbol{x}$- and $\boldsymbol{x}'$-centred *Euclidean winding basis*, illustrated in Figure 2.3. It is also worth mentioning that the radial coordinates $\xi = \xi' = |\boldsymbol{x} - \boldsymbol{x}'|$ correspond to the Euclidean distance between $\boldsymbol{x}$ and $\boldsymbol{x}'$, while the azimuthal coordinates χ and χ' measure changes in the winding angles as curves entangle.

Note that the bases (2.17) were not separately treated in previous works, e.g., Prior and Yeates 2014, because

$$\hat{\boldsymbol{e}}'_\xi = -\hat{\boldsymbol{e}}_\xi\,, \qquad \hat{\boldsymbol{e}}'_\chi = -\hat{\boldsymbol{e}}_\chi\,, \qquad \hat{\boldsymbol{e}}'_w = \hat{\boldsymbol{e}}_w\,. \tag{2.18}$$

Nevertheless, it is crucial to emphasise this distinction, since (2.18) no longer holds in the spherical domains.

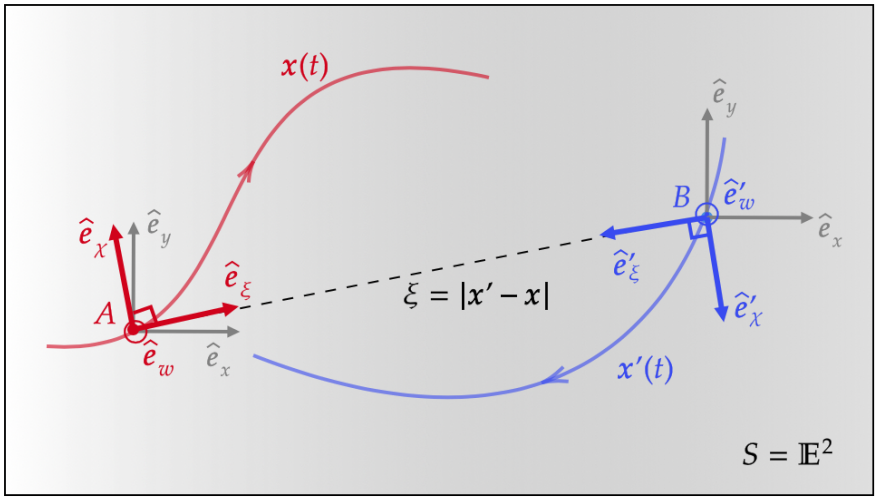

Figure 2.3: The $\boldsymbol{x}$-centred Euclidean winding basis $\{\hat{\boldsymbol{e}}_\xi, \hat{\boldsymbol{e}}_\chi, \hat{\boldsymbol{e}}_w\}$ compared to the standard Euclidean basis $\{\hat{\boldsymbol{e}}_x, \hat{\boldsymbol{e}}_y, \hat{\boldsymbol{e}}_w\}$ at $A = \boldsymbol{x}(t)$, and similarly at $B = \boldsymbol{x}'(t)$. The radial coordinate or Euclidean distance $\xi = |\boldsymbol{x}' - \boldsymbol{x}|$ is also shown.

When points $\boldsymbol{x}$ and $\boldsymbol{x}'$ are allowed to be vary, i.e., as smooth, parameterised curves $\boldsymbol{x}, \boldsymbol{x}' : [0,1] \to \mathbb{E}^2$ such that $\boldsymbol{x}(t) \neq \boldsymbol{x}'(t)$ for all $t \in [0,1]$, Euclidean winding coordinates

(2.17) remain valid. Also, let $\hat{\boldsymbol{v}}'(t) = \hat{\boldsymbol{v}}'$ on $\boldsymbol{x}'(t)$ be an arbitrary but constant unit vector that serves as a reference direction. Then, we (implicitly) define the *Euclidean winding angle* of $\boldsymbol{x}(t)$ against $\boldsymbol{x}'(t)$ along $\hat{\boldsymbol{v}}'$, denoted $\theta_{\hat{\boldsymbol{v}}'}(\boldsymbol{x};\boldsymbol{x}')$, as follows:

$$\cos\theta_{\hat{\boldsymbol{v}}'}(\boldsymbol{x};\boldsymbol{x}') = \hat{\boldsymbol{v}}' \cdot \hat{\boldsymbol{e}}'_\xi = v'_\xi \,, \tag{2.19}$$

where we decomposed $\hat{\boldsymbol{v}}'$ in the $\boldsymbol{x}'$-centred winding basis as

$$\hat{\boldsymbol{v}}' = v'_\xi \hat{\boldsymbol{e}}'_\xi + v'_\chi \hat{\boldsymbol{e}}'_\chi \,. \tag{2.20}$$

To eliminate multivaluedness, we further require $\theta_{\hat{\boldsymbol{v}}'}(\boldsymbol{x};\boldsymbol{x}')$ to be continuous, measured in the right-handed sense, and such that $\theta_{\hat{\boldsymbol{v}}'}(\boldsymbol{x};\boldsymbol{x}') = 0$ when $\hat{\boldsymbol{e}}'_\xi = \hat{\boldsymbol{v}}'$. Combining with $|\hat{\boldsymbol{v}}'|^2 = 1$, we have

$$\sin\theta_{\hat{\boldsymbol{v}}'}(\boldsymbol{x};\boldsymbol{x}') = v'_\chi \,. \tag{2.21}$$

An explicit expression for $\theta_{\hat{\boldsymbol{v}}'}(\boldsymbol{x};\boldsymbol{x}')$ in the principal range $[-\pi,\pi]$ is given by,

$$\theta_{\hat{\boldsymbol{v}}'}(\boldsymbol{x};\boldsymbol{x}') = \texttt{atan2}(v'_\chi, v'_\xi) \,. \tag{2.22}$$

It is clear from (2.19) that the exact value of the winding angle $\theta_{\hat{\boldsymbol{v}}'}(\boldsymbol{x};\boldsymbol{x}')$ depends on both the (instantaneous) reference point $\boldsymbol{x}'$ and its reference direction $\hat{\boldsymbol{v}}'$. To obtain a measure that only depends on the former (as it corresponds to the physical motion), consider differentiating (2.19) with respect to t, i.e., allowing $\boldsymbol{x}(t)$ to vary while fixing $\boldsymbol{x}'(t)$,

$$-\sin\theta_{\hat{\boldsymbol{v}}'}\left.\frac{\mathrm{d}\theta_{\hat{\boldsymbol{v}}'}}{\mathrm{d}t}\right|_{\boldsymbol{x}'} = \left.\frac{\mathrm{d}(\hat{\boldsymbol{v}}'\cdot\hat{\boldsymbol{e}}'_\xi)}{\mathrm{d}t}\right|_{\boldsymbol{x}'} = \hat{\boldsymbol{v}}'\cdot\left.\frac{\mathrm{d}\hat{\boldsymbol{e}}'_\xi}{\mathrm{d}t}\right|_{\boldsymbol{x}'} , \tag{2.23}$$

using $\hat{\boldsymbol{v}}' =$ constant in the second equality. One can check that

$$\left.\frac{\mathrm{d}\hat{\boldsymbol{e}}'_\xi}{\mathrm{d}t}\right|_{\boldsymbol{x}'} = \frac{\mathrm{d}\chi}{\mathrm{d}t}\hat{\boldsymbol{e}}'_\chi \,, \tag{2.24}$$

where $\mathrm{d}\chi/\mathrm{d}t$ is given by the decomposition of $\mathrm{d}\boldsymbol{x}/\mathrm{d}t$ in the $\boldsymbol{x}'$-centred winding basis:

$$\left.\frac{\mathrm{d}\boldsymbol{x}}{\mathrm{d}t}\right|_{\boldsymbol{x}'} = \frac{\mathrm{d}\xi}{\mathrm{d}t}\hat{\boldsymbol{e}}'_{\xi} + \xi\frac{\mathrm{d}\chi}{\mathrm{d}t}\hat{\boldsymbol{e}}'_{\chi}\,. \tag{2.25}$$

Substituting (2.20), (2.21), and (2.24) into (2.23) yields the winding rate $\omega_{\hat{\boldsymbol{v}}'}(\boldsymbol{x};\boldsymbol{x}')$ in the polar representation as

$$\omega_{\hat{\boldsymbol{v}}'}(\boldsymbol{x};\boldsymbol{x}') \equiv \left.\frac{\mathrm{d}\theta_{\hat{\boldsymbol{v}}'}}{\mathrm{d}t}\right|_{\boldsymbol{x}'} = -\frac{\mathrm{d}\chi}{\mathrm{d}t}\,. \tag{2.26}$$

Comparing with its counterpart, (2.4), (2.26) has an extra minus sign due to the opposite choice of the angle-measuring direction.

Using the vector definitions of the winding basis (2.17), (2.26) can be expressed in terms of the position vectors of both curves as

$$\omega_{\hat{\boldsymbol{v}}'}(\boldsymbol{x};\boldsymbol{x}') = -\frac{1}{\xi}\left(\frac{\mathrm{d}\boldsymbol{x}}{\mathrm{d}t}\cdot\hat{\boldsymbol{e}}'_{\chi}\right) = -\frac{\mathrm{d}\boldsymbol{x}}{\mathrm{d}t}\cdot\hat{\boldsymbol{e}}'_{w}\times\frac{\boldsymbol{x}-\boldsymbol{x}'}{|\boldsymbol{x}-\boldsymbol{x}'|^2}\,. \tag{2.27}$$

Note that $\omega_{\hat{\boldsymbol{v}}'}(\boldsymbol{x};\boldsymbol{x}')$ is now independent of the reference direction $\hat{\boldsymbol{v}}'$ and is thus a more intrinsic winding-measuring quantity. Also, (2.27) is coordinate-free, so the choice of the winding basis serves only for convenience in the derivation.

One could similarly have defined the winding angle $\theta_{\hat{\boldsymbol{v}}}(\boldsymbol{x}';\boldsymbol{x})$ of the curves $\boldsymbol{x}'$ about $\boldsymbol{x}$ along a fixed reference direction $\hat{\boldsymbol{v}}$ (on $\boldsymbol{x}$) and obtained the corresponding, direction-independent rate $\omega_{\hat{\boldsymbol{v}}}(\boldsymbol{x}';\boldsymbol{x})$ as follows

$$\omega_{\hat{\boldsymbol{v}}}(\boldsymbol{x}';\boldsymbol{x}) \equiv \left.\frac{\mathrm{d}\theta'_{\hat{\boldsymbol{v}}}}{\mathrm{d}t}\right|_{\boldsymbol{x}} = -\frac{\mathrm{d}\chi'}{\mathrm{d}t} = -\frac{\mathrm{d}\boldsymbol{x}'}{\mathrm{d}t}\cdot\hat{\boldsymbol{e}}_{w}\times\frac{\boldsymbol{x}'-\boldsymbol{x}}{|\boldsymbol{x}'-\boldsymbol{x}|^2}\,, \tag{2.28}$$

with $\mathrm{d}\chi'/\mathrm{d}t$ defined in $\boldsymbol{x}$-centred winding basis as in (2.25).

Note that neither the individual winding rates (2.27) nor (2.28) is symmetric about the curves $\boldsymbol{x}$ and $\boldsymbol{x}'$, which can be understood as the two individual summands in the product rule of differentiation. We can instead construct their sum as the symmetric, *Euclidean*

pairwise winding rate of curves $\boldsymbol{x}$ and $\boldsymbol{x}'$, i.e.,

$$\omega_{\mathrm{E}}(t;\boldsymbol{x},\boldsymbol{x}') \equiv \omega_{\hat{\boldsymbol{v}}'}(\boldsymbol{x};\boldsymbol{x}') + \omega_{\hat{\boldsymbol{v}}}(\boldsymbol{x}';\boldsymbol{x}) \tag{2.29}$$

$$= -\left(\frac{\mathrm{d}\chi}{\mathrm{d}t} + \frac{\mathrm{d}\chi'}{\mathrm{d}t}\right) \tag{2.30}$$

$$= \hat{\boldsymbol{e}}_w \cdot \frac{\mathrm{d}}{\mathrm{d}t}(\boldsymbol{x}-\boldsymbol{x}') \times \frac{\boldsymbol{x}-\boldsymbol{x}'}{|\boldsymbol{x}-\boldsymbol{x}'|^2}\,, \tag{2.31}$$

which is precisely the Euclidean winding rate (2.6) derived in §2.1.2.

2.2.2. Winding Rates from Green's Function for Laplacian

The invention of Green's functions by the English mathematician George Green (1793-1841) had a profound impact on the development of electromagnetism (Challis 2003). Here, we briefly review this concept and show how Euclidean winding rates (2.29) naturally arise from the derivative of Green's functions (see also III. §4.D in Arnold and Khesin 1998).

Intuitively, a Green's function is the "response" to a highly localised "source" in a given physical system. More precisely, given a linear differential operator $\mathcal{L}$, its *Green's function* or *fundamental solution* $G(\boldsymbol{x},\boldsymbol{x}')$, is defined to be a solution of[3], e.g., Arfken and Weber 2005; Courant and Hilbert 1989 until (2.38),

$$\mathcal{L}[G(\boldsymbol{x};\boldsymbol{x}')] = \delta(\boldsymbol{x}-\boldsymbol{x}')\,, \tag{2.32}$$

where $\delta(\boldsymbol{x}-\boldsymbol{x}')$ is the (appropriate) delta function at $\boldsymbol{x}=\boldsymbol{x}'$. Once the Green's function is known, the solution to the inhomogeneous differential equation,

$$\mathcal{L}[u(\boldsymbol{x})] = f(\boldsymbol{x})\,, \tag{2.33}$$

can be represented as

$$u(\boldsymbol{x}) = \int G(\boldsymbol{x};\boldsymbol{x}')f(\boldsymbol{x}')\ \mathrm{d}^3\boldsymbol{x}'\ . \tag{2.34}$$

[3]Note that other conventions are also possible, for example, defining G as the solution to $\mathcal{L}[G(\boldsymbol{x};\boldsymbol{x}')] = -\delta(\boldsymbol{x}-\boldsymbol{x}')$.

For Euclidean winding rates ω_{E}, we will be interested in the Laplacian Δ_{E} in $\mathbb{E}^2$, or

$$\mathcal{L} = \Delta_{\mathrm{E}} \equiv \partial_x^2 + \partial_y^2 \,, \tag{2.35}$$

as well as the associated Green's function $G_{\mathrm{E}}(\boldsymbol{x};\boldsymbol{x}')$. The latter can be obtained as follows. Since the right side of (2.32) is rotationally invariant about $\boldsymbol{x} = \boldsymbol{x}'$, so $G_{\mathrm{E}}(\boldsymbol{x};\boldsymbol{x}')$ must only depend on the Euclidean distance $\xi \equiv |\boldsymbol{x} - \boldsymbol{x}'|$, so that

$$G_{\mathrm{E}}(\boldsymbol{x};\boldsymbol{x}') = G_{\mathrm{E}}(\xi) \,. \tag{2.36}$$

Integrating both sides of (2.32) over the disc $D_\xi \equiv \{\boldsymbol{x} \in \mathbb{E}^2 : |\boldsymbol{x} - \boldsymbol{x}'| \leq \xi\}$ with boundary C_ξ and the 2D Green's theorem gives

$$1 = \int_{D_\xi} \Delta_{\mathrm{E}} G_{\mathrm{E}} \, \mathrm{d}A = \int_{C_\xi} \hat{\boldsymbol{n}} \cdot \boldsymbol{\nabla} G_{\mathrm{E}} \, \mathrm{d}l = 2\pi\xi \frac{\mathrm{d}G_{\mathrm{E}}}{\mathrm{d}\xi} \,. \tag{2.37}$$

Hence, we have,

$$G_{\mathrm{E}}(\xi) = \frac{1}{2\pi} \log \xi \,, \quad \text{or} \quad G_{\mathrm{E}}(\boldsymbol{x};\boldsymbol{x}') = \frac{1}{2\pi} \log |\boldsymbol{x} - \boldsymbol{x}'| \,, \tag{2.38}$$

where the integration constant is set to zero to ensure that $G \to 0$ as $\xi \to \infty$. It is clear that the *reciprocity property* is satisfied, i.e.,

$$G_{\mathrm{E}}(\boldsymbol{x};\boldsymbol{x}') = G_{\mathrm{E}}(\boldsymbol{x}';\boldsymbol{x}) \,. \tag{2.39}$$

To relate the Euclidean Green's function (2.38) to the Euclidean pairwise winding rate (2.31), consider taking the gradient (with respect to $\boldsymbol{x}$) of the former, which gives

$$\boldsymbol{\nabla} G_{\mathrm{E}}(\boldsymbol{x};\boldsymbol{x}') = \frac{1}{2\pi} \frac{\boldsymbol{x} - \boldsymbol{x}'}{|\boldsymbol{x} - \boldsymbol{x}'|^2} \,, \tag{2.40}$$

so that ω_{E} can be written as,

$$\omega_{\mathrm{E}}(t;\boldsymbol{x},\boldsymbol{x}') = 2\pi \hat{\boldsymbol{e}}_w \cdot \frac{\mathrm{d}}{\mathrm{d}t}(\boldsymbol{x} - \boldsymbol{x}') \times \boldsymbol{\nabla} G_{\mathrm{E}}(\boldsymbol{x};\boldsymbol{x}') \,. \tag{2.41}$$

In a formulation using complex numbers, substituting $z(t) = x(t) + \mathrm{i}y(t)$ in (2.38) gives

$$G_{\mathrm{E}}(z; z') = \frac{1}{2\pi} \log |z - z'| \,, \tag{2.42}$$

and thus we can write ω_{E} as (cf. (2.8) in §2.1.2 and later §4.2.2),

$$\omega_{\mathrm{E}}(t; z, z') = 4\pi \operatorname{Im}\left[\partial_z G_{\mathrm{E}}(z; z') \frac{\mathrm{d}(z - z')}{\mathrm{d}t}\right] . \tag{2.43}$$

Both (2.41) and (2.43) manifest that the derivative of the Green's function is an inseparable part of the Euclidean winding rate. This is an vital observation and will play an essential rôle in the spherical and periodic extensions.

2.3. Winding as a Topological Invariant

In §1.3.2, we introduced the Gauß linking number L^{G} in the topological interpretation of closed-field helicity. Recall that, for a pair of non-intersecting, arclength-parameterised, closed curves $\boldsymbol{x}, \boldsymbol{x}' : [0, 1] \to \mathbb{E}^3$, L^{G} is defined by

$$L^{\mathrm{G}}(\boldsymbol{x}, \boldsymbol{x}') \equiv \frac{1}{4\pi} \int_{\boldsymbol{x}} \int_{\boldsymbol{x}'} \mathrm{d}\boldsymbol{x} \cdot \mathrm{d}\boldsymbol{x}' \times \frac{\boldsymbol{x} - \boldsymbol{x}'}{|\boldsymbol{x} - \boldsymbol{x}'|^2} \tag{2.44}$$

$$= \frac{1}{4\pi} \int_{\boldsymbol{x}} \int_{\boldsymbol{x}'} \frac{\mathrm{d}\boldsymbol{x}}{\mathrm{d}s} \cdot \frac{\mathrm{d}\boldsymbol{x}'}{\mathrm{d}s'} \times \frac{\boldsymbol{x} - \boldsymbol{x}'}{|\boldsymbol{x} - \boldsymbol{x}'|^2} \, \mathrm{d}s' \, \mathrm{d}s \,. \tag{2.45}$$

Berger and Prior 2006 showed that, given a preferred direction, say vertical w, L^{G} can be written in terms of the Euclidean winding rates ω_{E} for pair of curves $\boldsymbol{x}, \boldsymbol{x}'$. By respectively splitting the curve $\boldsymbol{x}$ and $\boldsymbol{x}'$ into w-monotonic[4] subsections $\boldsymbol{x}_0, \cdots, \boldsymbol{x}_n$ and $\boldsymbol{x}'_0, \cdots, \boldsymbol{x}'_m$, they defined the *total winding number* L^{W} as

$$L^{\mathrm{W}}(\boldsymbol{x}, \boldsymbol{x}') \equiv \sum_{i=0}^{n} \sum_{j=0}^{m} \frac{\sigma(\boldsymbol{x}_i)\sigma(\boldsymbol{x}'_j)}{2\pi} \int_{w_{ij}^{\min}}^{w_{ij}^{\max}} \omega_{\mathrm{E}}(w; \boldsymbol{x}_i, \boldsymbol{x}'_j) \, \mathrm{d}w \,. \tag{2.46}$$

Here, $[w_{ij}^{\min}, w_{ij}^{\max}]$ is the mutual w-monotonic interval (possibly empty) shared by the

[4] with only isolated zeros of $\mathrm{d}w_i/\mathrm{d}w$ allowed.

ith subsection $\boldsymbol{x}_i$ of $\boldsymbol{x}$ and the jth subsection $\boldsymbol{x}'_j$ of $\boldsymbol{x}'$. Also, $\sigma(\boldsymbol{x}_i)$ corresponds to the transversal direction of $\boldsymbol{x}_i$, defined by

$$\sigma(\boldsymbol{x}_i) \equiv \begin{cases} +1\,, & \text{for} \quad \dfrac{\mathrm{d}w_i}{\mathrm{d}w} > 0\,; \\ -1\,, & \text{for} \quad \dfrac{\mathrm{d}w_i}{\mathrm{d}w} < 0\,; \\ 0\,, & \text{for} \quad \dfrac{\mathrm{d}w_i}{\mathrm{d}w} = 0\,; \end{cases} \qquad \text{where } w_i \equiv \hat{\boldsymbol{e}}_w \cdot \boldsymbol{x}_i\,. \tag{2.47}$$

Then, ibid. (see also Prior and Yeates 2014) proved that

Theorem 2.1 (Berger and Prior 2006, Theorem 1). *When curves $\boldsymbol{x}, \boldsymbol{x}'$ are closed, the total winding number L^{W} (along w-direction) is equal to the Gauß linking number L^{G}, and thus invariant under continuous, non-intersecting deformations of $\boldsymbol{x}$ and $\boldsymbol{x}'$.*

When the curves $\boldsymbol{x}, \boldsymbol{x}'$ are open, while the Gauß integral (2.44) can be evaluated, Theorem 2.1 in general does not hold. However, a restricted sense of topological invariance still remains, as stated in the following theorem:

Theorem 2.2 (ibid., Theorem 2). *L^{W} is invariant to all continuous, non-intersecting deformations of $\boldsymbol{x}$ and $\boldsymbol{x}'$ which vanish at $w = w_{\min}$ and $w_{\max}$.*

Thus, the total winding number L^{W} (and the associated winding rates) for a pair of curves always remains a topological quantity. For simplicity, we will consider henceforth only monotonic curves, whereas any generalisation to non-monotonic curves can, in principle, be achieved by applying Theorems 2.1 and 2.2.

Chapter 3

Winding of Open Curves in Spherical Domains

In this chapter[1], a novel definition of winding of open curves in spherical domains is proposed, a significant generalisation from the Euclidean measure in Chapter 2. The exact form of this quantity, albeit fundamental, cannot be found in the existing literature except qualitative discussions (see e.g., Campbell and Berger 2014; Crowdy and Cloke 2003 and references therein). This task is known to be non-trivial because, unlike planes, spheres are closed surfaces and have non-zero intrinsic curvature.

We organise this chapter as follows. Basic geometrical facts of the two-dimensional sphere S^2 are reviewed in §3.1. In §3.2, we construct the individual and pairwise winding rates of open curves in spherical domains, one of the major results of this thesis. It is followed, in §3.3, by two examples to illustrate the non-trivial features of spherical winding. Unless otherwise stated, (r, θ, ϕ) denotes a spherical polar coordinate system with polar angle $\theta \in [0, \pi]$ and azimuthal angle $\phi \in [0, 2\pi]$.

[1]Adapted from Chapter 5 and Appendix C, D. Xiao, C. B. Prior, and A. R. Yeates (2023a). "Spherical winding and helicity". In: *J. Phys. A: Math. Theor.* 56, p. 205201.

3.1. A Primer on Spherical Domains

When embedded (with the induced metric) in the Euclidean space $\mathbb{E}^3$, the two-dimensional sphere S^2 can be defined as

$$S^2 \equiv \{\boldsymbol{x} \in \mathbb{E}^3 : |\boldsymbol{x}| = 1\}\,. \tag{3.1}$$

The main references for this section are Lee 2019 on differential geometry (§3.1.1 and 3.1.3) and Brannan, Esplen, and Gray 1999 on general spherical geometry (§3.1.2 and 3.1.4).

3.1.1. Spherical Surface Vectors

In Euclidean spaces, it is common to treat vectors as *global* entities[2], whereas vectors on spheres can only be defined *locally*. This means that spherical vectors at different points cannot be compared directly, so the usual concept of derivatives is ill-defined. Distinct notations are adopted to distinguish them: Italic letters, e.g., $\boldsymbol{x}, \boldsymbol{y}, \cdots$ for Euclidean vectors, and Gothic letters, e.g., $\mathfrak{x}, \mathfrak{y}, \cdots$ for spherical surface vectors.

A Euclidean vector $\boldsymbol{v} \in \mathbb{E}^3$ can be treated as a *spherical surface vector* $\mathfrak{v}_p$ at some $p \in S^2$, if and only if

$$\boldsymbol{v} \cdot \boldsymbol{x}_p = 0\,, \tag{3.2}$$

where $\boldsymbol{x}_p$ is the position vector also the outwards unit normal vector to S^2 at p. The set of all surface vectors at p is called the *tangent space* to S^2 at p, denoted $T_p(S^2)$ or T_p, which can be canonically identified as the plane through p with normal $\boldsymbol{x}_p$.

A smooth *surface vector field* $\mathfrak{v}$ on S^2 is a smooth assignment of surface vectors everywhere on S^2, and it usually arises from the S^2-restriction of a Euclidean vector field.

3.1.2. Great Circles & Spherical Distances

Let A and B be distinct points on S^2 with respective Euclidean position vectors $\boldsymbol{x}$ and $\boldsymbol{x}'$. A *great circle* through A and B, denoted γ_{AB}, is the intersection of the plane OAB with

[2] in which case they are free vectors or equivalence classes of parallel vectors.

S^2, as shown in Figure 3.1. If $\boldsymbol{x} = -\boldsymbol{x}'$, then A and B are called *antipodal* and γ_{AB} is not unique. Otherwise, the great circle γ_{AB} is uniquely determined.

Any arc of a great circle on S^2 is a length-extremising[3] curve, or a *geodesic*, between its endpoints. It is the spherical analogue of a straight line (segment) on flat Euclidean planes. Using the length of the shorter arc $\overset{\frown}{AB}$ on γ_{AB}, we define the *spherical distance* between non-antipodal points A and B as

$$\xi(\boldsymbol{x}, \boldsymbol{x}') \equiv \arccos(\boldsymbol{x} \cdot \boldsymbol{x}') \,. \tag{3.3}$$

To include identical and antipodal points in the definition (3.3), we can set, for any $\boldsymbol{x} \in S^2$,

$$\xi(\boldsymbol{x}, \boldsymbol{x}) \equiv 0; \qquad \xi(\boldsymbol{x}, -\boldsymbol{x}) \equiv \pi \,. \tag{3.4}$$

In spherical polar coordinates $\boldsymbol{x} = (\theta, \phi)$ and $\boldsymbol{x}' = (\theta', \phi')$, the spherical distance $\xi(\boldsymbol{x}, \boldsymbol{x}')$ can also be expressed as

$$\cos\xi = \cos\theta' \cos\theta' + \sin\theta \sin\theta' \cos(\phi - \phi') \,, \tag{3.5}$$

also known as the spherical cosine rule. Note that it would be difficult to manipulate this expression directly, which in the hindsight could have prohibited earlier attempts.

To obtain a parameterised equation for the great circle γ_{AB} through non-antipodal points A and B, it suffices to determine scalars λ and μ such that

$$\boldsymbol{r}_{AB} = \lambda \boldsymbol{x} + \mu \boldsymbol{x}' \,, \quad \text{subject to} \quad |\boldsymbol{r}_{AB}| = 1 \,. \tag{3.6}$$

Now, using $\boldsymbol{x} \cdot \boldsymbol{x}' = \cos\xi$ and $|\boldsymbol{x}| = |\boldsymbol{x}'| = 1$, we have

$$1 = |\boldsymbol{r}_{AB}|^2 = \lambda^2 + \mu^2 + 2\lambda\mu\cos\xi \,, \tag{3.7}$$

[3] with respect to the induced metric on S^2.

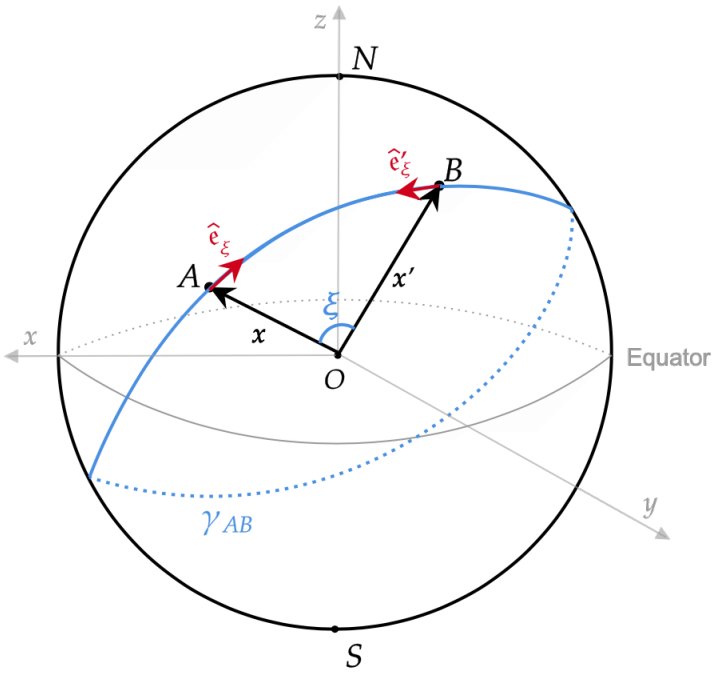

Figure 3.1: Great circle γ_{AB} through two non-antipodal points $A = \boldsymbol{x}$ and $B = \boldsymbol{x}'$ and their spherical distance ξ. The mutually-pointing separation vectors $\hat{\mathbf{e}}_\xi$ and $\hat{\mathbf{e}}'_\xi$ are also shown.

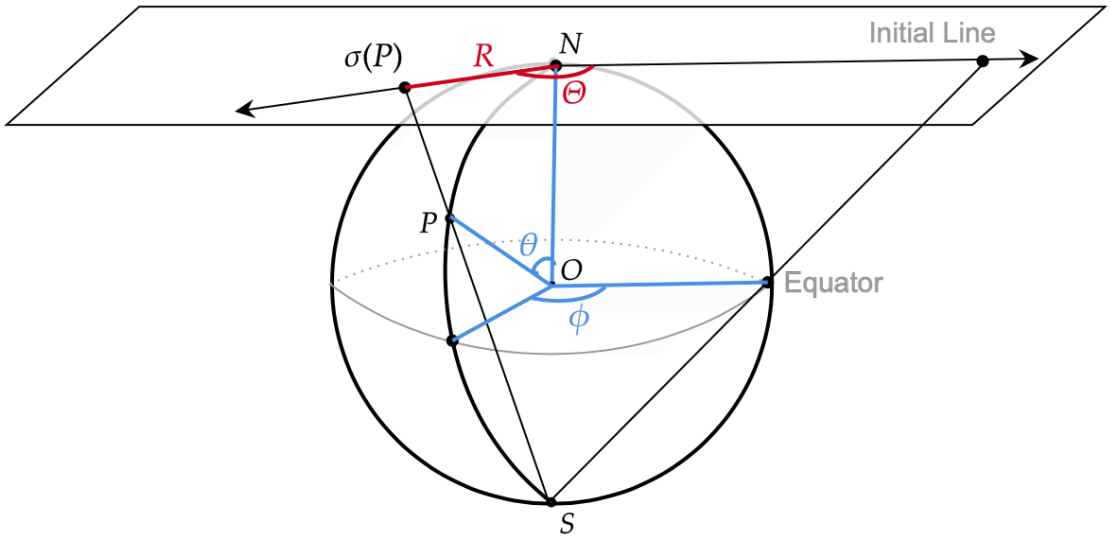

Figure 3.2: Stereographic projection $\sigma : S^2 \setminus \{\mathrm{S}\} \to \mathbb{E}^2$, $P \mapsto \sigma(P)$, as defined by (3.21). The spherical polar coordinates (θ, ϕ) on S^2 and the plane polar coordinates (R, Θ) on $\mathbb{E}^2$ are also shown for reference.

and one can solve for λ in terms of μ as

$$\lambda = -\mu \cos\xi \pm \sqrt{1 - \mu^2 \sin^2\xi}\,. \tag{3.8}$$

Consider a change of variables from μ to $t \in [0, 2\pi)$, given by

$$\mu \equiv \frac{\sin t}{\sin\xi}\,, \tag{3.9}$$

and noting that $\sin\xi > 0$, then

$$\lambda = -\sin t \cot\xi \pm \cos t\,, \tag{3.10}$$

and therefore

$$\boldsymbol{r}_{AB}(t) = \cos t\ \boldsymbol{x} + \sin t\ (-\cot\xi\ \boldsymbol{x} + \csc\xi\ \boldsymbol{x}')\,. \tag{3.11}$$

Here, we have chosen the positive sign in (3.10) to match $\boldsymbol{r}_{AB}(t=0) = \boldsymbol{x}$.

Note that the arclength $|\widehat{AB}|$ computed in the direction of increasing t is automatically the shorter arc between A and B on γ_{AB}, since setting $\boldsymbol{r}_{AB}(t) = \boldsymbol{x}'$ in (3.11) gives

$$\begin{cases} \sin t \csc\xi = 1\,, \\ \cos t - \sin t \cot\xi = 0\,; \end{cases} \tag{3.12}$$

which solves to give $t = \xi$, i.e., the parameter t is equal to the spherical distance ξ.

3.1.3. Covariant Derivatives & Parallel Transport

As aforementioned, spherical surface vectors are locally defined and cannot be differentiated in the usual sense. Here, we present an elementary derivation of a generalised sense of differentiation on spheres, called *covariant differentiation*.

On a sphere S^2 of radius r (an abuse of notation for this subsection only), the orthogonal, *coordinate basis (surface) vectors* $\boldsymbol{e}_\theta, \boldsymbol{e}_\phi$ and the *orthonormal basis (surface) vectors* $\hat{\boldsymbol{e}}_\theta, \hat{\boldsymbol{e}}_\phi$ can

be defined in terms of Euclidean basis vectors $\{\hat{\boldsymbol{e}}_x, \hat{\boldsymbol{e}}_y, \hat{\boldsymbol{e}}_w\}$ as

$$\mathfrak{e}_\theta = r\ \hat{\mathfrak{e}}_\theta = r\ (\cos\theta\cos\phi\ \hat{\boldsymbol{e}}_x + \cos\theta\sin\phi\ \hat{\boldsymbol{e}}_y - \sin\theta\ \hat{\boldsymbol{e}}_w)\,, \tag{3.13}$$

$$\mathfrak{e}_\phi = r\sin\theta\ \hat{\mathfrak{e}}_\phi = r\sin\theta\ (-\sin\phi\ \hat{\boldsymbol{e}}_x + \cos\phi\ \hat{\boldsymbol{e}}_y)\,. \tag{3.14}$$

Consider a parameterised curve $C : \boldsymbol{x}(t) = (r, \theta(t), \phi(t))$ and a surface vector $\mathfrak{f} = \mathfrak{f}^\theta\mathfrak{e}_\theta + \mathfrak{f}^\phi\mathfrak{e}_\phi$ decomposed in the orthogonal basis. The *covariant derivative of* $\mathfrak{f}$ *along* C is defined as the directional derivative of $\mathfrak{f}$ along C in the local tangent plane, i.e.,

$$\left.\frac{\mathrm{d}\mathfrak{f}}{\mathrm{d}t}\right|_C \equiv \left.\frac{\mathrm{d}\mathfrak{f}^\theta}{\mathrm{d}t}\right|_C \mathfrak{e}_\theta + \mathfrak{f}^\theta\left.\frac{\mathrm{d}\mathfrak{e}_\theta}{\mathrm{d}t}\right|_C + \left.\frac{\mathrm{d}\mathfrak{f}^\phi}{\mathrm{d}t}\right|_C \mathfrak{e}_\phi + \mathfrak{f}^\phi\left.\frac{\mathrm{d}\mathfrak{e}_\phi}{\mathrm{d}t}\right|_C \tag{3.15}$$

$$= \left.\frac{\mathrm{d}\mathfrak{f}^\theta}{\mathrm{d}t}\right|_C \mathfrak{e}_\theta + \mathfrak{f}^\theta\left(\dot\theta\frac{\partial\mathfrak{e}_\theta}{\partial\theta} + \dot\phi\frac{\partial\mathfrak{e}_\theta}{\partial\phi}\right) + \left.\frac{\mathrm{d}\mathfrak{f}^\phi}{\mathrm{d}t}\right|_C \mathfrak{e}_\phi + \mathfrak{f}^\phi\left(\dot\theta\frac{\partial\mathfrak{e}_\phi}{\partial\theta} + \dot\phi\frac{\partial\mathfrak{e}_\phi}{\partial\phi}\right), \tag{3.16}$$

using the chain rule and $\dot{(\ )} \equiv \mathrm{d}/\mathrm{d}t$ in (3.16). From (3.13)-(3.14), we have

$$\frac{\partial\mathfrak{e}_\theta}{\partial\theta} = -r\ \hat{\boldsymbol{e}}_r\,, \qquad \frac{\partial\mathfrak{e}_\theta}{\partial\phi} = \cot\theta\ \mathfrak{e}_\phi\,; \tag{3.17}$$

$$\frac{\partial\mathfrak{e}_\phi}{\partial\theta} = \cot\theta\ \mathfrak{e}_\phi\,, \qquad \frac{\partial\mathfrak{e}_\phi}{\partial\phi} = -\sin\theta\ (\cos\theta\ \mathfrak{e}_\theta + r\sin\theta\ \hat{\boldsymbol{e}}_r)\,; \tag{3.18}$$

where $\hat{\boldsymbol{e}}_r$ is the local unit radial vector. Substituting (3.17) and (3.18) into (3.16), by ignoring changes in $\hat{\boldsymbol{e}}_r$ which does not belong to the local tangent plane, gives

$$\left.\frac{\mathrm{d}\mathfrak{f}}{\mathrm{d}t}\right|_C = \left(\left.\frac{\mathrm{d}\mathfrak{f}^\theta}{\mathrm{d}t}\right|_C - \mathfrak{f}^\phi\sin\theta\cos\theta\ \dot\phi\right)\mathfrak{e}_\theta + \left[\left.\frac{\mathrm{d}\mathfrak{f}^\phi}{\mathrm{d}t}\right|_C + \cot\theta\,(\mathfrak{f}^\theta\dot\phi + \mathfrak{f}^\phi\dot\theta)\right]\mathfrak{e}_\phi\,. \tag{3.19}$$

A surface vector $\mathfrak{f}$ is called *parallel transported* along the curve C or *covariantly constant* with respect to C if

$$\left.\frac{\mathrm{d}\mathfrak{f}}{\mathrm{d}t}\right|_C = \mathbf{0}\,. \tag{3.20}$$

This is known as the *parallel transport equation*, which can be solved uniquely given an initial value $\mathfrak{f}(t=0)$.

3.1.4. Stereographic Projection

The (unit) sphere S^2 is topologically different from the Euclidean plane $\mathbb{E}^2$, since S^2 is compact whereas $\mathbb{E}^2$ is not. There exists, however, a bijective and angle-preserving map, i.e., the *stereographic projection* σ, from the punctured sphere $S^2 \setminus \{\mathrm{S}\}$ (removing the South pole[4] (S)) to $\mathbb{E}^2$. Using spherical polar coordinates $(r = 1, \theta, \phi)$ for $S^2 \setminus \{\mathrm{S}\}$ and plane polar coordinates[5] (R, Θ) for $\mathbb{E}^2$, the map σ is given by

$$\begin{aligned} &\sigma : S^2 \setminus \{\mathrm{S}\} \to \mathbb{E}^2 , \\ &\qquad (\theta, \phi) \mapsto (R, \Theta) = \left(\frac{\sin\theta}{1 + \cos\theta}, \phi \right) . \end{aligned} \tag{3.21}$$

Geometrically, as illustrated in Figure 3.2, the map σ sends every point $P(\theta, \phi) \in S^2 \setminus \{\mathrm{S}\}$ to the intersection of the line SP with $\mathbb{E}^2$ (centred at and tangent to N). Although S is not in the domain of σ, it is often common to add a "point at infinity"[6], denoted ∞, to $\mathbb{E}^2$, such that $\sigma(\mathrm{S}) \equiv \infty$.

For the inverse stereographic projection σ^{-1}, note that

$$R = \frac{2\sin\theta}{1 + \cos\theta} = 2\tan\left(\frac{\theta}{2}\right) , \tag{3.22}$$

so that we have

$$\begin{aligned} &\sigma^{-1} : \mathbb{E}^2 \to S^2 \setminus \{\mathrm{S}\} , \\ &\qquad (R, \Theta) \mapsto (\theta, \phi) = (2\arctan(R/2), \Theta) . \end{aligned} \tag{3.23}$$

Further discussions on the effects of the stereographic projection continue in §6.3.

[4] Alternatively, the stereographic projection can be defined from any other point on S^2.
[5] with the North pole (N) coinciding with the origin $r = 0$ and an appropriate choice of initial axis.
[6] which is formally known as the one-point compatification of $\mathbb{E}^2$.

3.2. Spherical Winding Rates

In this section, we construct spherical winding rates of open curves using a convenient choice of coordinates defined in §3.2.1, called the spherical winding coordinates. A detailed derivation is presented in §3.2.2. Then, in §3.2.3, we review the concept of generalised Green's functions, in particular that for the spherical Laplacian, from which we obtain alternative expressions for spherical winding rates in §3.2.4.

3.2.1. Spherical Winding Coordinates

Let A and B be distinct, non-antipodal points on S^2 with respective position vectors $\boldsymbol{x}$ and $\boldsymbol{x}'$, i.e., $\boldsymbol{x} \neq \pm\boldsymbol{x}'$. Also, let γ_{AB} be the great circle from A to B with the parameterised equation $\boldsymbol{r}_{AB}(t)$, (3.11), and similarly $\boldsymbol{r}_{BA}(t)$ from B to A. As shown in Figure 3.3 (see also Figure 3.1), we define the *separation vectors* between A and B as the mutually-pointing, unit surface tangent vectors $\hat{\boldsymbol{\epsilon}}_\xi$ to $\boldsymbol{r}_{AB}$ at A and $\hat{\boldsymbol{\epsilon}}'_\xi$ to $\boldsymbol{r}_{BA}$ at B, i.e.,

$$\hat{\boldsymbol{\epsilon}}_\xi \equiv \left.\frac{\mathrm{d}\boldsymbol{r}_{AB}}{\mathrm{d}t}\right|_A , \qquad \hat{\boldsymbol{\epsilon}}'_\xi \equiv \left.\frac{\mathrm{d}\boldsymbol{r}_{BA}}{\mathrm{d}t}\right|_B ; \tag{3.24}$$

both pointing along the shorter arc $\overset{\frown}{AB}$ from (3.12). We can explicitly compute that

$$\hat{\boldsymbol{\epsilon}}_\xi = \left.\frac{\mathrm{d}\boldsymbol{r}_{AB}}{\mathrm{d}t}\right|_{t=0} = \frac{-\cos\xi\ \boldsymbol{x} + \boldsymbol{x}'}{\sin\xi} , \tag{3.25}$$

and similarly, by reversing the rôles of $\boldsymbol{x}$ and $\boldsymbol{x}'$, we have

$$\hat{\boldsymbol{\epsilon}}'_\xi = \left.\frac{\mathrm{d}\boldsymbol{r}_{BA}}{\mathrm{d}t}\right|_{t=0} = \frac{-\cos\xi\ \boldsymbol{x}' + \boldsymbol{x}}{\sin\xi} . \tag{3.26}$$

One can verify that $|\hat{\boldsymbol{\epsilon}}_\xi| = |\hat{\boldsymbol{\epsilon}}'_\xi| = 1$, since, e.g., using $|\boldsymbol{x}| = |\boldsymbol{x}'| = 1$ and $\boldsymbol{x} \cdot \boldsymbol{x}' = \cos\xi$ gives

$$\hat{\boldsymbol{\epsilon}}_\xi \cdot \hat{\boldsymbol{\epsilon}}_\xi = \frac{1}{\sin^2\xi}[\cos^2\xi\ |\boldsymbol{x}|^2 + |\boldsymbol{x}'|^2 - 2\cos\xi(\boldsymbol{x} \cdot \boldsymbol{x}')] = 1 . \tag{3.27}$$

We can further construct unit surface vectors in the *local* azimuthal direction $\hat{\boldsymbol{\epsilon}}_\chi$ at A

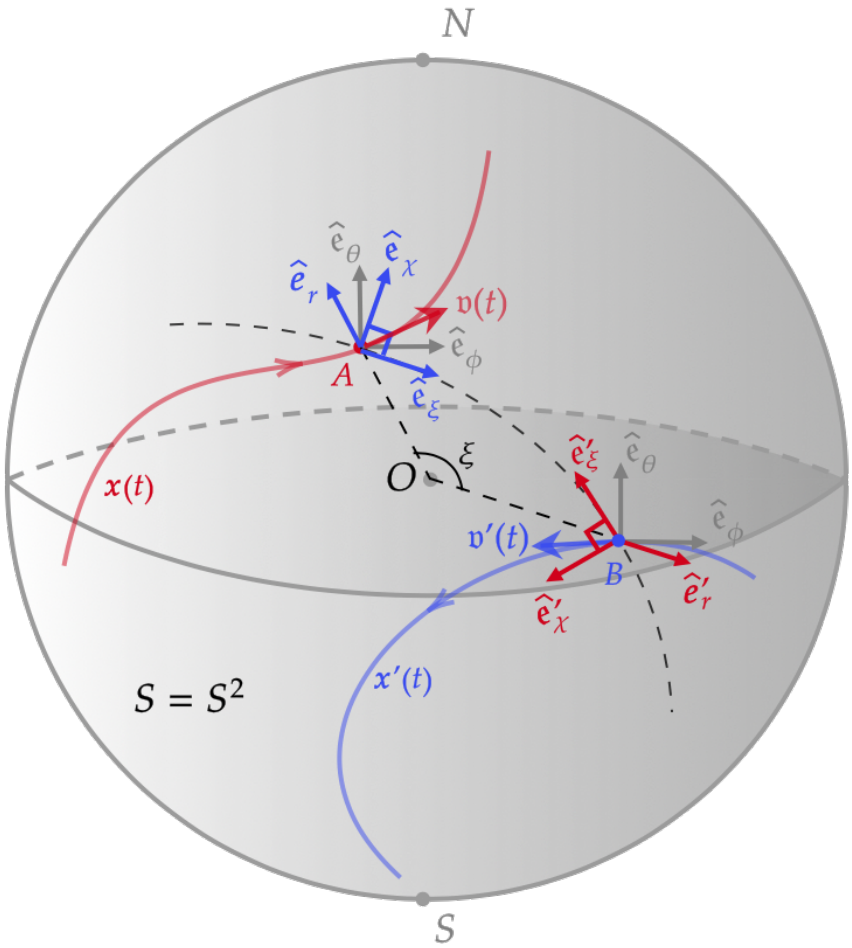

Figure 3.3: The $\boldsymbol{x}'$-Northed spherical winding basis $\{\hat{\boldsymbol{e}}_r, \hat{\boldsymbol{e}}_\xi, \hat{\boldsymbol{e}}_\chi\}$ compared to the standard spherical polar basis $\{\hat{\boldsymbol{e}}_r, \hat{\boldsymbol{e}}_\theta, \hat{\boldsymbol{e}}_\phi\}$ at $A = \boldsymbol{x}(t)$. Corresponding quantities are displayed at $B = \boldsymbol{x}'(t)$. The spherical distance $\xi(\boldsymbol{x}, \boldsymbol{x}')$ is also shown.

and $\hat{\boldsymbol{\epsilon}}'_\chi$ at B, as shown in Figure 3.3. Using orthonormality and right-handedness, define

$$\hat{\boldsymbol{\epsilon}}_\chi \equiv \frac{\hat{\boldsymbol{e}}_r \times \hat{\boldsymbol{\epsilon}}_\xi}{|\hat{\boldsymbol{e}}_r \times \hat{\boldsymbol{\epsilon}}_\xi|}, \qquad \hat{\boldsymbol{\epsilon}}'_\chi \equiv \frac{\hat{\boldsymbol{e}}'_r \times \hat{\boldsymbol{\epsilon}}'_\xi}{|\hat{\boldsymbol{e}}'_r \times \hat{\boldsymbol{\epsilon}}'_\xi|}; \tag{3.28}$$

where $\hat{\boldsymbol{e}}_r = \boldsymbol{x}$ and $\hat{\boldsymbol{e}}'_r = \boldsymbol{x}'$ are the corresponding unit normal vectors to S^2. Using (3.25) and (3.26), the definition (3.28) becomes

$$\hat{\boldsymbol{e}}_r \times \hat{\boldsymbol{\epsilon}}_\xi = \boldsymbol{x} \times \frac{-\cos\xi\ \boldsymbol{x} + \boldsymbol{x}'}{\sin\xi} = \frac{\boldsymbol{x} \times \boldsymbol{x}'}{\sin\xi} \implies \hat{\boldsymbol{\epsilon}}_\chi = \frac{\boldsymbol{x} \times \boldsymbol{x}'}{\sin\xi}, \tag{3.29}$$

noting that $|\boldsymbol{x} \times \boldsymbol{x}'| = \sin\xi$. Similarly, we have

$$\hat{\boldsymbol{\epsilon}}'_\chi = \frac{\boldsymbol{x}' \times \boldsymbol{x}}{\sin\xi}. \tag{3.30}$$

Note that $\hat{\boldsymbol{\epsilon}}_\chi$ and $\hat{\boldsymbol{\epsilon}}'_\chi$ cannot be compared directly as they are defined at different points (and thus in different tangent spaces).

Now, consider r-parameterised curves $\boldsymbol{x}, \boldsymbol{x}' : [r_1, r_2] \to S^2 \times [r_1, r_2]$ in a spherical shell such that $\boldsymbol{x}(r) \neq \pm\, \boldsymbol{x}'(r)$ is satisfied for all $r \in [r_1, r_2]$. We can define two sets of *spherical winding coordinates* (at radius r) using (3.24) and (3.28), summarised below in Table 3.1. Note that the North assumes the rôle of the "origin" in respective coordinate systems. The polar angles $\xi = \xi'$ are the intrinsic, spherical distance between $\boldsymbol{x}$ and $\boldsymbol{x}'$, whereas the azimuthal angles χ and χ' measure spherical winding as curves entangle.

Name (North position)	Current position	Spherical winding basis	Spherical winding coordinates
$\boldsymbol{x}'$-Northed	$\boldsymbol{x}$	$\{\hat{\boldsymbol{e}}_r, \hat{\boldsymbol{\epsilon}}_\xi, \hat{\boldsymbol{\epsilon}}_\chi\}$	(r, ξ, χ)
$\boldsymbol{x}$-Northed	$\boldsymbol{x}'$	$\{\hat{\boldsymbol{e}}'_r, \hat{\boldsymbol{\epsilon}}'_\xi, \hat{\boldsymbol{\epsilon}}'_\chi\}$	(r, ξ', χ')

Table 3.1: Summary of spherical winding coordinates defined for a pair of spherical curves $\boldsymbol{x}$ and $\boldsymbol{x}'$, where $\hat{\boldsymbol{e}}_r = \boldsymbol{x}/r$ and $\hat{\boldsymbol{e}}'_r = \boldsymbol{x}'/r$ are the local unit normal vectors.

3.2.2. Winding Rates from Winding Coordinates

Without loss of generality, consider smooth curves $\boldsymbol{x}, \boldsymbol{x}' : [0,1] \to S^2$ such that $\boldsymbol{x}(t) \neq \pm\boldsymbol{x}'(t)$ for all $t \in [0,1]$, understood as projections of the two corresponding curves in the spherical shell $S^2 \times [r_1, r_2]$ on S^2. Also, let $\{\hat{\boldsymbol{e}}_r, \hat{\mathbf{e}}_\xi, \hat{\mathbf{e}}_\chi\}$ be the $\boldsymbol{x}'$-Northed spherical winding basis at $\boldsymbol{x}$, and $\{\hat{\boldsymbol{e}}'_r, \hat{\mathbf{e}}'_\xi, \hat{\mathbf{e}}'_\chi\}$ be the $\boldsymbol{x}$-Northed spherical winding basis at $\boldsymbol{x}'$.

We first implicitly define the *spherical winding angle*, denoted $\theta_{\hat{\mathfrak{v}}'}(\boldsymbol{x}; \boldsymbol{x}')$, of $\boldsymbol{x}(t)$ seen from $\boldsymbol{x}'(t)$ with respect to the local reference direction $\hat{\mathfrak{v}}'(t)$ on $\boldsymbol{x}'(t)$. We choose $\hat{\mathfrak{v}}'(t)$ such that it is a unit surface vector covariantly constant on $\boldsymbol{x}'(t)$, i.e., parallel transported on $\boldsymbol{x}'(t)$ from an arbitrary, initial choice $\hat{\mathfrak{v}}'_0$ (cf. §3.1.3). Then,

$$\cos\theta_{\hat{\mathfrak{v}}'}(\boldsymbol{x}; \boldsymbol{x}') = \hat{\mathfrak{v}}' \cdot \hat{\mathbf{e}}'_\xi = \mathfrak{v}'_\xi \,, \tag{3.31}$$

where the last equality follows from the $\boldsymbol{x}$-Northed decomposition of $\hat{\mathfrak{v}}'$,

$$\hat{\mathfrak{v}}' = \mathfrak{v}'_\xi \hat{\mathbf{e}}'_\xi + \mathfrak{v}'_\chi \hat{\mathbf{e}}'_\chi \,. \tag{3.32}$$

We require $\theta_{\hat{\mathfrak{v}}'}(\boldsymbol{x}; \boldsymbol{x}')$ to be continuous, measured in the right-handed sense, and such that $\theta_{\hat{\mathfrak{v}}'}(\boldsymbol{x}; \boldsymbol{x}') = 0$ when $\hat{\mathbf{e}}'_\xi = \hat{\mathfrak{v}}'$. Combining (3.31) with

$$|\hat{\mathfrak{v}}'|^2 = \mathfrak{v}'^2_\xi + \mathfrak{v}'^2_\chi = 1 \,, \tag{3.33}$$

we obtain

$$\sin\theta_{\hat{\mathfrak{v}}'}(\boldsymbol{x}; \boldsymbol{x}') = \mathfrak{v}'_\chi \,. \tag{3.34}$$

Recall that in the Euclidean case (§2.2.1) we derived a winding measure that depends only on the (instantaneous) reference point but not the reference direction. To see how it generalises to spherical domains, consider differentiating (3.31) with respect to t while fixing $\boldsymbol{x}'(t)$,

$$-\sin\theta_{\hat{\mathfrak{v}}'}\, \frac{\mathrm{d}\theta_{\hat{\mathfrak{v}}'}}{\mathrm{d}t}\bigg|_{\boldsymbol{x}'} = \frac{\mathrm{d}(\hat{\mathfrak{v}}' \cdot \hat{\mathbf{e}}'_\xi)}{\mathrm{d}t}\bigg|_{\boldsymbol{x}', \hat{\mathfrak{v}}'} + \frac{\mathrm{d}(\hat{\mathfrak{v}}' \cdot \hat{\mathbf{e}}'_\xi)}{\mathrm{d}t}\bigg|_{\boldsymbol{x}', \hat{\mathbf{e}}'_\xi} = \hat{\mathfrak{v}}' \cdot \frac{\mathrm{d}\hat{\mathbf{e}}'_\xi}{\mathrm{d}t}\bigg|_{\boldsymbol{x}'} + \frac{\mathrm{d}\mathfrak{v}'_\xi}{\mathrm{d}t}\bigg|_{\boldsymbol{x}'} \,. \tag{3.35}$$

Comparing with (2.23), it is the second term on the right side of (3.35) that distinguishes the spherical case from Euclidean. The *non-zero* curvature of spherical surfaces results in the *non-trivial* parallel transport of the reference direction $\hat{\mathfrak{v}}'(t)$ on $\boldsymbol{x}'(t)$, and this term measures the winding contribution from the changes (though covariantly constant) in $\hat{\mathfrak{v}}'(t)$. It can be computed from the parallel transport equation (3.20) as follows:

$$\hat{\boldsymbol{\epsilon}}'_\xi \cdot \frac{\mathrm{d}\hat{\mathfrak{v}}'}{\mathrm{d}t}\bigg|_{\boldsymbol{x}'} = \left(-\frac{\mathrm{d}\mathfrak{v}'_\xi}{\mathrm{d}t}\bigg|_{\boldsymbol{x}'}\right) - \sin\xi'\cos\xi'\frac{\mathrm{d}\chi'}{\mathrm{d}t}\left(-\frac{\mathfrak{v}'_\chi}{\sin\xi}\right) = 0\,, \tag{3.36}$$

where we identify,

$$\mathfrak{f}^\theta \leftrightarrow -\mathfrak{v}'_\xi\,, \quad \mathfrak{f}^\phi \leftrightarrow -\frac{\mathfrak{v}'_\chi}{\sin\xi'}\,, \tag{3.37}$$

recalling that $\mathfrak{f}$ and $\hat{\mathfrak{v}}'$ are written in the orthogonal coordinate basis. Here, $\mathrm{d}\chi'/\mathrm{d}t$ is defined as the projection of $\mathrm{d}\boldsymbol{x}'/\mathrm{d}t$ in the $\boldsymbol{x}$-Northed winding basis at $\boldsymbol{x}'$,

$$\frac{\mathrm{d}\boldsymbol{x}'}{\mathrm{d}t} = \frac{\mathrm{d}\xi'}{\mathrm{d}t}\hat{\boldsymbol{\epsilon}}'_\xi + \sin\xi'\frac{\mathrm{d}\chi'}{\mathrm{d}t}\hat{\boldsymbol{\epsilon}}'_\chi\,, \tag{3.38}$$

so that

$$\frac{\mathrm{d}\mathfrak{v}'_\xi}{\mathrm{d}t}\bigg|_{\boldsymbol{x}'} = -\cos\xi'\frac{\mathrm{d}\chi'}{\mathrm{d}t}\mathfrak{v}'_\chi\,. \tag{3.39}$$

The first term on the right side of (3.35) measures the winding contribution as the curve $\boldsymbol{x}'(t)$ entangles about $\boldsymbol{x}(t)$, as in the Euclidean case (2.26). Substituting $\hat{\boldsymbol{\epsilon}}'_\xi$ with the expression (3.26) while fixing $\boldsymbol{x}'(t)$, so that,

$$\frac{\mathrm{d}\hat{\boldsymbol{\epsilon}}'_\xi}{\mathrm{d}t}\bigg|_{\boldsymbol{x}'} = \frac{1}{\sin^2\xi}\left[(\boldsymbol{x}' - \cos\xi\boldsymbol{x})\frac{\mathrm{d}\xi}{\mathrm{d}t} + \sin\xi\frac{\mathrm{d}\boldsymbol{x}}{\mathrm{d}t}\right]. \tag{3.40}$$

Retrospectively, one can verify that $\mathrm{d}\hat{\boldsymbol{\epsilon}}'_\xi/\mathrm{d}t$ is indeed a surface vector at $\boldsymbol{x}'$, since

$$\boldsymbol{x}' \cdot \frac{\mathrm{d}\hat{\boldsymbol{\epsilon}}'_\xi}{\mathrm{d}t} = 0\,, \quad \hat{\boldsymbol{\epsilon}}'_\xi \cdot \frac{\mathrm{d}\hat{\boldsymbol{\epsilon}}'_\xi}{\mathrm{d}t} = 0\,; \tag{3.41}$$

and it also aligns entirely with $\hat{\mathbf{e}}'_\chi$. Its magnitude can be computed from

$$\left|\frac{\mathrm{d}\hat{\mathbf{e}}'_\xi}{\mathrm{d}t}\right|^2 = \frac{1}{\sin^2\xi}\left[\left|\frac{\mathrm{d}\boldsymbol{x}}{\mathrm{d}t}\right|^2 - \left(\frac{\mathrm{d}\xi}{\mathrm{d}t}\right)^2\right] = \left(\frac{\mathrm{d}\chi}{\mathrm{d}t}\right)^2 \implies \frac{\mathrm{d}\hat{\mathbf{e}}'_\xi}{\mathrm{d}t} = \frac{\mathrm{d}\chi}{\mathrm{d}t}\,, \tag{3.42}$$

choosing the positive sign to match its Euclidean counterpart (2.24). Here, $\mathrm{d}\chi/\mathrm{d}t$ is defined by decomposing $\mathrm{d}\boldsymbol{x}/\mathrm{d}t$ in the $\boldsymbol{x}'$-Northed winding basis $\{\hat{\boldsymbol{e}}_r, \hat{\mathbf{e}}_\xi, \hat{\mathbf{e}}_\chi\}$ as

$$\frac{\mathrm{d}\boldsymbol{x}}{\mathrm{d}t} = \frac{\mathrm{d}\xi}{\mathrm{d}t}\hat{\mathbf{e}}_\xi + \sin\xi\frac{\mathrm{d}\chi}{\mathrm{d}t}\hat{\mathbf{e}}_\chi\,. \tag{3.43}$$

Hence, we obtain

$$\hat{\boldsymbol{\mathfrak{v}}}'\cdot\left.\frac{\mathrm{d}\hat{\mathbf{e}}'_\xi}{\mathrm{d}t}\right|_{\boldsymbol{x}'} = \mathfrak{v}'_\chi\frac{\mathrm{d}\chi}{\mathrm{d}t}\,. \tag{3.44}$$

Substituting both (3.39) and (3.44) into (3.35) yields the *individual spherical winding rate* of $\boldsymbol{x}$ against $\boldsymbol{x}'$ along $\hat{\boldsymbol{\mathfrak{v}}}'$, i.e.,

$$\omega_{\hat{\boldsymbol{\mathfrak{v}}}'}(\boldsymbol{x};\boldsymbol{x}') \equiv \frac{\mathrm{d}\theta_{\hat{\boldsymbol{\mathfrak{v}}}'}}{\mathrm{d}t} = -\left(\cos\xi\frac{\mathrm{d}\chi'}{\mathrm{d}t} + \frac{\mathrm{d}\chi}{\mathrm{d}t}\right), \tag{3.45}$$

which is manifestly independent of the reference direction $\hat{\boldsymbol{\mathfrak{v}}}'$ provided it is covariantly constant on $\boldsymbol{x}'(t)$. This allows us to suppress $\hat{\boldsymbol{\mathfrak{v}}}'$ without loss of generality in future discussions. In terms of Euclidean vectors of both curves, (3.45) can be written coordinate-independent as

$$-\omega(\boldsymbol{x};\boldsymbol{x}') = \frac{\cos\xi}{\sin\xi}\frac{\mathrm{d}\boldsymbol{x}'}{\mathrm{d}t}\cdot\hat{\mathbf{e}}'_\chi + \frac{1}{\sin\xi}\frac{\mathrm{d}\boldsymbol{x}}{\mathrm{d}t}\cdot\hat{\mathbf{e}}_\chi \tag{3.46}$$

$$= \frac{1}{\sin^2\xi}\left(\cos\xi\frac{\mathrm{d}\boldsymbol{x}'}{\mathrm{d}t}\cdot\boldsymbol{x}\times\boldsymbol{x}' + \frac{\mathrm{d}\boldsymbol{x}}{\mathrm{d}t}\cdot\boldsymbol{x}'\times\boldsymbol{x}\right). \tag{3.47}$$

This confirms the universal nature of this expression, whereas the use of spherical winding coordinates only facilitates derivation.

Seen from the perspective of $\boldsymbol{x}(t)$, we can similarly define the spherical winding angle $\theta_{\hat{\boldsymbol{\mathfrak{v}}}}(\boldsymbol{x}';\boldsymbol{x})$ of $\boldsymbol{x}'(t)$ along covariantly constant $\hat{\boldsymbol{\mathfrak{v}}}(t)$ on $\boldsymbol{x}(t)$, and corresponding individual spherical winding rate $\omega(\boldsymbol{x}';\boldsymbol{x})$ of $\boldsymbol{x}'(t)$ against $\boldsymbol{x}(t)$. Although swapping $\boldsymbol{x}\leftrightarrow\boldsymbol{x}'$ in $\omega(\boldsymbol{x};\boldsymbol{x}')$ does not yield $\omega(\boldsymbol{x}';\boldsymbol{x})$, this asymmetry can be overcome by defining the *(pairwise) spherical*

winding rate $\omega_{\mathrm{s}}(t;\boldsymbol{x},\boldsymbol{x}')$ as the arithmetic average of two individual measures, i.e.,

$$\omega_{\mathrm{s}}(t;\boldsymbol{x},\boldsymbol{x}') \equiv \frac{1}{2}[\omega(\boldsymbol{x};\boldsymbol{x}') + \omega(\boldsymbol{x}';\boldsymbol{x})] \tag{3.48}$$

$$= -\frac{1+\cos\xi}{2}\left(\frac{\mathrm{d}\chi}{\mathrm{d}t} + \frac{\mathrm{d}\chi'}{\mathrm{d}t}\right) \tag{3.49}$$

$$= \frac{1}{2(1-\cos\xi)}\frac{\mathrm{d}}{\mathrm{d}t}(\boldsymbol{x}-\boldsymbol{x}')\cdot\boldsymbol{x}\times\boldsymbol{x}' \,. \tag{3.50}$$

The pre-factor $(1+\cos\xi)$ also resolves the isolated case when $\boldsymbol{x}$ and $\boldsymbol{x}'$ are antipodal ($\cos\xi = -1$), which we have previously excluded. We have thus constructed the spherical analogue of the Euclidean winding rates (2.29), providing an intrinsic measure of winding for any pair of spherical curves.

For the examples later in §3.3, we make two further definitions, following §2.1.3. Integrating the winding rate with respect to t gives the cumulative change of winding angle, which we shall call the *spherical winding number*. The *individual spherical winding number* $L_{\mathrm{s}}(\boldsymbol{x};\boldsymbol{x}')$ of curve $\boldsymbol{x}(t)$ against $\boldsymbol{x}'(t)$ is defined by

$$L_{\mathrm{s}}(\boldsymbol{x};\boldsymbol{x}') \equiv \frac{1}{2\pi}\int_0^1 \omega\big[\boldsymbol{x}(t);\boldsymbol{x}'(t)\big]\,\mathrm{d}t = -\frac{1}{2\pi}\int_0^1 \left(\cos\xi\frac{\mathrm{d}\chi'}{\mathrm{d}t} + \frac{\mathrm{d}\chi}{\mathrm{d}t}\right)\mathrm{d}t \,. \tag{3.51}$$

The *(pairwise) spherical winding number* $\mathcal{L}_{\mathrm{s}}(\boldsymbol{x},\boldsymbol{x}')$ of curves $\boldsymbol{x}(t)$ and $\boldsymbol{x}'(t)$ is given by

$$\mathcal{L}_{\mathrm{s}}(\boldsymbol{x},\boldsymbol{x}') \equiv \frac{1}{2}\big[L_{\mathrm{s}}(\boldsymbol{x};\boldsymbol{x}') + L_{\mathrm{s}}(\boldsymbol{x}';\boldsymbol{x})\big] = \frac{1}{4\pi}\int_0^1 \omega_{\mathrm{s}}(t;\boldsymbol{x},\boldsymbol{x}')\,\mathrm{d}t \tag{3.52}$$

$$= -\frac{1}{4\pi}\int_0^1 (1+\cos\xi)\left(\frac{\mathrm{d}\chi}{\mathrm{d}t} + \frac{\mathrm{d}\chi'}{\mathrm{d}t}\right)\mathrm{d}t \,. \tag{3.53}$$

By definition, $\mathcal{L}_{\mathrm{s}}(\boldsymbol{x},\boldsymbol{x}')$ is symmetric about both curves, independent of the choice of reference directions on either curve, and invariant under coordinate transformations.

3.2.3. Generalised Green's Functions

Recall that in §2.2.2, we related Euclidean winding rates to Green's functions for the Laplacian on $\mathbb{E}^2$. However, there does not exist a similar Green's function on S^2, a

consequence of the *Fredholm*[7] *Alternative (Theorem).* A version sufficient for our discussions is given as follows; see e.g., Courant and Hilbert 1989; Evans 2010; Paul 2019,

Theorem 3.1 (Fredholm Alternative). *Let $\mathcal{L}$ be a suitably defined elliptic operator and consider solutions to the inhomogeneous differential equation*

$$\mathcal{L}[u] = f\,, \tag{‡}$$

with boundary conditions such that $\mathcal{L}$ is self-adjoint. Then,

(i) if the only solution to $\mathcal{L}[u] = 0$ satisfying boundary conditions is the trivial solution $u = 0$, i.e., if $\lambda = 0$ is not an eigenvalue of $\mathcal{L}$, then there is a unique solution to (‡); or

(ii) if there are non-trivial solutions to $\mathcal{L}[u] = 0$ satisfying boundary conditions, i.e., if $\lambda = 0$ is an eigenvalue of $\mathcal{L}$, then there are either no solution or infinitely many solutions to (‡);

and the criteria for (‡) to have a solution is that, for any u_0 such that $\mathcal{L}[u_0] = 0$, we require that the orthogonality condition holds:

$$\int f(\boldsymbol{x}) u_0(\boldsymbol{x})\, \mathrm{d}\boldsymbol{x} = 0\,. \tag{3.54}$$

For spherical winding rates, we will be interested in the surface Laplacian $\Delta_{\mathcal{S}}$, or the *Laplace*[8]*–Beltrami*[9] *operator*, on $\mathcal{S} = S^2$. It can be given explicitly in spherical polar coordinates as

$$\Delta_{\mathcal{S}} = \frac{1}{\sin\theta}\frac{\partial}{\partial\theta}\left(\sin\theta\frac{\partial}{\partial\theta}\right) + \frac{1}{\sin^2\theta}\frac{\partial^2}{\partial\phi^2}\,. \tag{3.55}$$

For the Poisson's equation on S^2

$$\Delta_{\mathcal{S}} u = f\,, \tag{3.56}$$

the non-trivial, everywhere-regular solution (with the constant chosen specifically for the normalisation) (Courant and Hilbert 1989)

$$u_0 = \frac{1}{\sqrt{4\pi}}\,, \tag{3.57}$$

[7] Erik Ivar Fredholm, Swedish, 1866-1927.
[8] Pierre-Simon Laplace, French, 1749-1827.
[9] Eugenio Beltrami, Italian, 1835-1900

satisfies Theorem 3.1(ii), i.e.,

$$\Delta_{\mathcal{S}} u_0 = 0\,. \tag{3.58}$$

Hence, (3.56) has infinitely many solutions and $\Delta_{\mathcal{S}}$ has no Green's functions.

This leads to the concept of *Green's functions in the generalised sense*, or *generalised Green's function*, see e.g., Courant and Hilbert 1989; Paul 2019. Let $\mathcal{L}$ be a differential operator satisfying the conditions of Theorem 3.1(ii) with $\mathcal{L}[u_0] = 0$ for some non-trivial u_0. Then, we can define the generalised Green's function $G(\boldsymbol{x}, \boldsymbol{x}')$ be the solution to, cf. (2.32),

$$\mathcal{L}[G(\boldsymbol{x}, \boldsymbol{x}')] = \delta(\boldsymbol{x}, \boldsymbol{x}') - \frac{u_0(\boldsymbol{x}) u_0(\boldsymbol{x}')}{\langle u_0, u_0 \rangle}\,, \tag{3.59}$$

where $\delta(\boldsymbol{x}, \boldsymbol{x}')$ is the (appropriate) delta function at $\boldsymbol{x} = \boldsymbol{x}'$ and $\langle f, g \rangle \equiv \int f g \,\mathrm{d}V$. It is a well-defined solution to (3.56), since the right side of (3.59) satisfies the compatibility condition (3.54),

$$\int u_0(\boldsymbol{x}') \left(\delta(\boldsymbol{x}, \boldsymbol{x}') - \frac{u_0(\boldsymbol{x}) u_0(\boldsymbol{x}')}{\langle u_0, u_0 \rangle} \right) \mathrm{d}\boldsymbol{x}' = u(\boldsymbol{x}) - \frac{\langle u_0, u_0 \rangle \, u_0(\boldsymbol{x})}{\langle u_0, u_0 \rangle} = 0\,. \tag{3.60}$$

The general form of solutions $u(\boldsymbol{x})$ to (‡) is then given by

$$u(\boldsymbol{x}) = \int G(\boldsymbol{x}, \boldsymbol{x}') f(\boldsymbol{x}') \,\mathrm{d}\boldsymbol{x}' + k u_0(\boldsymbol{x})\,, \tag{3.61}$$

for some constant k. Uniqueness can be imposed, e.g., by enforcing additionally

$$\int u(\boldsymbol{x}) u_0(\boldsymbol{x}) \,\mathrm{d}\boldsymbol{x} = 0\,. \tag{3.62}$$

3.2.4. Winding Rates from Generalised Green's Functions for Laplacian

To construct a generalised Green's function $G_{\mathrm{s}}(\boldsymbol{x}, \boldsymbol{x}')$ for the spherical Laplacian $\Delta_{\mathcal{S}}$, (3.55), we can solve (3.59) by substituting the constant solution (3.57), i.e., (adapted from

Courant and Hilbert 1989 until (3.65))

$$\Delta_{\mathcal{S}} G_{\mathrm{s}}(\boldsymbol{x}, \boldsymbol{x}') = \delta(\boldsymbol{x}, \boldsymbol{x}') - \frac{1}{4\pi} \,. \tag{3.63}$$

We first deduce that G_{s} is rotationally invariant as satisfied by the right side of (3.63). This allows us to set, without loss of generality, the source $\boldsymbol{x}'$ to the North pole N with $\theta = 0$, so that G_{s} is ϕ-independent. Solving this ordinary differential equation gives

$$G_{\mathrm{s}}(\boldsymbol{x}, N) = \frac{1}{4\pi} \log(1 - \cos\theta) \,, \tag{3.64}$$

such that $\Delta_{\mathcal{S}} G_{\mathrm{s}} = -1/(4\pi)$ when $\boldsymbol{x} \neq \mathrm{N}$ and G_{s} has the required singularity as $\boldsymbol{x} \to \mathrm{N}$. Then, by replacing θ by the spherical distance $\xi(\boldsymbol{x}, \boldsymbol{x}')$, defined in §3.1.2, we obtain the general expression for $G_{\mathrm{s}}(\boldsymbol{x}, \boldsymbol{x}')$ as

$$G_{\mathrm{s}}(\boldsymbol{x}, \boldsymbol{x}') = \frac{1}{4\pi} \log\big(1 - \cos[\xi(\boldsymbol{x}, \boldsymbol{x}')]\big) \,. \tag{3.65}$$

Differentiating the generalised Green's function G_{s} with respect to ξ, we have

$$\frac{\mathrm{d}G_{\mathrm{s}}}{\mathrm{d}\xi} = \frac{\sin\xi}{1 - \cos\xi} = \frac{1 + \cos\xi}{\sin\xi} \,, \tag{3.66}$$

so that the spherical winding rate ω_{s}, (3.48), can be written as, noting that $\xi = \xi'$,

$$\omega_{\mathrm{s}}(\boldsymbol{x}, \boldsymbol{x}') = \frac{1 + \cos\xi}{\sin\xi} \left(\sin\xi \frac{\mathrm{d}\chi}{\mathrm{d}t} + \sin\xi' \frac{\mathrm{d}\chi'}{\mathrm{d}t} \right) = \frac{\mathrm{d}G_{\mathrm{s}}}{\mathrm{d}\xi} \left(\frac{\mathrm{d}\chi}{\mathrm{d}t} + \frac{\mathrm{d}\chi'}{\mathrm{d}t} \right) . \tag{3.67}$$

This again manifests the direct link between the derivative of the generalised Green's function G_{s} and the spherical winding rate ω_{s}, analogous to the Euclidean case §2.2.2 (and also to the periodic case §4.2.2).

3.3. Examples of Spherical Winding

In this section, we illustrate novel properties of spherical winding, using the examples of a helix-line pair (in §3.3.1) and a belt-trick pair (in §3.3.2), both of which are r-monotonic. We work in the spherical shell $V_{\mathrm{s}} = S^2 \times [r_1 = 1, r_2 = 3]$ with some fixed, spherical polar coordinates (r, θ, ϕ), although these choices are merely for the convenience of description. This is because spherical winding measures can be written in coordinate-free, vector notations and are thus intrinsic to curve configurations.

We compute, in V_{s}, both the symmetric, pairwise spherical winding number $\mathcal{L}_{\mathrm{s}}(\boldsymbol{x}, \boldsymbol{x}')$ for curves $\boldsymbol{x}$ and $\boldsymbol{x}'$ from (3.53), and individual spherical winding numbers $L_{\mathrm{s}}(\boldsymbol{x}; \boldsymbol{x}')$ and $L_{\mathrm{s}}(\boldsymbol{x}'; \boldsymbol{x})$ from (3.51). (For simplicity, the subscript "s" will be suppressed henceforth.) Both provide insight into how spherical winding is accumulated during curve entanglement.

3.3.1. A Helix-Line Pair

As shown in Figures 3.4(a), 3.5(a), and 3.6(a), we first consider the pair of open spherical curves which consists of a radial line $\boldsymbol{x}_L(r)$ (in red) located at (r, θ_L, ϕ_L), and a spherical helix $\boldsymbol{x}_H(r)$ (in blue) centred at (r, θ_H, ϕ_H) with angular radius $r_h \in (0, \pi)$ (in units of radians) and angular velocity $\omega > 0$ (in units of radians per unit parameter, right-handed seen from the North). This is the simplest, non-trivial configuration of open spherical curves, which shall be called a *helix-line pair*.

Asymmetry of Individual Winding

We first examine the case when the line $\boldsymbol{x}_L$ and the (centre of) helix $\boldsymbol{x}_H$ are both fixed at the North, i.e., $(\theta_L, \phi_L) = (\theta_H, \phi_H) = (0, 0)$, with $r_h = \pi/3$ and $\omega = 2\pi$, as shown in Figure 3.4(a). In Figure 3.4(b), we plot the individual spherical winding number $L(\boldsymbol{x}_H; \boldsymbol{x}_L)$ of helix relative to line (in blue), $L(\boldsymbol{x}_L; \boldsymbol{x}_H)$ of line relative to helix (in red), and their average, pairwise winding number $\mathcal{L}(\boldsymbol{x}_H, \boldsymbol{x}_L)$ (in black), all against the radial parameter r.

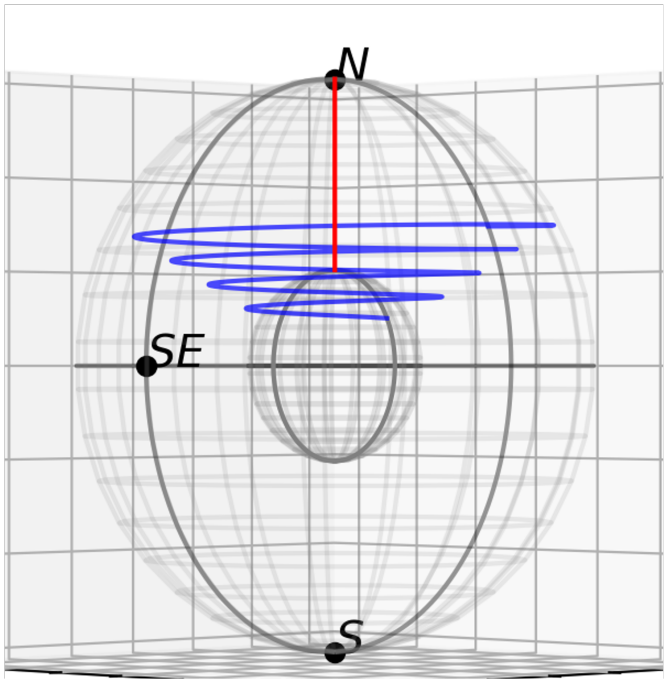

(a)

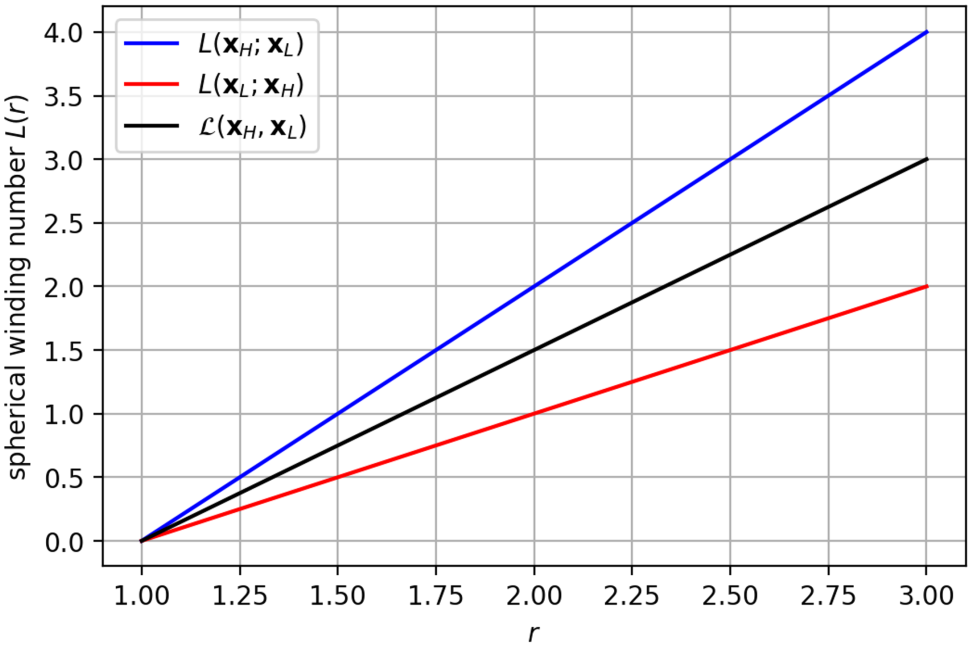

(b)

Figure 3.4: (a) Spherical winding of a helix-line pair both fixed at North. The line $\boldsymbol{x}_L$ is shown in red, and the helix $\boldsymbol{x}_H$ is shown in blue with angular radius $r_h = \pi/3$ and angular speed $\omega = 2\pi$. (b) Individual and pairwise spherical winding numbers against the radial parameter r.

All winding quantities are positive and increase linearly, as the helix $\boldsymbol{x}_H$ rotates right-handedly with uniform speed. In particular, $L(\boldsymbol{x}_H;\boldsymbol{x}_L)$ measures the (full or partial) number of turns completed by $\boldsymbol{x}_H$ in reference coordinates (of $\boldsymbol{x}_L$). However, due to the asymmetry in the individual spherical winding number from the intrinsic spherical curvature, we confirm that in this case $L(\boldsymbol{x}_L;\boldsymbol{x}_H) \neq L(\boldsymbol{x}_H;\boldsymbol{x}_L)$. As pointed out by Campbell and Berger 2014, $L(\boldsymbol{x}_L;\boldsymbol{x}_H)$ and $L(\boldsymbol{x}_H;\boldsymbol{x}_L)$ are related by the Gauss-Bonnet theorem, i.e.,

$$L(\boldsymbol{x}_L;\boldsymbol{x}_H) = \frac{L(\boldsymbol{x}_H;\boldsymbol{x}_L)}{2\pi} \oint_{\boldsymbol{x}_H} \kappa_g \,\mathrm{d}l \tag{3.68}$$

$$= \frac{L(\boldsymbol{x}_H;\boldsymbol{x}_L)}{2\pi} \cdot \frac{\cos r_h}{\sin r_h} \cdot 2\pi \sin r_h \tag{3.69}$$

$$= L(\boldsymbol{x}_H;\boldsymbol{x}_L) \cos r_h \,, \tag{3.70}$$

where

$$\kappa_g = \cos r_h / \sin r_h \,, \tag{3.71}$$

is the (constant) geodesic curvature of the helix $\boldsymbol{x}_H$ with a fixed angular radius r_h (as projected on S^2). While ibid. only considered this simplest example, we have generalised the spherical measure for *any* pair of spherical curves.

Inside or Outside?

Next, we consider the scenario shown in Figure 3.5(a), which is a helix-line pair fixed at North while the angular radius r_h of the helix increases from 0 to π. As r_h increases, it becomes less clear whether the two curves remain entangled. Indeed, one might argue that the line is outside the region enclosed by the faintest helix. Such ambiguity would not be present in Euclidean domains. In Figure 3.5(b), we plot the *final* (evaluated at $r = r_2$) spherical winding numbers, both individual and pairwise.

Note that the final individual winding number $L(\boldsymbol{x}_H;\boldsymbol{x}_L)$ (in blue) is independent of r_h. This corresponds exactly to the total number of (full) rotations of $\boldsymbol{x}_H$ in reference coordinates. However, the pairwise winding number $\mathcal{L}(\boldsymbol{x}_L,\boldsymbol{x}_H)$ (in black) does have an r_h-dependence, since the individual winding $L(\boldsymbol{x}_L;\boldsymbol{x}_H)$ (in red) of $\boldsymbol{x}_L$ seen from $\boldsymbol{x}_H$ varies significantly as the reference direction is parallel transported on $\boldsymbol{x}_H$. Indeed, its sinusoidal

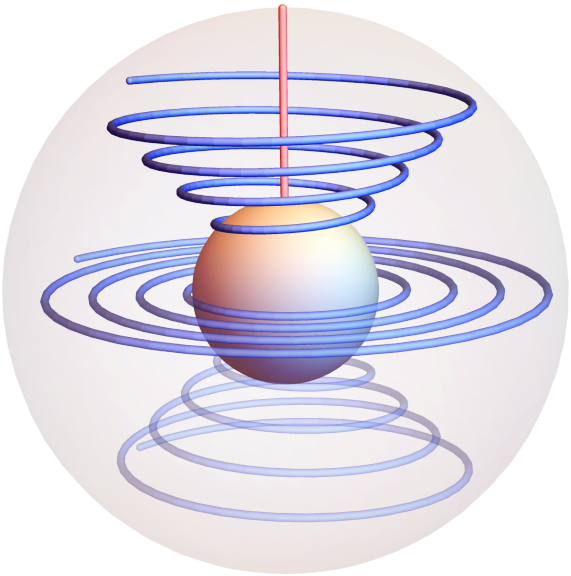

(a)

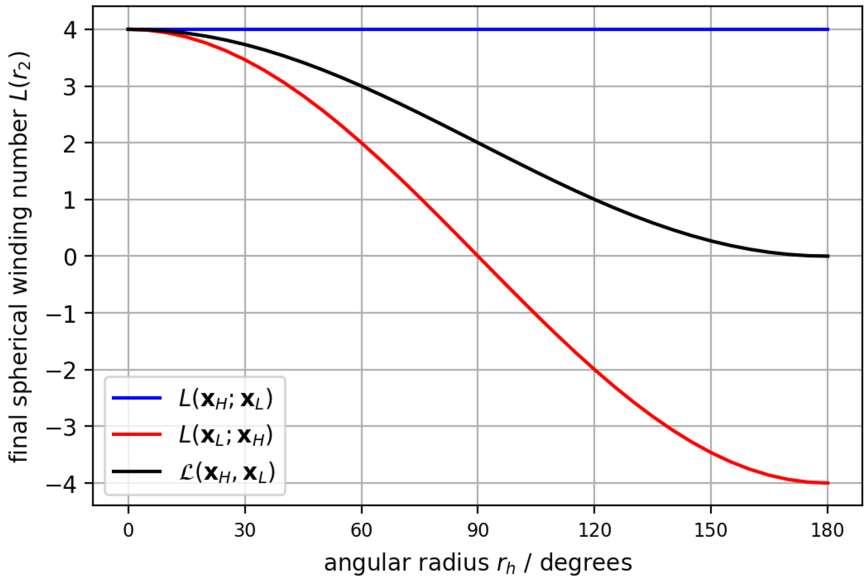

(b)

Figure 3.5: (a) Spherical winding of a helix-line pair both fixed at North. The line $\boldsymbol{x}_L$ is shown in red, and the helix $\boldsymbol{x}_H$ is shown in blue with angular speed $\omega = 2\pi$ and varying angular radius r_h. (b) Final, individual and pairwise spherical winding numbers against the angular radius r_h of the helix.

variation against r_h is also predicted by (3.70) as

$$L(\boldsymbol{x}_L;\boldsymbol{x}_H) = 4\cos r_h, \qquad \text{at} \quad r = r_2\,. \tag{3.72}$$

The fact that $L(\boldsymbol{x}_L;\boldsymbol{x}_H)$ changes signs as r_h varies can be interpreted as the changes in the signs of winding seen from the North as well as the transition for the line to reside "inside" to "outside" of the helix. Both observations indicate the *chiral* nature of helicity, which are summarised in Table 3.2 below:

$L(\boldsymbol{x}_L;\boldsymbol{x}_H)$	r_h	apparent relation of $\boldsymbol{x}_L$ against $\boldsymbol{x}_H$	sign of winding seen from North
positive	$< \pi/2$	inside	positive
0	$= \pi/2$	-	0
negative	$> \pi/2$	outside	negative

Table 3.2: Relationship between spherical winding number and direction of a helix-line pair with the helix radius r_h.

Pairwise or Individual?

Recall that the pairwise spherical winding number $\mathcal{L}(\boldsymbol{x}_H,\boldsymbol{x}_L)$ has been defined to restore the symmetry about both curves. It has another advantage, as we shall demonstrate using a different helix-line pair, shown in Figure 3.6(a). Here, the helix $\boldsymbol{x}_H$ is again fixed at the North, i.e., $(\theta_H,\phi_H) = (0,0)$, with $r_h = \pi/4$ and $\omega = 2\pi$. The radial line $\boldsymbol{x}_L$ is moved continuously along (half-)circles $\phi = 0$ and $\phi = \pi$ such that its polar angle $\theta_L = \theta$ when $\phi_L = 0$ and $\theta_L = 2\pi - \theta$ when $\phi_L = \pi$.

We observe that in Figure 3.6(b) there are discontinuities separating regions of constant winding. The discontinuities at $\theta_L = 45°$ and $315°$ are present in all three which are topologically significant. Their occurrences indicate the transitions of the line from being "inside" to "outside" of the helix, which are topological changes in the configuration.

However, the jumps in the individual winding numbers (in red and blue) at $\theta_L = 135°$ and $225°$ are coordinate artefacts. They are recorded when the line crosses the "mirror" helix or the antipodal image where individual measures are ill-defined, shown in

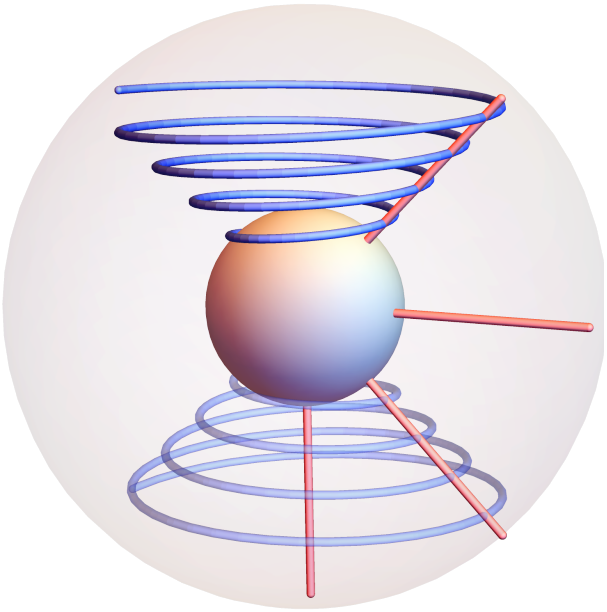

(a)

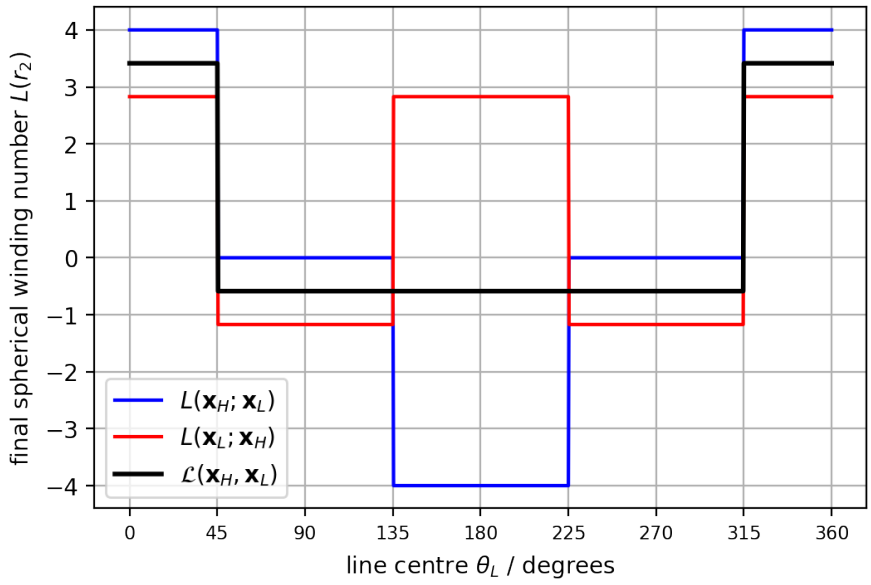

(b)

Figure 3.6: (a) Spherical winding of a helix-line pair, with the line $\boldsymbol{x}_L$ (in red) moved along meridional circles. The helix $\boldsymbol{x}_H$ (in dark blue) of radius $r_h = \pi/4$ is fixed at North, and its antipodal image (in pale blue), i.e., the "mirror" helix, of radius $\tilde{r}_h = \pi - r_h$ is shown. (b) Final, individual and pairwise spherical winding numbers against the position of the line centre θ_L.

Figure 3.6(a). These discontinuities are associated with the well-known failure of a single coordinate system covering the entire sphere.

The pairwise winding number (in black), as the average of individual quantities, remains continuous across $\theta_L = 135°$ and $225°$, since both curves "sense" the equal and opposite jump. This can also be explained from the vanishing values of the pre-factor $(1 + \cos\xi)$ in (3.52) when $\xi = \pi$, i.e., no winding is recorded at the antipodal points.

3.3.2. A "Belt-Trick" Pair

The helix-line example highlighted the properties of spherical winding arising from the non-zero curvature, whereas another distinction is the existence of the *Dirac belt-trick* or *plate-trick*. As shown in 3.7(a), while the blue curve $\boldsymbol{x}_B$ that is initially not entangled with the radial line $\boldsymbol{x}_L$ (in red) in panel (a), the continuous deformation of $\boldsymbol{x}_B$, through panels (b)-(e), makes it winds around $\boldsymbol{x}_L$ almost once at panel (f).

Mathematically, this move corresponds to the fact (e.g., see Bolker 1973) that the special unitary group $\mathrm{SU}(2)$ (which consists of 2×2 unitary matrices with unit determinant) is the double cover of the special orthogonal group $\mathrm{SO}(3)$ (which consists of all 3D rotations). Also, the belt-trick move is the only additional generator of the spherical braid group compared to its Euclidean counterpart (Fadell and Buskirk 1962).

Figure 3.8 plots the changes in the spherical winding numbers as the belt-trick occurs for the parametrisation shown in Figure 3.7. We observe that in Figure 3.8(a) there is a continuous increase of the pairwise winding number $\mathcal{L}$ from approximately 0 to 1, failing to be invariant for a continuous, non-self-intersecting deformation. In contrast, the (pairwise) winding number in the Euclidean case is a topological invariant (cf. §2.3).

This example illustrates the inherent impossibility to define spherical winding measures that depend *only* on the endpoints of curves on the boundary surfaces. However, as we shall prove in Chapter 6, when averaged over all $\boldsymbol{B}$-lines and weighted by magnetic flux, the spherical winding of $\boldsymbol{B}$-lines does yield a dynamical invariant, i.e., the spherical winding helicity $H^{\mathrm{W}}(\boldsymbol{B})$.

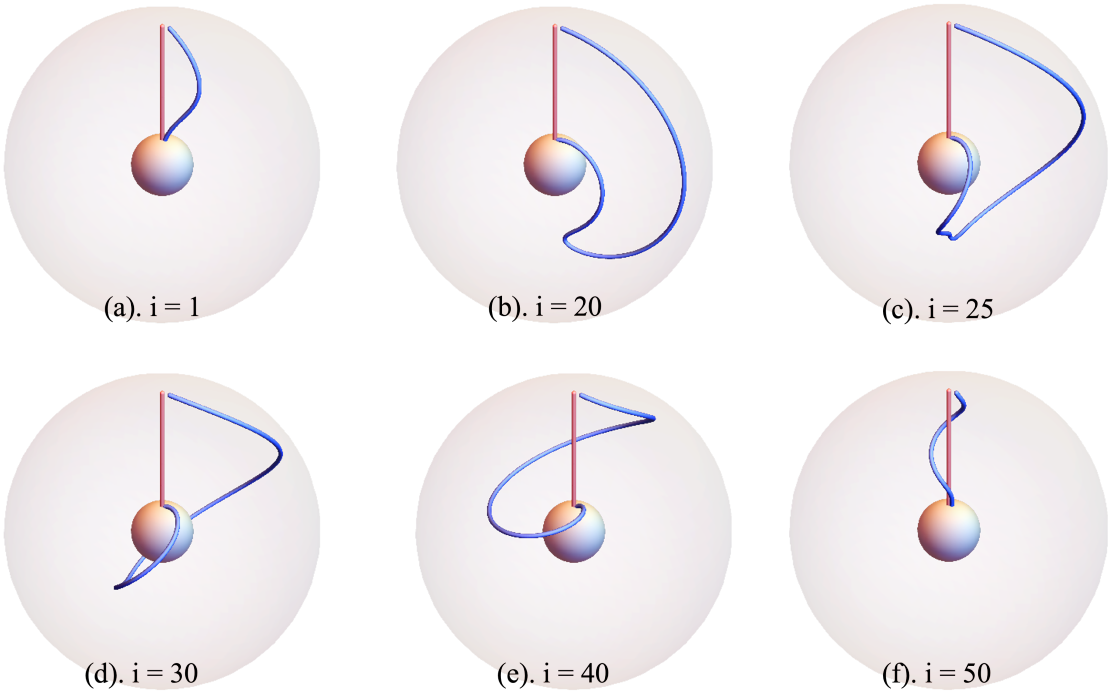

Figure 3.7: Selected snapshots (as labelled in the parameterisation series $i = 1, 2, \cdots, 50$) of the curve $\boldsymbol{x}_B$ (blue) performing the Dirac belt-trick against the radial line $\boldsymbol{x}_L$ (red).

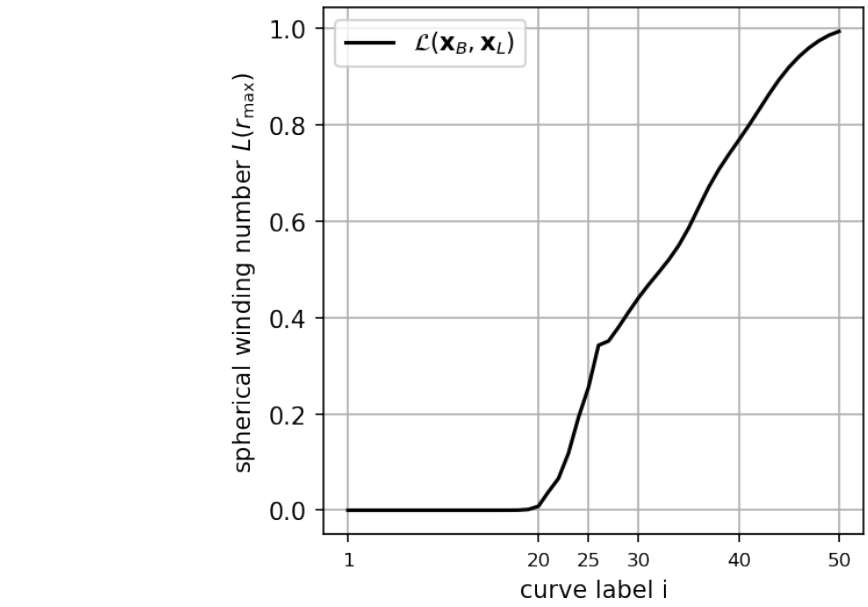

(a)

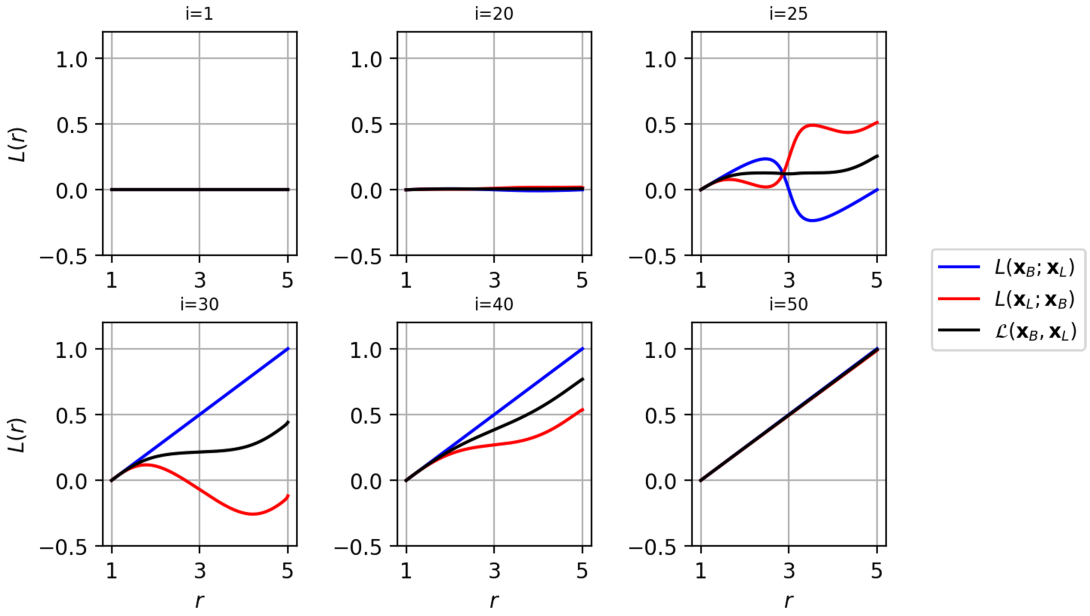

(b)

Figure 3.8: Spherical winding numbers for a belt-trick pair with the belt-trick curve $\boldsymbol{x}_B$ and line $\boldsymbol{x}_L$, calculated for the parameterisation shown in Figure 3.7. Panel (a) plots the final pairwise measure $\mathcal{L}(\boldsymbol{x}_B, \boldsymbol{x}_L)$ against snapshot label i. Panel (b) shows winding numbers, individual and pairwise, against the radial parameter r for the selected snapshots.

Chapter 4

Winding of Open Curves in Periodic Domains

In this chapter[1], we propose a novel definition of winding of open curves in periodic domains, which further generalises the Euclidean and spherical measures discussed in Chapters 2 and 3, respectively. Note that Panagiotou 2015 (see also references therein) attempted to obtain such a quantity using infinite sums of Euclidean winding, although no closed-form expression was found and there were inherent flaws in her argument. While adopting a similar approach, this result will be derived from first principles and supported by fundamental results in complex analysis.

This chapter is organised as follows. §4.1 introduces the periodic domain and characterises its topological properties using de Rham cohomology. In §4.2, we construct the winding rate and winding number of open curves in periodic domains from both infinite sums and the generalised Green's functions for Laplacian, another major result of this thesis. From two toy examples presented in §4.3, we illustrate new features of winding in periodic domains and verify the agreement between analytical and numerical results.

[1]Adapted from Chapter 2, D. Xiao, C. B. Prior, and A. R. Yeates (2024). "Winding and Magnetic Helicity in Periodic Domains". In: *(under review)*.

4.1. A Primer on Periodic Domains

4.1.1. Periodic Domain as Flat 2-Torus

By *periodic domains*, we mean doubly-periodic, identified squares of the form,

$$\mathcal{S} \equiv \{(x, y) : x \sim x + 1, y \sim y + 1\}\,. \tag{4.1}$$

Such a domain can be represented as the space formed by "gluing" two pairs of the opposite edges of the unit square (see e.g., Sutherland 2009), as shown in Figure 4.1(a). Formally, it can be written as the *flat 2-torus*, or the quotient space,

$$\mathcal{S} = \mathbb{E}^2/\mathbb{Z}^2 \equiv \mathbb{T}^2\,, \tag{4.2}$$

inheriting the flat Euclidean metric from $\mathbb{E}^2$.

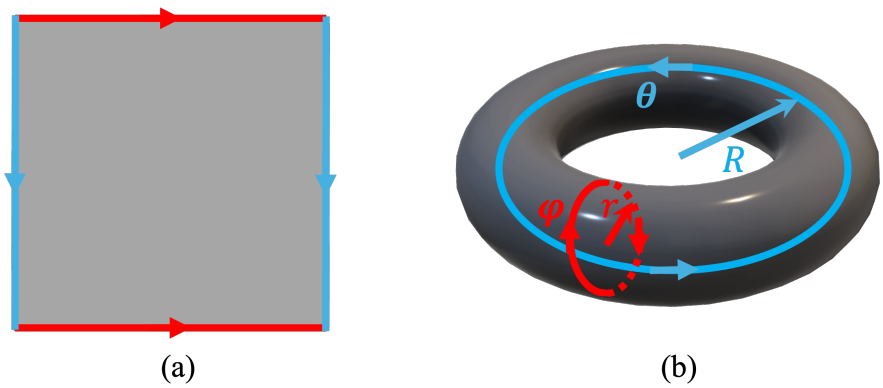

Figure 4.1: (a) A periodic domain $\mathcal{S}$ represented as an identified square and (b) a ring torus in $\mathbb{E}^3$ that is topologically equivalent to $\mathcal{S}$ but has non-vanishing curvature.

Topologically, $\mathcal{S}$ is equivalent to a *ring torus* T in $\mathbb{E}^3$, as shown in Figure 4.1(b), i.e., there exists a continuous deformation $\mathbb{T}^2 \to T$ with continuous inverse. However, the latter has non-vanishing curvature arising from its (e.g., usual) embedding in $\mathbb{E}^3$:

$$T : \begin{pmatrix} x \\ y \\ w \end{pmatrix} = \begin{pmatrix} (R + r\cos\varphi)\cos\theta \\ (R + r\cos\varphi)\sin\theta \\ r\sin\varphi \end{pmatrix}, \tag{4.3}$$

where $\theta, \varphi \in [0, 2\pi)$ are angular parameters around the major radius R and the minor radius $r < R$, respectively. Note that it is impossible for $\mathbb{T}^2$ to be continuously transformed to T while retaining the flat metric, unless some regularity conditions are dropped (see Borrelli et al. 2012 for details).

4.1.2. Topology of Periodic Domains

To characterise the non-trivial topology of periodic domains $\mathbb{T}^2$ in the context of vector fields, the language of *de Rham*[2] *cohomology* is arguably best suited (see e.g., Madsen and Tornehave 1997 for an introduction) and we give a brief overview below. Here, the symbol $=$ is used for the suitable notion of equivalence up to isomorphism.

Let $\Omega(\mathbb{T}^2)$ be the space of smooth, square-integrable vector fields defined on $\mathbb{T}^2$, then, using differential operators div, grad, and curl with their usual meanings, the following subspaces of $\Omega(\mathbb{T}^2)$,

$$H^1(\mathbb{T}^2) \equiv \ker\big[\mathrm{curl}(\mathbb{T}^2)\big] \,/\, \mathrm{im}\big[\mathrm{grad}(\mathbb{T}^2)\big], \tag{4.4}$$

$$H^2(\mathbb{T}^2) \equiv \ker\big[\mathrm{div}(\mathbb{T}^2)\big] \,/\, \mathrm{im}\big[\mathrm{curl}(\mathbb{T}^2)\big], \tag{4.5}$$

are respectively defined as the *first* and *second de Rham cohomology groups* (canonically identified). It suffices, from dimensional arguments, to consider only these two groups which are well-known to be represented as (see e.g., Hatcher 2009)

$$H^1(\mathbb{T}^2) = \mathrm{span}\{\hat{\boldsymbol{e}}_x, \hat{\boldsymbol{e}}_y\}, \tag{4.6}$$

$$H^2(\mathbb{T}^2) = \mathrm{span}\{\hat{\boldsymbol{e}}_w\}; \tag{4.7}$$

[2] Georges de Rham, Swiss, 1903-1990

where $\{\hat{\boldsymbol{e}}_x, \hat{\boldsymbol{e}}_y, \hat{\boldsymbol{e}}_w\}$ are the usual Cartesian basis vectors[3] in $\mathbb{E}^3$.

Indeed, the first and second de Rham cohomology groups can be defined and used to characterise the topology for any two-dimensional surface. Intuitively, (4.6) and (4.7) respectively characterise the space of 1- or 2-dimensional "holes" on $\mathbb{T}^2$ (see e.g., Cantarella, DeTurck, and Gluck 2002). The dimension of H^1 is called the *genus* and is equal to the number of equivalence classes of oriented loops defined therein (see e.g., Hatcher 2009).

Note that both the plane $\mathbb{E}^2$ and the sphere S^2 have trivial topology in the sense that

$$H^1(\mathbb{E}^2) = H^2(\mathbb{E}^2) = \{\mathbf{0}\}\,, \tag{4.8}$$

as a special case of the Poincaré lemma, and

$$H^1(S^2) = H^2(S^2) = \{\mathbf{0}\}\,. \tag{4.9}$$

4.2. Periodic Winding Rates

In this section, we adopt the complex formulation preluded in §2.1.2, i.e., by identifying the Euclidean or non-periodic domain $\mathbb{E}^2$ as $\mathbb{C}$, and planar doubly periodic domain $\mathbb{T}^2$ as

$$\mathcal{S} \equiv \mathbb{C}/\mathbb{Z}[\mathrm{i}]\,, \tag{4.10}$$

where $\mathbb{Z}[\mathrm{i}]$ are the Gaussian integers defined by

$$\mathbb{Z}[\mathrm{i}] \equiv \{n_x + \mathrm{i}n_y : n_x, n_y \in \mathbb{Z}\}\,. \tag{4.11}$$

Note that translation invariance allows us to assume without loss of generality that $\mathcal{S}$ is centred at the origin $z = 0$. Also, recall that the Euclidean winding rate ω_{E} for a single

[3]Recall that the symbol z is reserved for a general complex variable which will be used next.

curve $\gamma : [0,1] \to \mathbb{C} \setminus \{0\}$ against $z = 0$ is given by, cf. (2.8),

$$\omega_{\mathrm{E}}(t;\gamma) = \mathrm{Im}\left(\frac{1}{z}\frac{\mathrm{d}z}{\mathrm{d}t}\right). \tag{4.12}$$

For a pair of curves $\gamma, \gamma' : [0,1] \to \mathbb{C}$ such that $\gamma(t) \neq \gamma'(t)$ for all $t \in [0,1]$, the Euclidean pairwise winding rate $\omega_{\mathrm{E}}(t;\gamma,\gamma')$ is given by, cf. (2.29),

$$\omega_{\mathrm{E}}(t;\gamma,\gamma') \equiv \frac{1}{2}[\omega_{\mathrm{E}}(t;\gamma-\gamma') + \omega_{\mathrm{E}}(t;\gamma'-\gamma)] = \omega_{\mathrm{E}}(t;\gamma-\gamma') = \omega_{\mathrm{E}}(t;\gamma'-\gamma)\,. \tag{4.13}$$

4.2.1. Winding Rates from Infinite Sums

Given a curve $\gamma : [0,1] \to \mathcal{S} \setminus \{0\}$ and for any $n \in \mathbb{Z}[\mathrm{i}]$, a *periodic image* γ_n of γ is defined as

$$\gamma_n \equiv \gamma + n : [0,1] \to \mathbb{C} \setminus \{0\}\,. \tag{4.14}$$

Examples of periodic images are shown in Figure 4.2, which will be investigated in §4.3.

It is intuitive to postulate that the *periodic winding rate*, denoted $\omega_{\mathrm{p}}(t;\gamma)$, of γ about $z = 0$, could be defined as the infinite sum of non-periodic winding $\omega_{\mathrm{E}}(t;\gamma_n)$ over all periodic images γ_n (see e.g., Panagiotou 2015), i.e.,

$$\sum_{n\in\mathbb{Z}[\mathrm{i}]} \mathrm{Im}\left[\frac{1}{z+n}\frac{\mathrm{d}}{\mathrm{d}t}(z+n)\right] = \mathrm{Im}\left[\left(\sum_{n\in\mathbb{Z}[\mathrm{i}]}\frac{1}{z+n}\right)\frac{\mathrm{d}z}{\mathrm{d}t}\right]. \tag{4.15}$$

However, it is known that the infinite sum on the right side of (4.15) is ill-defined, since it converges only conditionally (Conway 1978) so it can yield *arbitrary* values by changing the summation order. To retain the winding-generating singular behaviour of (4.15) while ensuring finiteness and single-valuedness, we can apply the Mittag-Leffler theorem (ibid.) so that

$$\sum_{n\in\mathbb{Z}[\mathrm{i}]}\frac{1}{z+n} \xrightarrow{\text{M.-L.}} \zeta(z) \equiv \frac{1}{z} + \sum_{\substack{n\in\mathbb{Z}[\mathrm{i}]\\ n\neq 0}}\left(\frac{1}{z-n} + \frac{1}{n} + \frac{z}{n^2}\right), \tag{4.16}$$

where $\zeta(z)$ is the *Weierstrass zeta function* defined on $\mathcal{S}$ (Whittaker and Watson 1996). The additional terms now guarantee absolute and uniform convergence.

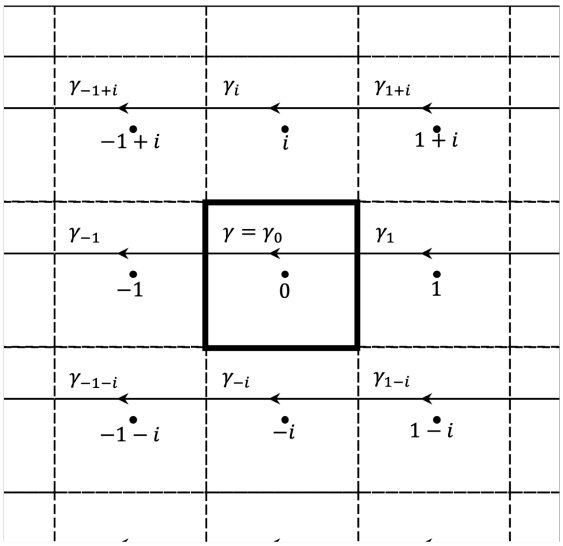

(a). Line-point winding
$\gamma: z = -t + 0.5 + 0.25i$

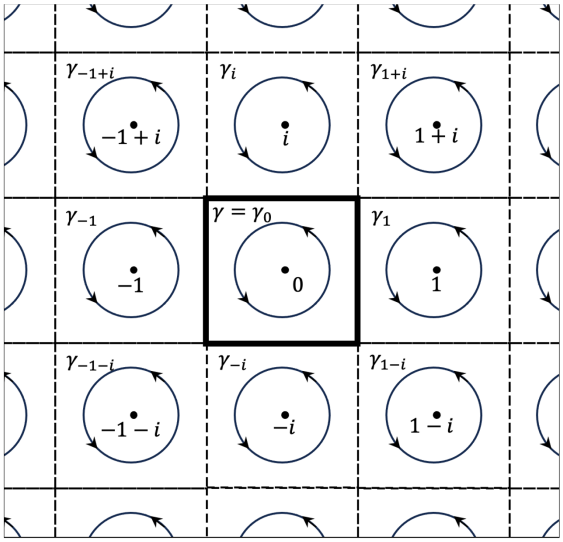

(b). Circle-point winding
$\gamma: z = 0.25e^{2\pi it}$

Figure 4.2: Periodic images γ_n of the curve γ for examples of (a) line-point and (b) circle-point winding in the planar periodic domain $\mathcal{S}$ (marked by the bold outline).

Geometrically, O'Neil 1989 showed that $\zeta(z)$ is equivalent to the limit of a finite sum over $C_R \equiv \{|z| \leq R\}$ with $R \to \infty$:

$$\zeta(z) = \lim_{R\to\infty} \sum_{\substack{n\in\mathbb{Z}[\mathrm{i}] \\ |n|<R}} \frac{1}{z+n}\,. \tag{4.17}$$

The radially symmetric order of summation is necessary for the above equality to hold and it is implicitly assumed (without justification) in Panagiotou 2015.

A further modification is necessary due to the compactness of $\mathcal{S}$, which was overlooked either in ibid. Note that (4.16) still fails to be doubly periodic due to Legendre's relations (Whittaker and Watson 1996) on $\mathcal{S}$:

$$\zeta(z+1) = \zeta(z) + \pi\,, \qquad \zeta(z+\mathrm{i}) = \zeta(z) - \pi\mathrm{i}\,. \tag{4.18}$$

To restore periodicity, we need to remove a linear gradient $\pi\bar{z}$ from $\zeta(z)$ so that,

$$\zeta(z) \longrightarrow \zeta(z) - \pi\bar{z}\,, \tag{4.19}$$

which is also the unique, non-trivial term that can be added due to Liouville's theorem. In crystallography literature, e.g., Poulton et al. 1999, the extra term $-\pi\bar{z}$ is referred to as the existence of a uniform background of counter-source, or "jellium", to neutralise the effect of the source at $z = 0$. Alternatively, it is interpreted as compensation for the far-field contribution of the finite sum (4.17) (Goncharov and Gryanik 1986).

In summary, the naïve sum (4.15) should be modified to give the *periodic winding rate* $\omega_{\mathrm{p}}(t;\gamma)$ as

$$\omega_{\mathrm{p}}(t;\gamma) \equiv \mathrm{Im}\left[\left(\zeta(z) - \pi\bar{z}\right)\frac{\mathrm{d}z}{\mathrm{d}t}\right]. \tag{4.20}$$

Using (4.17), it can be written in terms of the Euclidean or non-periodic winding rates ω_{E}, (4.12), as follows:

$$\omega_{\mathrm{p}}(t;\gamma) = \lim_{R\to\infty} \sum_{\substack{n\in\mathbb{Z}[\mathrm{i}] \\ |n|<R}} \left[\left(1 - \frac{\pi|z+n|^2}{N_R}\right)\omega_{\mathrm{E}}(t;\gamma_n)\right], \tag{4.21}$$

where,

$$N_R = \pi R^2 + O(R^{14/22}) \,, \tag{4.22}$$

is the number of lattice points within C_R (see Hensley 1994 for details).

For curves $\gamma, \gamma' : [0,1] \to \mathcal{S}$ such that $\gamma(t) \neq \gamma'(t)$ for all $t \in [0,1]$, the *pairwise periodic winding rate* $\omega_{\mathrm{p}}(t;\gamma,\gamma')$ can be similarly defined as

$$\omega_{\mathrm{p}}(t;\gamma,\gamma') \equiv \frac{1}{2}\big[\omega_{\mathrm{p}}(t;\gamma-\gamma') + \omega_{\mathrm{p}}(t;\gamma'-\gamma)\big] \,, \tag{4.23}$$

which is manifestly symmetric in γ and γ'. Also, translation invariance ensures that (4.23) is well-defined. From (4.20), we have

$$\omega_{\mathrm{p}}(t;\gamma-\gamma') = \omega_{\mathrm{p}}(t;\gamma'-\gamma) \,, \tag{4.24}$$

so that

$$\omega_{\mathrm{p}}(t;\gamma,\gamma') = \omega_{\mathrm{p}}(t;\gamma-\gamma') = \omega_{\mathrm{p}}(t;\gamma'-\gamma) \,. \tag{4.25}$$

We thus constructed the periodic analogue of winding rates of open curves, (4.20) and (4.23), providing further generalisations to the Euclidean measures, (4.12) and (4.13).

4.2.2. Winding Rates from Generalised Green's Functions for Laplacians

Recall that both the Euclidean and spherical winding rates can be written in terms of the respective (generalised) Green's function for Laplacians (cf. §2.2.2 and 3.2.3). Here, we demonstrate that their periodic counterpart can be similarly interpreted. Recall that the Euclidean Green's function $G_{\mathrm{E}}(z,z')$ for the Laplacian in $\mathbb{E}^2 = \mathbb{C}$ is defined as the solution to the Poisson's equation:

$$\Delta_z G_{\mathrm{E}}(z,z') = \delta(z-z') \,, \tag{4.26}$$

and the periodic Green's function $G_{\mathrm{p}}(z, z')$ for the same Laplacian[4] in $\mathcal{S} = \mathbb{C}/\mathbb{Z}[\mathrm{i}]$:

$$.\Delta_z G_{\mathrm{p}}(z, z') = \delta(z - z') - \frac{1}{\mathrm{Area}(\mathcal{S})}\,. \tag{4.27}$$

Here, $\delta(z - z')$ is the Dirac function with the singularity located at $z = z'$ and,

$$\Delta_z = 4\partial_z\partial_{\bar{z}} = 4\partial_{\bar{z}}\partial_z\,, \tag{4.28}$$

is the Laplacian with respect to z. Also, the Wirtinger[5] derivatives ∂_z and $\partial_{\bar{z}}$ are defined as

$$\partial_z \equiv \frac{1}{2}(\partial_x - \mathrm{i}\partial_y)\,, \qquad \partial_{\bar{z}} \equiv \frac{1}{2}(\partial_x + \mathrm{i}\partial_y)\,. \tag{4.29}$$

Since $\mathcal{S}$ is compact and boundaryless and any constant function corresponds to the zero eigenvalue of the Laplacian (see §3.2.3 for a detailed introduction), it is more precise to refer $G_{\mathrm{p}}(z, z')$ as the *generalised* (Courant and Hilbert 1989), or *source-neutral* (Poulton et al. 1999), *Green's function*. Also, the inclusion of the term $1/\mathrm{Area}(\mathcal{S}) = 1$ guarantees compatibility due to Stokes' theorem, i.e.,

$$\int_{\mathcal{S}} G_{\mathrm{p}}(z, z')\ \mathrm{d}A_z = 0\,, \tag{4.30}$$

where $\mathrm{d}A_z = \mathrm{d}\bar{z} \wedge \mathrm{d}z\,/(2\mathrm{i})$ is the area form on $\mathbb{C}$ as the complex equivalent of $\mathrm{d}A = \mathrm{d}x \wedge \mathrm{d}y$.

Explicit expressions of $G_{\mathrm{E}}(z, z')$ and $G_{\mathrm{p}}(z, z')$ are given by, e.g., Lin and Wang 2010:

$$G_{\mathrm{E}}(z, z') = \frac{1}{2\pi}\log|z - z'|\,, \tag{4.31}$$

$$G_{\mathrm{p}}(z, z') = \frac{1}{2\pi}\log|\vartheta_1(z - z')| - \frac{1}{2}[\mathrm{Im}(z - z')]^2\,; \tag{4.32}$$

[4] since, by definition, $\mathbb{T}^2$ has no curvature.
[5] Wilhelm Wirtinger, Austrian, 1865-1945

where $\vartheta_1(z)$ is the *first Jacobi theta function* on $\mathcal{S}$, e.g., Whittaker and Watson 1996,

$$\vartheta_1(z) \equiv 2\sum_{n=0}^{\infty}(-1)^n \mathrm{e}^{-\pi(n+\frac{1}{2})^2}\sin\left[(2n+1)\pi z\right] \tag{4.33}$$

$$\propto z\prod_{n=1}^{\infty}\left(1-\frac{z^2}{n^2}\right)[1-\mathrm{e}^{2\pi\mathrm{i}(z-n\mathrm{i})}][1-\mathrm{e}^{2\pi\mathrm{i}(z+n\mathrm{i})}]\,. \tag{4.34}$$

As (4.31) and (4.32) are translation invariant and symmetric in z and z', one can set $(z-z')\to z$ and regard both (generalised) Green's functions as univariate without ambiguity. Also, their derivatives given by, e.g., ibid.,

$$4\pi\partial_z G_{\mathrm{E}}(z) \;=\; \frac{1}{z}\,, \tag{4.35}$$

$$4\pi\partial_z G_{\mathrm{p}}(z) \;=\; \zeta(z)-\pi\bar{z}\,. \tag{4.36}$$

For reference, (4.35) and (4.36) are visualised in Figure 4.3.

Comparing (4.35) with (4.12) and (4.36) with (4.20), the periodic (with subscript $\mathrm{k}=\mathrm{p}$) and Euclidean or non-periodic (with subscript $\mathrm{k}=\mathrm{E}$) winding rates can be unified into a single expression:

$$\omega_{\mathrm{k}}(t;\gamma) = 4\pi\,\mathrm{Im}\left[\partial_z G_{\mathrm{k}}(z)\frac{\mathrm{d}z}{\mathrm{d}t}\right]. \tag{4.37}$$

We can also define its integral as the *(pairwise) winding number*, denoted $L_{\mathrm{k}}(\gamma)$, as

$$L_{\mathrm{k}}(\gamma) \equiv \frac{1}{2\pi}\int_0^1 \omega_{\mathrm{k}}(t;\gamma)\;\mathrm{d}t\;, \tag{4.38}$$

where the factor of $1/(2\pi)$ is customary[6]. Using (4.37), it follows that

$$L_{\mathrm{k}}(\gamma) = 2\,\mathrm{Im}\int_\gamma \partial_z G_{\mathrm{k}}(z)\;\mathrm{d}z\;. \tag{4.39}$$

[6]This is because L yields integer values for closed curves; see also §2.3.

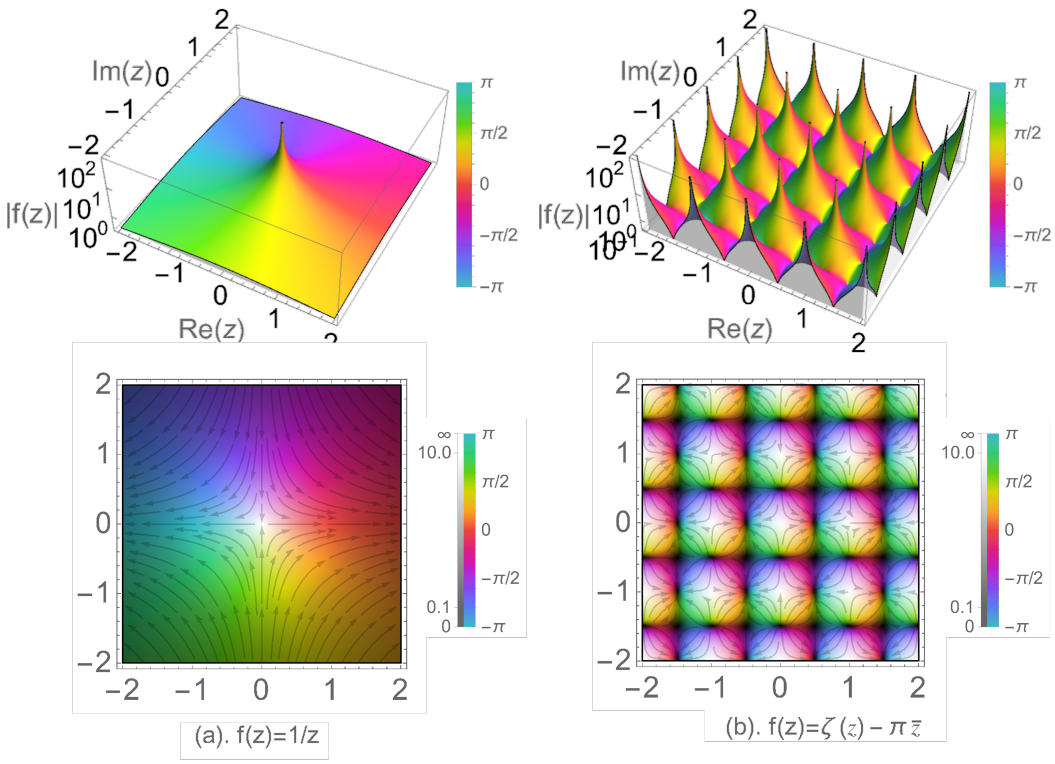

Figure 4.3: 3D (top row) and 2D/streamline (bottom row) plots of derivatives of (generalised) Green's functions (4.35)-(4.36) used in (4.37). Colours and grey shades respectively indicate the complex phase and modulus.

4.3. Examples of Winding in Periodic Domains

In this section, we compute periodic and non-periodic winding quantities for the examples in Figure 4.2, i.e., winding of either a line (§4.3.1) or a circle (§4.3.2) about $z = 0$ (formally also a line as $\{z = 0\} \times [0, 1]$). The winding numbers computed numerically all agree with the analytical calculations from (4.39). We remark, however, that in both examples, L_p is not invariant under continuous, non-intersecting deformations of the curves (cf. §2.3), which illustrates the peculiarities of winding in periodic domains.

4.3.1. A Line-Point Pair

Certain lines cannot be continuously contracted to a point in periodic domains, which manifests the non-trivial domain topology and will later be associated with the non-vanishing harmonic fluxes in §5. Here, we consider horizontal lines γ of the form,

$$\gamma : z = -t + 0.5 + \mathrm{i}a\,, \quad \text{where} \quad t \in [0, 1]\,, \tag{4.40}$$

and $a \in [-0.5, 0.5] \setminus \{0\}$ is the vertical position, and investigate their periodic and non-periodic winding about $z = 0$. The case $a = 0.25$ is shown in Figure 4.2(a), and relevant winding quantities are computed and plotted in Figure 4.4.

With $\mathrm{d}z/\mathrm{d}t = -1$, winding rates ω_p and ω_E are respectively the imaginary parts of (4.35) and (4.36), up to a sign. We observe from Figure 4.4(a) that $|\omega_\mathrm{p}| < |\omega_\mathrm{E}|$, which could be interpreted as the "localising effect" due to periodicity. Such an effect is most significant at $a = \pm 0.5$, when γ simultaneously traverses the lower and upper domain boundaries in opposite directions with the same rate, leading to no overall winding being measured.

The dependence of winding numbers, L_p and L_E, on the line's vertical position a is illustrated in Figure 4.4(b). In the non-periodic case, we have

$$L_\mathrm{E}(a) = \frac{1}{2\pi} \operatorname{Im} \left[\operatorname{Log}(-0.5 + \mathrm{i}a) - \operatorname{Log}(0.5 + \mathrm{i}a)\right] \tag{4.41}$$

$$= \frac{1}{2\pi} \operatorname{Arg}\left(\frac{2\mathrm{i}a - 1}{2\mathrm{i}a + 1}\right). \tag{4.42}$$

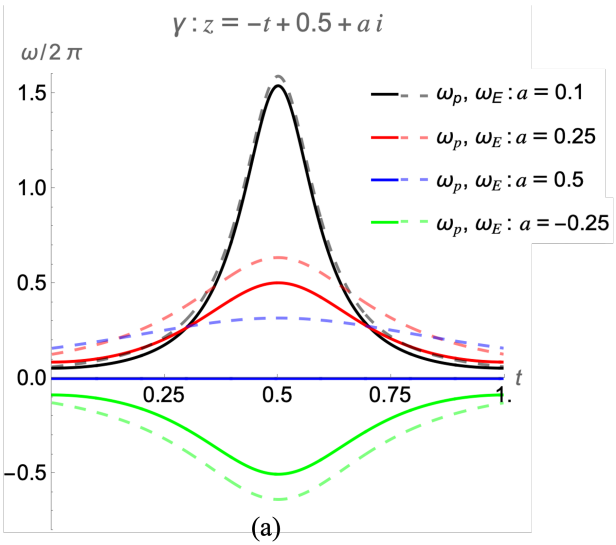

(a)

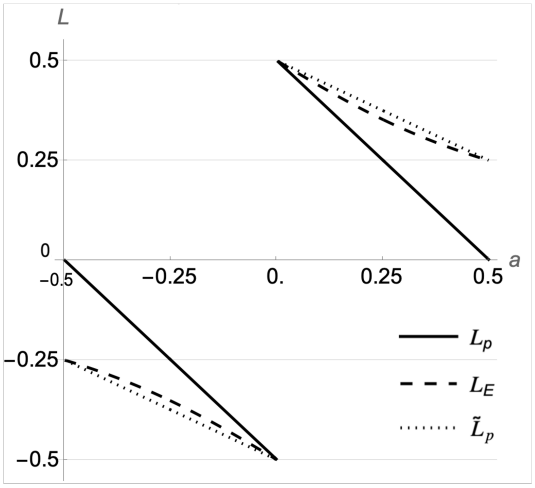

(b)

Figure 4.4: (a). Winding rates $\omega_{\mathrm{p}}, \omega_{\mathrm{E}}$ and (b) winding numbers $L_{\mathrm{p}}, L_{\mathrm{E}}$, of horizontal lines (4.40) against $z = 0$ with vertical positions a. Periodic quantities ω_{p} and L_{p} are plotted in solid lines while non-periodic ones ω_{E} and L_{E} are in dashed lines. For comparison, the quantity $\tilde{L}_{\mathrm{p}}$ from (4.56) is also plotted in panel (b).

The periodic winding number L_p can be computed from the contours shown in Figure 4.5. For $a > 0$, using Cauchy's theorem, we have

$$\int_{\gamma+\gamma_1+\gamma_2+\gamma_-+\gamma_++C_\epsilon} \zeta(z)\,\mathrm{d}z = 0\,, \tag{4.43}$$

since $\zeta(z)$ is analytic within the contour. From parity, i.e., $\zeta(-z) = -\zeta(z)$, it follows that

$$\int_{\gamma_1} \zeta(z)\,\mathrm{d}z = -\int_{\gamma_2} \zeta(z)\,\mathrm{d}z\,. \tag{4.44}$$

From quasi-periodicity (4.18), noting that integration is performed on $\mathbb{C}$, we have

$$\begin{aligned}
\int_{\gamma_+} \zeta(z)\,\mathrm{d}z &= \int_{t=0}^{a} \zeta(0.5+t\mathrm{i})\,\mathrm{i}\,\mathrm{d}t && (4.45)\\
&= \int_{t=0}^{a} \zeta(-0.5+t\mathrm{i}+1)\,\mathrm{i}\,\mathrm{d}t && (4.46)\\
&= \int_{t=0}^{a} \big[\zeta(-0.5+t\mathrm{i})+\pi\big]\,\mathrm{i}\,\mathrm{d}t && (4.47)\\
&= \mathrm{i}a\pi - \int_{t=a}^{0} \zeta(-0.5+t\mathrm{i})\,\mathrm{i}\,\mathrm{d}t && (4.48)\\
&= \mathrm{i}a\pi - \int_{\gamma_-} \zeta(z)\,\mathrm{d}z\,. && (4.49)
\end{aligned}$$

From the indentation lemma[7] and $\mathrm{Res}_{z=0}\zeta(z) = 1$, we have

$$\int_{C_\epsilon} \zeta(z)\,\mathrm{d}z = -\frac{\pi}{2\pi}\cdot 2\pi\mathrm{i} = -\pi\mathrm{i}\,. \tag{4.50}$$

Hence, substituting (4.44)-(4.50) into (4.43) gives

$$\int_{\gamma} \zeta(z)\,\mathrm{d}z = -\mathrm{i}a\pi + \mathrm{i}\pi\,. \tag{4.51}$$

[7]The indentation lemma is a special version of the residue theorem which can be stated as follows. Let f have a simple pole at $z = z_0$ with residue $\mathrm{Res}_{z=z_0}(f)$, then

$$\int_{C_\epsilon} f(z)\,\mathrm{d}z = \mathrm{i}(\theta_1-\theta_0)\mathrm{Res}_{z=z_0}(f)\,,\quad \text{where}\quad C_\epsilon : \theta \mapsto a+\epsilon\mathrm{e}^{\mathrm{i}\theta},\ \theta\in[\theta_0,\theta_1],\ \epsilon\to 0\,.$$

Note that, from a simple parametric integration, we have

$$-\int_\gamma \pi\bar{z}\,\mathrm{d}z = -\pi\int_{t=0}^{1}(-t+0.5-\mathrm{i}a)\,(-\mathrm{d}t) = (0.5-\mathrm{i}a)\pi\,, \tag{4.52}$$

so that

$$L_\mathrm{p}(a) = \frac{1}{2\pi}\,\mathrm{Im}\int_\gamma (\zeta(z)-\pi\bar{z})\;\mathrm{d}z = \frac{1}{2}-a\,. \tag{4.53}$$

The case $a<0$ can be similarly computed with a different contour shown in Figure 4.5(ii),

$$L_\mathrm{p}(a) = -\frac{1}{2}-a\,. \tag{4.54}$$

Combining both (4.53) and (4.54), we have

$$L_\mathrm{p}(a) = \frac{1}{2}\mathrm{sgn}(a)-a\,, \tag{4.55}$$

which agrees with the numerical result shown in Figure 4.4.

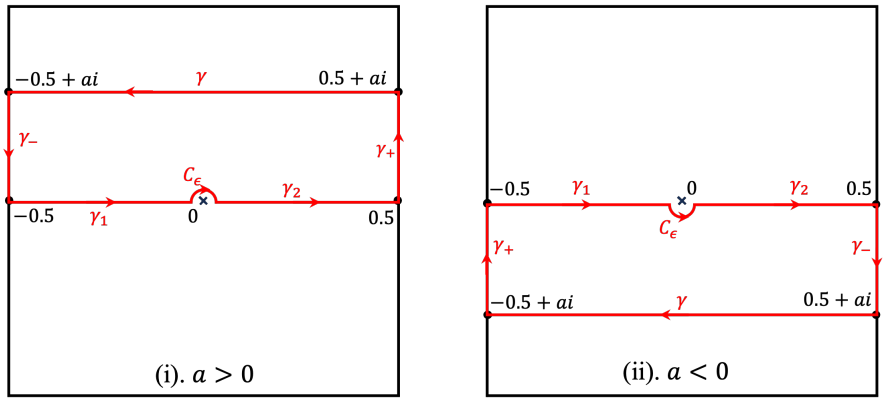

Figure 4.5: Contours used to evaluate $\int_\gamma \zeta(z)\,\mathrm{d}z$ in §4.3.1.

Also, to demonstrate the necessity of including the correction term $-\pi\bar{z}$ for compactness, we also plot the quantity $\tilde{L}_\mathrm{p}$ in Figure 4.4 for comparison, defined by

$$\tilde{L}_\mathrm{p}(a) \equiv L_\mathrm{p}(a) - \frac{1}{2\pi}\int_\gamma -\pi\bar{z}\;\mathrm{d}z = \frac{1}{2}\mathrm{sgn}(a)-\frac{a}{2}\,. \tag{4.56}$$

Note that, at $a=\pm 0.5$, only the domain-specific L_p is continuous, as desired. Meanwhile,

we remark that the discontinuity at $a = 0$ is present in all cases, a result of the reversal of winding direction when the line passes through the origin.

4.3.2. A Circle-Point Pair

Next, we consider circles - the simplest, closed planar curves - of the form,

$$\gamma : z = r\mathrm{e}^{2\pi \mathrm{i} t}\,, \quad \text{where} \quad t \in [0,1]\,, \tag{4.57}$$

with radius $r \in (0, 0.5]$ or $r = 1/\sqrt{2}$, and their periodic and non-periodic winding about $z = 0$. The case $r = 0.25$ is shown in Figure 4.2(b), and relevant winding quantities are computed and plotted in Figure 4.6. In the non-periodic case, one can verify that

$$\omega_{\mathrm{E}} = 2\pi\,, \qquad L_{\mathrm{E}} = 1\,; \tag{4.58}$$

irrespective of the value of r, since γ encircles $z = 0$ exactly once at a constant rate.

In Figure 4.6(a), the periodic winding rate ω_{p} experiences the "localising effect" similar to the line-point case, again due to the imposed periodicity. When $r = 0.5$, we have $\omega_{\mathrm{p}} = 0$ at quarter intervals, i.e., when γ passes through the zeros of $\partial_z G_{\mathrm{p}}$; cf Figure 4.3(b). Geometrically, these instants correspond to the cancellation of simultaneous positive and negative winding generated by the periodic images of γ.

To compute the expression of the periodic winding number L_{p} analytically, consider

$$L_{\mathrm{p}}(r) = \frac{1}{2\pi}\,\mathrm{Im} \oint_{\gamma} \left(\zeta(z) - \pi \bar{z}\right)\,\mathrm{d}z = 1 - \pi r^2\,, \tag{4.59}$$

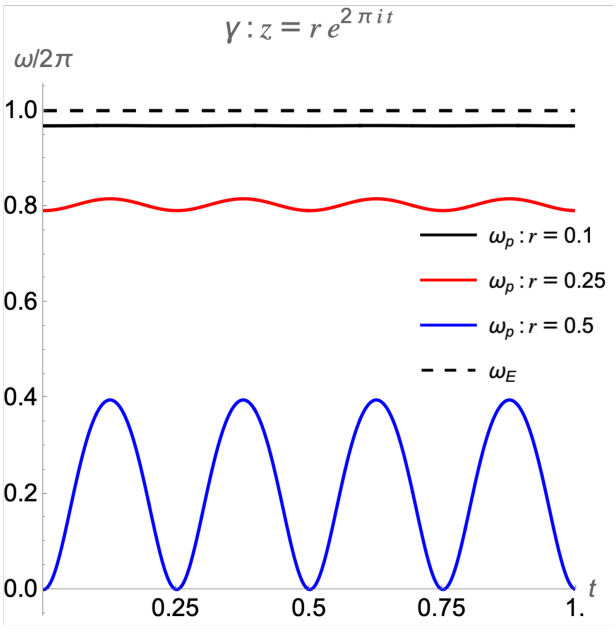

(a)

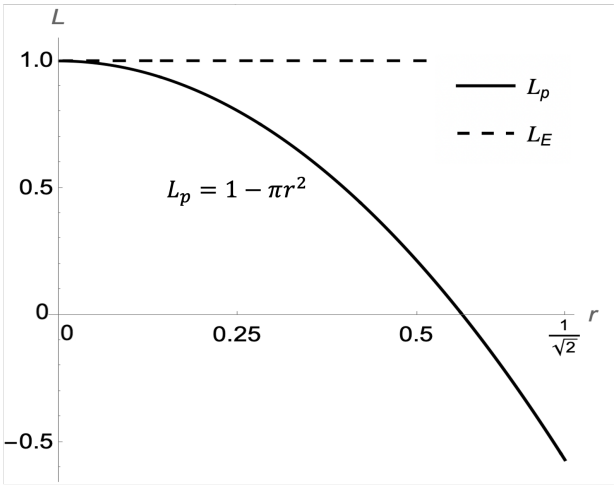

(b)

Figure 4.6: (a). Winding rates $\omega_{\mathrm{p}}, \omega_{\mathrm{E}}$ and (b) winding numbers $L_{\mathrm{p}}, L_{\mathrm{E}}$ of circles (4.57) against $z = 0$ with radius r. Note that $r \in (1/2, 1/\sqrt{2})$ is ill-defined and should be ignored. Periodic quantities ω_{p} and L_{p} are plotted in solid lines while non-periodic ones ω_{E} and L_{E} are in dashed lines.

where

$$\int_\gamma \bar{z}\,\mathrm{d}z = \int_\gamma (x - \mathrm{i}y)(\mathrm{d}x + \mathrm{i}\,\mathrm{d}y) \tag{4.60}$$

$$= \int_\gamma \left[(x - \mathrm{i}y)\,\mathrm{d}x + (y + \mathrm{i}x)\,\mathrm{d}y\right] \tag{4.61}$$

$$= \int_{\mathrm{Int}(\gamma)} \left[\partial_x(y + \mathrm{i}x) - \partial_y(x - \mathrm{i}y)\right]\,\mathrm{d}A \tag{4.62}$$

$$= \int_{\mathrm{Int}(\gamma)} 2\mathrm{i}\,\mathrm{d}A = 2\mathrm{i}A = 2\mathrm{i}\pi r^2\,, \tag{4.63}$$

using Green's theorem at the second last line. Whilst L_p is undefined for $r \in (1/2, \sqrt{2}/2)$ due to the inconsistency in winding directions, we can still compute $L_\mathrm{p} < 0$ at the isolated case $r = \sqrt{2}/2$, realising the "inside-out" transition, or a reversal of the winding direction, described by Berger 1996. This is illustrated in Figure 4.7.

To conclude, both examples demonstrated the non-conservation of winding measures in periodic domains, similar to that in the spherical case (cf. §3.3). We will prove in Chapter 6 that when averaged over all $\boldsymbol{B}$-lines and weighted by magnetic flux we will obtain a meaningful measure of helicity, i.e., $H^\mathrm{W}(\boldsymbol{B})$, the periodic winding helicity, providing an answer to the open question posed by ibid.

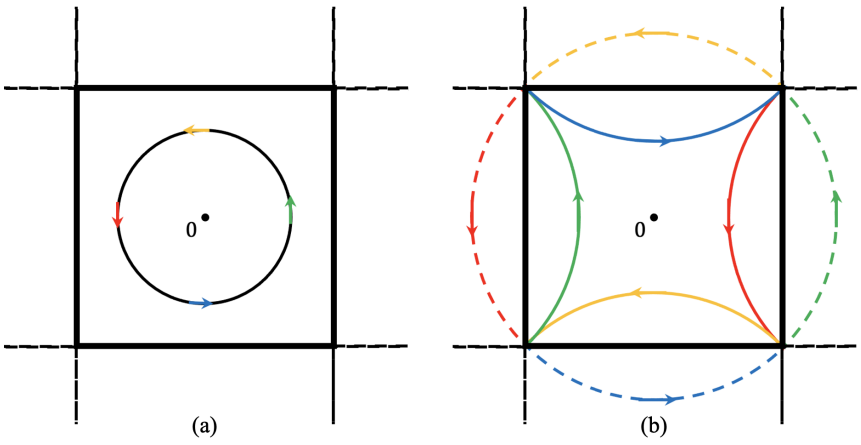

Figure 4.7: A reversal of the direction of winding: (a). counterclockwise when $r < 1/2$ and (b). clockwise when $r = 1/\sqrt{2}$.

Chapter 5

Winding Gauge From the Generalised Poloidal-Toroidal Decomposition

In this chapter[1], we identify a particular choice of vector potential, called the winding gauge. We shall prove in Chapter 6 that open-field magnetic helicity using such a choice acquires the topological interpretation as the total, flux-weighted winding of $\boldsymbol{B}$-lines.

We first introduce, in §5.1, the theoretical foundation of this chapter, i.e., the Hodge Decomposition Theorem for surfaces (Theorem 5.2), as well as its precursor, the Helmholtz Decomposition Theorem (Theorem 5.1). §5.2 presents an *ab initio* derivation of the generalised poloidal-toroidal decomposition of magnetic fields (first proposed and coined in Berger and Hornig 2018), in Euclidean, spherical, and periodic domains. Then, in §5.3, we give definitions of the winding gauge and elaborate on its key properties.

[1]Adapted from Chapter 3 and Appendix A, D. Xiao, C. B. Prior, and A. R. Yeates (2023a). "Spherical winding and helicity". In: *J. Phys. A: Math. Theor.* 56, p. 205201, and Chapter 4, D. Xiao, C. B. Prior, and A. R. Yeates (2024). "Winding and Magnetic Helicity in Periodic Domains". In: *(under review)*; unless otherwise stated.

5.1. Decomposition Theorems for Vector Fields

5.1.1. Helmholtz Decomposition Theorem

In 1858, in studying motions of an ideal fluid[2], German physicist Hermann von Helmholtz (1821-1894) proposed a method for decomposing vector fields in $\mathbb{E}^3$ in his seminal work Helmholtz 1858, later known as the *Helmholtz Decomposition Theorem*. In modern terms, it can be stated as follows, e.g., Arfken and Weber 2005; Cantarella, DeTurck, and Gluck 2002,

Theorem 5.1 (Helmholtz Decomposition Theorem). *Any smooth vector field $\boldsymbol{f}(\boldsymbol{x})$ in $\mathbb{E}^3$ satisfying the following far-field boundary conditions,*

$$[\boldsymbol{\nabla}\cdot\boldsymbol{f}]_\infty = 0\,, \qquad [\boldsymbol{\nabla}\times\boldsymbol{f}]_\infty = \boldsymbol{0}\,, \tag{5.1}$$

may be uniquely decomposed as the sum of divergence-free (or solenoidal) and curl-free[3] (or irrotational) components (in this order):

$$\boldsymbol{f} = -\boldsymbol{\nabla}\phi + \boldsymbol{\nabla}\times\boldsymbol{A}\,, \tag{5.2}$$

where ϕ and $\boldsymbol{A}$ are, respectively, the scalar *and* vector potentials *given by*

$$\phi(\boldsymbol{x}) = \int_V \frac{\boldsymbol{\nabla}'\cdot\boldsymbol{f}(\boldsymbol{x}')}{4\pi|\boldsymbol{x}-\boldsymbol{x}'|}\,\mathrm{d}^3\boldsymbol{x}'\,, \tag{5.3}$$

$$\boldsymbol{A}(\boldsymbol{x}) = \int_V \frac{\boldsymbol{\nabla}'\times\boldsymbol{f}(\boldsymbol{x}')}{4\pi|\boldsymbol{x}-\boldsymbol{x}'|}\,\mathrm{d}^3\boldsymbol{x}'\,. \tag{5.4}$$

Conversely, in any simply connected region $V\subset\mathbb{R}^3$ with smooth boundary ∂V, a smooth vector field $\boldsymbol{f}$ is uniquely determined by its divergence, $\boldsymbol{\nabla}\cdot\boldsymbol{f}$, and its curl, $\boldsymbol{\nabla}\cdot\boldsymbol{f}$, within V, as well as its normal boundary component, $\hat{\boldsymbol{n}}\cdot\boldsymbol{f}\big|_{\partial V}$.

[2] for which the fluid is incompressible and has no viscosity.

[3] Note that the concept of "curl" (in German: Rotation or Rotor) was introduced by von Helmholtz to describe the local rotations of ideal fluid elements.

Note that the Green's function for the 3D Laplacian $\Delta = \partial_x^2 + \partial_y^2 + \partial_w^2$ in $\mathbb{E}^3$ is given by

$$G(\boldsymbol{x}, \boldsymbol{x}') = \frac{1}{4\pi}|\boldsymbol{x} - \boldsymbol{x}'|\,, \tag{5.5}$$

which features in (5.3) and (5.4) as integral kernels. Later, von Helmholtz's work was translated by Tait[4] and published as Helmholtz 1867, which attracted considerable attention to his contemporaries including James Clark Maxwell and Lord Kelvin[5]. This led to the birth of vortex dynamics and later topological fluid dynamics in which helicity plays a central rôle (see Moffatt 2010 for a review).

It is worth mentioning that, in Helmholtz 1858, von Helmholtz also introduced the topological concepts of simple and multiple connectivity (of a three-dimensional domain), while Riemann[6] proposed almost identical ideas in his doctoral thesis on complex analysis in 1851 (now published in English as Riemann 2013). This provides an early example of the affinity between these branches of mathematics.

5.1.2. Hodge Decomposition Theorem for Surfaces

Closely related to the Helmholtz Decomposition Theorem and often regarded as an indirect generalisation, Hodge[7] proposed a more general theory on the orthogonal decomposition of differential forms[8] on Riemannian manifolds in Hodge 1941. A version of the Hodge Decomposition Theorem that suffices our needs can be stated as follows, e.g., Reusken 2018; Schuck and S. K. Antiochos 2019,

Theorem 5.2 (Hodge Decomposition Theorem). *Any smooth, square-integrable vector field $\boldsymbol{f}(\boldsymbol{x})$ in $\mathbb{E}^3$ restricted on a smooth surface $\mathcal{S} \subset \mathbb{E}^3$ (with unit outwards normal $\hat{\mathbf{n}}$) may be uniquely decomposed as a the sum of a normal component and a tangential component (in this order):*

$$\boldsymbol{f} = \boldsymbol{f}_n + \boldsymbol{f}_{\mathcal{S}}\,, \tag{5.6}$$

[4] Peter Guthrie Tait, Scottish, 1831-1901
[5] William Thomson, 1st Baron Kelvin, British, 1824-1907.
[6] Bernhard Riemann, German, 1826-1866.
[7] William Vallance Douglas Hodge, English, 1903-1975.
[8] as coordinate-independent generalisations for vector fields. Interested readers are referred to the self-contained introduction Schleifer 1983.

where

$$\boldsymbol{f}_n \equiv \hat{\boldsymbol{n}} f_n \,, \quad \textit{with} \quad f_n \equiv \hat{\boldsymbol{n}} \cdot \boldsymbol{f}; \tag{5.7}$$

and

$$\boldsymbol{f}_{\mathcal{S}} \equiv (\hat{\boldsymbol{n}} \times \boldsymbol{\nabla}_{\mathcal{S}} \phi + \boldsymbol{\nabla}_{\mathcal{S}} \psi + \boldsymbol{\Omega}_{\mathcal{S}}) \,, \tag{5.8}$$

with

$$\Delta_{\mathcal{S}} \phi \equiv \hat{\boldsymbol{n}} \cdot \boldsymbol{\nabla} \times \boldsymbol{f} \,, \tag{5.9}$$

$$\Delta_{\mathcal{S}} \psi \equiv \boldsymbol{\nabla}_{\mathcal{S}} \cdot \boldsymbol{f}_{\mathcal{S}} \,, \tag{5.10}$$

$$\boldsymbol{\Omega}_{\mathcal{S}} \equiv \boldsymbol{f}_{\mathcal{S}} - \hat{\boldsymbol{n}} \times \boldsymbol{\nabla}_{\mathcal{S}} \phi - \boldsymbol{\nabla}_{\mathcal{S}} \psi \,. \tag{5.11}$$

The relevant surface differential operators for any vector field $\boldsymbol{g}$ and scalar field h on $\mathcal{S}$ are defined as follows:

$$\boldsymbol{\nabla}_{\mathcal{S}} h \equiv \boldsymbol{\nabla} h - \hat{\boldsymbol{n}} (\hat{\boldsymbol{n}} \cdot \boldsymbol{\nabla} h) \,, \tag{5.12}$$

$$\boldsymbol{\nabla}_{\mathcal{S}} \cdot \boldsymbol{g} \equiv \boldsymbol{\nabla} \cdot \boldsymbol{g} - \hat{\boldsymbol{n}} \cdot \frac{\partial \boldsymbol{g}}{\partial n} \,, \tag{5.13}$$

$$\Delta_{\mathcal{S}} h \equiv \boldsymbol{\nabla}_{\mathcal{S}} \cdot \boldsymbol{\nabla}_{\mathcal{S}} h \,. \tag{5.14}$$

Here, $\boldsymbol{\nabla}_{\mathcal{S}}$ is called the *surface gradient* and $\Delta_{\mathcal{S}}$ is called the *surface Laplacian*. For simply-connected surfaces, e.g., Euclidean planes $\mathcal{S} = \mathbb{E}^2$ or spheres $\mathcal{S} = S^2$, one must have (see e.g., Reusken 2018)

$$\boldsymbol{\Omega}_{\mathcal{S}} = \boldsymbol{0} \,. \tag{5.15}$$

In contrast, for general, possibly multiply-connected, surfaces $\mathcal{S}$, we have

$$\boldsymbol{\Omega}_{\mathcal{S}} \in H^1(\mathcal{S}) \,, \tag{5.16}$$

where $H^1(\mathcal{S})$ is the first de Rham cohomology group of $\mathcal{S}$ (cf. §4.1.2). For $\mathcal{S} = \mathbb{T}^2$,

$$\boldsymbol{\Omega}_{\mathcal{S}} = a \hat{\boldsymbol{e}}_x + b \hat{\boldsymbol{e}}_y \,, \tag{5.17}$$

where $a, b \in \mathbb{R}$ are constants, and $\hat{\boldsymbol{e}}_x, \hat{\boldsymbol{e}}_y$ are the horizontal Cartesian unit vectors.

5.2. Generalised Poloidal-Toroidal Decomposition

The *poloidal-toroidal decomposition* of magnetic fields (Chandrasekhar and Kendall 1957) has been widely used in physics in Cartesian and spherical coordinates (see e.g., reviews in Backus 1958 and §2.3.2 in Moffatt and Dormy 2019). A major extension for domains foliated by simply-connected surfaces was proposed in Berger and Hornig 2018, coined as *generalised poloidal-toroidal decomposition*. In this section, using Theorem 5.2, we present a novel derivation based on the Hodge-decomposed of magnetic vector potentials (cf. §5.2.2 for a thorough treatment), and provide a generalisation to ibid. to domains foliated by multiply-connected surfaces.

5.2.1. Overview & Statement

Throughout this thesis, *foliated domains* V are domains of the following form

$$V \equiv \mathcal{S}_t \times [t_1, t_2] \,, \tag{5.18}$$

i.e., a trivial foliation of identical, two-dimensional surfaces $\mathcal{S}$ parameterised continuously by $t \in [t_1, t_2]$. In particular, we consider the following three types of surfaces $\mathcal{S}$:

(i) Euclidean/non-periodic domains V_{E} foliated by planes $\mathcal{S} = \mathbb{E}^2$ along $\hat{\boldsymbol{n}} = \hat{\boldsymbol{e}}_w$;

(ii) Spherical domains V_{s} foliated by spherical surfaces $\mathcal{S} = S^2$ along $\hat{\boldsymbol{n}} = \hat{\boldsymbol{e}}_r$;

(iii) Periodic domains V_{p} foliated by doubly periodic squares $\mathcal{S} = \mathbb{T}^2$ along $\hat{\boldsymbol{n}} = \hat{\boldsymbol{e}}_w$.

We define the *surface integral* $\langle f \rangle_{\mathcal{S}}$ (or $\langle \boldsymbol{v} \rangle_{\mathcal{S}}$) for any scalar field f (or vector field $\boldsymbol{v}$, viewed as Euclidean restrictions, same below) on $\mathcal{S}$ as

$$\langle f \rangle_{\mathcal{S}} \equiv \int_{\mathcal{S}} f \, \mathrm{d}A \,, \qquad \langle \boldsymbol{v} \rangle_{\mathcal{S}} \equiv \int_{\mathcal{S}} \boldsymbol{v} \, \mathrm{d}A \,; \tag{5.19}$$

which can be understood as the surface average (up to a constant factor). Also, we define the L^2-*inner product* $\langle \boldsymbol{u}, \boldsymbol{v} \rangle$ for any vector fields $\boldsymbol{u}$ and $\boldsymbol{v}$ on $\mathcal{S}$ as

$$\langle \boldsymbol{u}, \boldsymbol{v} \rangle_{\mathcal{S}} = \langle \boldsymbol{u} \cdot \boldsymbol{v} \rangle_{\mathcal{S}} \,. \tag{5.20}$$

Specifically for the periodic domain V_{p} (which could be generalised to other multiply-connected domains), we define the *harmonic flux*, or *zero-mode*, of a vector field $\boldsymbol{v}$, denoted $\boldsymbol{v}_0 \in H^1(V_{\mathrm{p}})$, as

$$\boldsymbol{v}_0(w) \equiv \langle \hat{\boldsymbol{e}}_x \cdot \boldsymbol{v} \rangle_{\mathcal{S}_w} \hat{\boldsymbol{e}}_x + \langle \hat{\boldsymbol{e}}_y \cdot \boldsymbol{v} \rangle_{\mathcal{S}_w} \hat{\boldsymbol{e}}_y \,, \tag{5.21}$$

where $\mathcal{S}_w \equiv \mathbb{T}^2 \times \{w\}$ is the foliating surface at height w.

Then, we are ready to state the *generalised poloidal-toroidal decomposition for magnetic fields*, as follows:

Theorem 5.3 (Generalised Poloidal-Toroidal Decomposition for Magnetic Fields; Berger and Hornig 2018; Xiao, Prior, and Yeates 2023a, 2024). *Any magnetic field* $\boldsymbol{B}(\boldsymbol{x})$ *can be uniquely decomposed as*

$$\boldsymbol{B}(\boldsymbol{x}) = \begin{cases} \boldsymbol{B}_T(\boldsymbol{x}) + \boldsymbol{B}_P(\boldsymbol{x}) \,, & \text{for } V = V_{\mathrm{E}} \text{ or } V_{\mathrm{s}} \,; \\ \boldsymbol{B}_T(\boldsymbol{x}) + \boldsymbol{B}_P(\boldsymbol{x}) + \boldsymbol{B}_0(w) \,, & \text{for } V = V_{\mathrm{p}} \,. \end{cases} \tag{5.22}$$

Here, the toroidal field component $\boldsymbol{B}_T(\boldsymbol{x})$ *and* poloidal field component $\boldsymbol{B}_P(\boldsymbol{x})$ *take the form*

$$\boldsymbol{B}_T \equiv \boldsymbol{\nabla} \times [\hat{\boldsymbol{n}} T(\boldsymbol{x})] \,, \tag{5.23}$$

$$\boldsymbol{B}_P \equiv \boldsymbol{\nabla} \times \boldsymbol{\nabla} \times [\hat{\boldsymbol{n}} P(\boldsymbol{x})] \,, \tag{5.24}$$

such that the toroidal *and* poloidal flux functions, $T(\boldsymbol{x})$ *and* $P(\boldsymbol{x})$ *respectively, are unique solutions to surface Poisson's equations on each foliating surface* $\mathcal{S}$*:*

$$\Delta_S P = -B_n \equiv -\hat{\boldsymbol{n}} \cdot \boldsymbol{B} \,, \tag{5.25}$$

$$\Delta_S T = -J_n \equiv -\hat{\boldsymbol{n}} \cdot \boldsymbol{\nabla} \times \boldsymbol{B} \,, \tag{5.26}$$

subject to either

$$P, T \to 0\,, \quad \textit{as} \quad |\boldsymbol{x}| \to \infty\,, \tag{5.27}$$

for non-compact $\mathcal{S} = \mathbb{E}^2$*, or*

$$\langle P \rangle_{\mathcal{S}} = \langle T \rangle_{\mathcal{S}} = 0\,, \tag{5.28}$$

for closed and compact surfaces $\mathcal{S} = S^2$ *or* $\mathbb{T}^2$*. Note that in the two latter cases, the following compatibility conditions also need to be satisfied on each foliating surface* $\mathcal{S}$*:*

$$\langle B_n \rangle_{\mathcal{S}} = \langle J_n \rangle_{\mathcal{S}} = 0\,. \tag{5.29}$$

Note that it is the case $\mathcal{S} = \mathbb{T}^2$ that generalises the original version in Berger and Hornig 2018, since it covers the multiply-connected case. Before presenting its proof in §5.2.3, we start by formally defining magnetic fields and magnetic vector potentials in the next subsection.

5.2.2. Magnetic Fields & Vector Potentials

Let $\boldsymbol{B} \in \ker[\mathrm{div}(V)]$ be a *magnetic field* in V, i.e.,

$$\boldsymbol{\nabla} \cdot \boldsymbol{B} = 0\,, \quad \text{in } V\,. \tag{5.30}$$

Since both Euclidean and spherical domains, V_{E} and V_{s} respectively, have trivial second de Rham cohomology group, i.e., $H^2(V_{\mathrm{E}}) = H^2(V_{\mathrm{s}}) = \{\boldsymbol{0}\}$, there exists some *(magnetic) vector potential* $\boldsymbol{A}$ in V_{E} or V_{s}, respectively, such that

$$\boldsymbol{B} = \boldsymbol{\nabla} \times \boldsymbol{A}\,. \tag{5.31}$$

In contrast, in the periodic domain V_{p}, since $H^2(V_{\mathrm{p}}) = \mathrm{span}\{\hat{\boldsymbol{e}}_w\}$ is non-trivial, we have

$$\boldsymbol{B} = \boldsymbol{\nabla} \times \boldsymbol{A} + \Phi(\boldsymbol{B})\,\hat{\boldsymbol{e}}_w\,, \tag{5.32}$$

where $\Phi(\boldsymbol{B})$ is the *net normal magnetic flux* defined by

$$\Phi(\boldsymbol{B}) \equiv \langle \hat{\boldsymbol{e}}_w, \boldsymbol{B} \rangle_{\mathcal{S}} \,. \tag{5.33}$$

However, since V_p (and also V_s) is foliated by closed surfaces, to avoid violating Gauß's law for magnetism (see e.g., Pfefferlé, Noakes, and Perrella 2021), we *impose* the condition of vanishing net normal flux, i.e.,

$$\Phi = 0 \,, \tag{5.34}$$

so that (5.31) also holds true in periodic domains V_p.

The choice of vector potential $\boldsymbol{A}$ is *non-unique*. Consider a gauge transformation

$$\boldsymbol{A} \mapsto \boldsymbol{A}' = \boldsymbol{A} + \boldsymbol{G} \tag{5.35}$$

for some gauge field $\boldsymbol{G} \in \ker[\mathrm{curl}(V)]$, i.e., $\boldsymbol{\nabla} \times \boldsymbol{G} = \boldsymbol{0}$, it ensures that

$$\boldsymbol{B} = \boldsymbol{\nabla} \times \boldsymbol{A}' = \boldsymbol{\nabla} \times \boldsymbol{A} \,. \tag{5.36}$$

Since $H^1(V_\mathrm{E}) = H^1(V_\mathrm{s}) = \{\boldsymbol{0}\}$, $\boldsymbol{G}$ must take the form

$$\boldsymbol{G} = \boldsymbol{\nabla}\chi \,, \quad \text{in } V = V_\mathrm{E} \text{ or } V_\mathrm{s} \,, \tag{5.37}$$

for some function χ, and

$$\boldsymbol{G} = \boldsymbol{\nabla}\chi + \boldsymbol{G}_0 \,, \quad \text{in } V = V_\mathrm{p} \,, \tag{5.38}$$

for some (doubly-periodic) function χ and some constant horizontal vector $\boldsymbol{G}_0$ (independent of w) such as

$$\boldsymbol{G}_0 \in H^1(V_\mathrm{p}) = \mathrm{span}\{\hat{\boldsymbol{e}}_x, \hat{\boldsymbol{e}}_y\} \,. \tag{5.39}$$

5.2.3. Proof of Theorem 5.3

Proof. Given a magnetic field $\boldsymbol{B}$ in $V = V_{\mathrm{E}}, V_{\mathrm{s}}$ or V_{p}, from §5.2.2, there always exists some admissible vector potential $\boldsymbol{A}$ such that $\boldsymbol{B} = \boldsymbol{\nabla} \times \boldsymbol{A}$. Applying the Hodge Decomposition Theorem for surfaces (Theorem 5.2) to $\boldsymbol{A}$ on each $\mathcal{S}_t \equiv \mathcal{S} \times \{t\}$ yields

$$\boldsymbol{A} = A_n \hat{\boldsymbol{n}} - \hat{\boldsymbol{n}} \times \boldsymbol{\nabla}_S P + \boldsymbol{\nabla}_S g + \boldsymbol{A}^* \,, \tag{5.40}$$

where $t = w$ and $\hat{\boldsymbol{n}} = \hat{\boldsymbol{e}}_w$ for $V = V_{\mathrm{E}}$ or V_{p}; and $t = r$ and $\hat{\boldsymbol{n}} = \hat{\boldsymbol{e}}_r$ for $V = V_{\mathrm{s}}$. The summands of (5.40) are mutually orthogonal with respect to the L^2-inner product (5.20) and are uniquely defined by:

$$A_n = \hat{\boldsymbol{n}} \cdot \boldsymbol{A} \,, \tag{5.41}$$

$$\Delta_S P = -\hat{\boldsymbol{n}} \cdot \boldsymbol{\nabla} \times \boldsymbol{A} \,, \tag{5.42}$$

$$\Delta_S g = \boldsymbol{\nabla}_S \cdot (\boldsymbol{A} - A_n \hat{\boldsymbol{n}}) \,, \tag{5.43}$$

$$\boldsymbol{A}^* = \boldsymbol{A} - A_n \hat{\boldsymbol{n}} + \hat{\boldsymbol{n}} \times \boldsymbol{\nabla}_S P - \boldsymbol{\nabla}_S g \,. \tag{5.44}$$

Also, from Theorem 5.2, it follows that the harmonic component $\boldsymbol{A}^*$ satisfies

$$\boldsymbol{A}^* = \begin{cases} \boldsymbol{0} \,, & \text{for } V = V_{\mathrm{E}} \text{ or } V_{\mathrm{s}} \,; \\ A^*_x(w)\, \hat{\boldsymbol{e}}_x + A^*_y(w)\, \hat{\boldsymbol{e}}_y \,, & \text{for } V = V_{\mathrm{p}} \,. \end{cases} \tag{5.45}$$

In both cases, we have

$$\hat{\boldsymbol{n}} \cdot \boldsymbol{A}^* = \boldsymbol{\nabla}_S \cdot \boldsymbol{A}^* = \hat{\boldsymbol{n}} \cdot \boldsymbol{\nabla} \times \boldsymbol{A}^* = 0 \,. \tag{5.46}$$

Now, consider a gauge transformation to $\boldsymbol{A}$ such that $\boldsymbol{A} \mapsto \boldsymbol{A}' = \boldsymbol{A} + \boldsymbol{G}$ for some $\boldsymbol{G} \in \ker[\mathrm{curl}(V)]$. Using Theorem 5.2, we can similarly decompose (5.37)-(5.38) as follows

$$\boldsymbol{G} = \begin{cases} \dfrac{\partial \chi}{\partial n} \hat{\boldsymbol{n}} + \boldsymbol{\nabla}_{\mathcal{S}} \chi \,, & \text{for } V = V_{\mathrm{E}} \text{ or } V_{\mathrm{s}} \,; \\ \dfrac{\partial \chi}{\partial n} \hat{\boldsymbol{n}} + \boldsymbol{\nabla}_{\mathcal{S}} \chi + \boldsymbol{G}_0 \,, & \text{for } V = V_{\mathrm{p}} \,; \end{cases} \tag{5.47}$$

where $\partial\chi/\partial n \equiv \hat{\boldsymbol{n}} \cdot \boldsymbol{\nabla}\chi$ and $\boldsymbol{G}_0$ is a constant horizontal vector independent of w. Then,

substituting (5.47) into (5.40), we have

$$\boldsymbol{A}' = \left(A_n + \frac{\partial \chi}{\partial n}\right)\hat{\boldsymbol{n}} - \hat{\boldsymbol{n}} \times \boldsymbol{\nabla}_S P + \boldsymbol{\nabla}_S(g + \chi) + \{\boldsymbol{A}^* + \boldsymbol{G}_0\}\,, \tag{5.48}$$

where the terms in curly braces are non-zero only when $V = V_{\mathrm{p}}$, and we used

$$-\hat{\boldsymbol{n}} \times \boldsymbol{\nabla}_S P = \boldsymbol{\nabla} \times (P\hat{\boldsymbol{n}})\,. \tag{5.49}$$

Note that (5.49) holds in our domains of interest, which is in general *not* valid; see Berger and Hornig 2018 and Yi and Choe 2022 for more discussions.

It follows from (5.48) that P is manifestly invariant under gauge transformations. Also, recall that, from Theorem 5.2 (in particular (5.42)), P automatically satisfies $\Delta_{\mathcal{S}} P = -\hat{\boldsymbol{n}} \cdot \boldsymbol{B}$, as required. As discussed in §3.2.3, for closed surfaces $\mathcal{S} = S^2$ or $\mathbb{T}^2$, we need to impose on each $\mathcal{S}$ the compatibility condition (3.54), i.e.,

$$\langle P \rangle_{\mathcal{S}} = 0\,. \tag{5.50}$$

Defining

$$T \equiv A_w + \frac{\partial \chi}{\partial n}\,, \tag{5.51}$$

and applying $\hat{\boldsymbol{n}} \cdot \boldsymbol{\nabla} \times \boldsymbol{\nabla} \times$ to (5.48), (5.26) can be explicitly verified, using $\boldsymbol{\nabla} \times \hat{\boldsymbol{n}} = \boldsymbol{0} = \boldsymbol{\nabla}_{\mathcal{S}} \times \hat{\boldsymbol{n}}$. Then, for closed surfaces, we can impose on each $\mathcal{S}_w$ that

$$\langle T \rangle_{\mathcal{S}} = 0\,. \tag{5.52}$$

Applying $\boldsymbol{\nabla} \times$ to (5.40) and, in the case of $V = V_{\mathrm{p}}$ identifying

$$\boldsymbol{B}_0 = \boldsymbol{\nabla} \times (\boldsymbol{A}^* + \boldsymbol{G}) = \boldsymbol{\nabla} \times \boldsymbol{A}^*\,, \tag{5.53}$$

concludes the proof. □

5.2.4. Elementary Properties

Expressions via Green's Functions

Using the Green's functions $G(\boldsymbol{x};\boldsymbol{x}')$ for the surface Laplacian $\Delta_{\mathcal{S}}$ when $\mathcal{S}=\mathbb{E}^2$ (cf. §2.2.2) and the generalised Green's functions when $\mathcal{S}=S^2$ or $\mathbb{T}^2$ (cf. §3.2.4 and 4.2.2), the Poisson's equations (5.25)-(5.26) for flux functions T and P can be explicitly solved as

$$P(\boldsymbol{x}) = -\int_{\mathcal{S}} B_n(\boldsymbol{x}')\; G(\boldsymbol{x};\boldsymbol{x}')\;\, \mathrm{d}^2\boldsymbol{x}'\;, \tag{5.54}$$

$$T(\boldsymbol{x}) = -\int_{\mathcal{S}} J_n(\boldsymbol{x}')\; G(\boldsymbol{x};\boldsymbol{x}')\;\, \mathrm{d}^2\boldsymbol{x}'\;, \tag{5.55}$$

subject to (5.28) if necessary. Here, we recall that the relevant (generalised, if appropriate) Green's functions are given by,

$$G_{\mathrm{E}}(\boldsymbol{x};\boldsymbol{x}') = \frac{1}{2\pi}\ln|\boldsymbol{x}-\boldsymbol{x}'|\,, \tag{5.56}$$

$$G_{\mathrm{s}}(\boldsymbol{x};\boldsymbol{x}') = \frac{1}{4\pi}\ln\left(1-\boldsymbol{x}\cdot\boldsymbol{x}'/r^2\right), \tag{5.57}$$

$$G_{\mathrm{p}}(\boldsymbol{x};\boldsymbol{x}') = \frac{1}{2\pi}\log|\vartheta_1(z-z')| - \frac{1}{2}[\mathrm{Im}(z-z')]^2\,. \tag{5.58}$$

Here, complex notation is used in the last case (cf. (4.32)).

Reciprocity

Magnetic fields of the forms (5.23) and (5.24) are respectively called *toroidal* and *poloidal magnetic fields* (see e.g., Moffatt and Dormy 2019). By definition, the field lines of $\boldsymbol{B}_T$ are confined on $\mathcal{S}$, since

$$\hat{\boldsymbol{n}}\cdot\boldsymbol{B}_T = 0\,. \tag{5.59}$$

By reciprocity (see also Berger and Hornig 2018), we mean that the curl of a toroidal field is a poloidal field, i.e.,

$$\boldsymbol{\nabla} \times \boldsymbol{B}_T = -\boldsymbol{\nabla} \times (\hat{\boldsymbol{n}} \times \boldsymbol{\nabla}_{\mathcal{S}} T) = \boldsymbol{B}_P \,, \quad \text{with } P \equiv \boldsymbol{\nabla}_{\mathcal{S}} T \,; \tag{5.60}$$

and the curl of a poloidal field is a toroidal field, i.e., by explicit computations,

$$\boldsymbol{\nabla} \times \boldsymbol{B}_P = -\Delta_{\mathcal{S}} \boldsymbol{\nabla} \times (\hat{\boldsymbol{n}} P) = -\boldsymbol{\nabla} \times (\hat{\boldsymbol{n}} \Delta_{\mathcal{S}} P) = \boldsymbol{B}_T \,, \quad \text{with } T \equiv \Delta_{\mathcal{S}} P \,. \tag{5.61}$$

It is worth noting that Yi and Choe 2022 proved that, among two-dimensional, simply-connected surfaces, the reciprocity property is *only* valid for foliations of $\mathbb{E}^2$ and S^2.

Orthogonality

In Euclidean and spherical domains, $V = V_{\mathrm{E}}$ and V_{s}, which are simply connected, Berger and Hornig 2018 proved that the poloidal and toroidal field components are orthogonal with respect to the L^2-inner product, i.e.,

$$\langle \boldsymbol{B}_T, \boldsymbol{B}_P \rangle_{\mathcal{S}} \equiv \int \boldsymbol{B}_T \cdot \boldsymbol{B}_P \, \mathrm{d}A = 0 \,. \tag{5.62}$$

To see this, note that

$$\begin{aligned}
\boldsymbol{B}_T \cdot \boldsymbol{B}_P &= \boldsymbol{\nabla} \times (\hat{\boldsymbol{n}} T) \cdot \boldsymbol{\nabla} \times \boldsymbol{\nabla} \times (\hat{\boldsymbol{n}} P) && (5.63)\\
&= \boldsymbol{\nabla}_{\mathcal{S}} \cdot \left[\hat{\boldsymbol{n}} T \times \boldsymbol{\nabla} \times \boldsymbol{\nabla} \times (\hat{\boldsymbol{n}} P) \right] - \hat{\boldsymbol{n}} T \cdot \boldsymbol{\nabla} \times \boldsymbol{\nabla} \times \boldsymbol{\nabla} \times (\hat{\boldsymbol{n}} P) && (5.64)\\
&= \boldsymbol{\nabla}_{\mathcal{S}} \cdot \left[\hat{\boldsymbol{n}} T \times \boldsymbol{\nabla} \times \boldsymbol{\nabla} \times (\hat{\boldsymbol{n}} P) \right] - \hat{\boldsymbol{n}} T \cdot \hat{\boldsymbol{n}} \times \boldsymbol{\nabla}_{\mathcal{S}} \Delta_{\mathcal{S}} P && (5.65)\\
&= \boldsymbol{\nabla}_{\mathcal{S}} \cdot \left[\hat{\boldsymbol{n}} T \times \boldsymbol{\nabla} \times \boldsymbol{\nabla} \times (\hat{\boldsymbol{n}} P) \right] , && (5.66)
\end{aligned}$$

where in (5.64) we used that $\boldsymbol{\nabla} = \boldsymbol{\nabla}_{\mathcal{S}}$, and in (5.65) we used reciprocity (5.61). For $\mathcal{S} = S^2$ or $\mathbb{T}^2$, (5.62) holds true since any integral over a closed compact surface is zero by Gauß's theorem. In the case of $\mathcal{S} = \mathbb{E}^2$, for (5.62) to be valid, we need to assume that magnetic fields decay sufficiently fast at infinity so that the boundary integral vanishes.

For the periodic domains V_{p}, in addition to (5.62), it is easy to see that,

$$\langle \boldsymbol{B}_T, \boldsymbol{B}_0 \rangle_{\mathcal{S}} = \langle \boldsymbol{B}_P, \boldsymbol{B}_0 \rangle_{\mathcal{S}} = 0\,. \tag{5.67}$$

Thus, all summands in (5.22) are mutually orthogonal in the L^2-sense, which implies that the total magnetic energy,

$$E(\boldsymbol{B}) \equiv \int_t \frac{1}{2} \langle \boldsymbol{B}, \boldsymbol{B} \rangle_{\mathcal{S}_t} \, \mathrm{d}t = \int_V \frac{|\boldsymbol{B}|^2}{2} \, \mathrm{d}V \ , \tag{5.68}$$

decomposes orthogonally in the sense that

$$E(\boldsymbol{B}) = \begin{cases} E(\boldsymbol{B}_P) + E(\boldsymbol{B}_T)\,, & \text{for } V = V_{\mathrm{E}} \text{ or } V_{\mathrm{s}}\,; \\ E(\boldsymbol{B}_P) + E(\boldsymbol{B}_T) + E(\boldsymbol{B}_0)\,, & \text{for } V = V_{\mathrm{p}}\,. \end{cases} \tag{5.69}$$

5.3. The Winding Gauge $\boldsymbol{A}^{\mathrm{W}}$

The winding gauge $\boldsymbol{A}^{\mathrm{W}}$ is central to the topological interpretation of open-field helicity as total, flux-weighted winding of $\boldsymbol{B}$-lines, which will be proved in Chapter 6. Here, we will define $\boldsymbol{A}^{\mathrm{W}}$ in §5.3.1 and discuss its properties in §5.3.2.

5.3.1. Definition

In the proof of Theorem 5.3, the general form of the vector potentials are identified as

$$\boldsymbol{A}' = \hat{\boldsymbol{n}} T - \hat{\boldsymbol{n}} \times \boldsymbol{\nabla}_S P + \boldsymbol{\nabla}_S (g + \chi) + \{\boldsymbol{A}^* + \boldsymbol{G}_0\}\,, \tag{5.70}$$

recalling that the terms in curly braces are non-zero only when $V = V_{\mathrm{p}}$ (same below). (5.70) characterises precisely the gauge redundancy from the generalised poloidal-toroidal decomposition of magnetic fields (5.22). Previously, ibid. ignored the possibility of gauge transformations and Moffatt and Dormy 2019 enforced the Coulomb gauge (5.75) without considering other choices.

From (5.70), we define the *winding gauge* $\boldsymbol{A}^{\mathrm{W}}$ as

$$\boldsymbol{A}^{\mathrm{W}} \equiv \hat{\boldsymbol{n}} T + \boldsymbol{\nabla} \times (\hat{\boldsymbol{n}} P) + \{\boldsymbol{A}_0^{\mathrm{W}}\}\,, \tag{5.71}$$

by choosing

$$\chi = -g\,, \tag{5.72}$$

and, further in V_{p}, choosing $\boldsymbol{G}_0$ such that $\boldsymbol{A}_0^{\mathrm{W}} \equiv \boldsymbol{A}^* + \boldsymbol{G}_0$ satisfies

$$\int_{V_{\mathrm{p}}} \boldsymbol{A}_0^{\mathrm{W}} \cdot \boldsymbol{\nabla} \times \boldsymbol{A}_0^{\mathrm{W}}\, \mathrm{d}V = 0\,. \tag{5.73}$$

Note that the choices (5.72), and also (5.73) if in V_{p}, can be understood as a gauge transformation from (5.70).

The name "winding gauge" was first coined in Prior and Yeates 2014, in which they proved that open-field helicity defined in this gauge acquires the winding-based interpretation in Euclidean tubular domains (with finite horizontal extents), reviewed in §6.2.1.

5.3.2. Properties

First, one can check that $\boldsymbol{A}^{W}$ satisfies the property of vanishing surface divergence:

$$\boldsymbol{\nabla}_{\mathcal{S}} \cdot \boldsymbol{A}^{\mathrm{W}} \equiv \boldsymbol{\nabla} \cdot \boldsymbol{A}^{\mathrm{W}} - \hat{\boldsymbol{n}} \cdot \frac{\partial \boldsymbol{A}^{\mathrm{W}}}{\partial n} = 0\,, \tag{5.74}$$

on each $\mathcal{S}$ where $\hat{\boldsymbol{n}} = \hat{\boldsymbol{e}}_w$ or $\hat{\boldsymbol{e}}_r$. This holds also for the original definition of $\boldsymbol{A}^{W}$ in ibid. and also Prior and Yeates 2021. Meanwhile, the first use of a similar gauge condition can be found in Hornig 2006, in which (5.74) was imposed on the domain boundary in defining the so-called "universal gauge".

In comparison, the usual Coulomb or Biot-Savart gauge $\boldsymbol{A}^{\mathrm{C}}$, used in the topological interpretation of closed-field helicity in §1.3.2, satisfies

$$\boldsymbol{\nabla} \cdot \boldsymbol{A}^{\mathrm{C}} = 0\,. \tag{5.75}$$

In the periodic domains $V = V_{\mathrm{P}}$, the global condition (5.73) ensures that the harmonic flux $\boldsymbol{A}_0^{\mathrm{W}}$ has no overall contribution to helicity. To see this, recall that helicity is defined as

$$H(\boldsymbol{B}) \equiv \int_V \boldsymbol{A} \cdot \boldsymbol{B} \, \mathrm{d}V \ , \tag{5.76}$$

and

$$\int_{V_{\mathrm{P}}} \boldsymbol{A}_0^{\mathrm{W}} \cdot \boldsymbol{B} \ \mathrm{d}V = \int_{V_{\mathrm{P}}} \boldsymbol{A}_0^{\mathrm{W}} \cdot \boldsymbol{B}_0 \ \mathrm{d}V + \int_0^1 \boldsymbol{A}_0^{\mathrm{W}} \cdot \left[\int_{\mathcal{S}_w} (\boldsymbol{B} - \boldsymbol{B}_0) \, \mathrm{d}^2\boldsymbol{x} \right] \mathrm{d}w \ . \tag{5.77}$$

By definition, the first term is zero combined with the fact that $\boldsymbol{B}_0 = \boldsymbol{\nabla} \times \boldsymbol{A}_0^{\mathrm{W}}$, cf. (5.53), and the second term also vanishes, since $\langle \boldsymbol{B} - \boldsymbol{B}_0 \rangle_{\mathcal{S}} = \boldsymbol{0}$. Hence, we obtain

$$\int_{V_{\mathrm{P}}} \boldsymbol{A}_0^{\mathrm{W}} \cdot \boldsymbol{B} \ \mathrm{d}V = 0 \, . \tag{5.78}$$

Further discussions on the global condition (5.73) continue in §6.4.1.

Chapter 6

Winding Magnetic Helicity

6.1. Overview & Statement of Main Results

The main result of this chapter, and indeed this thesis, is to establish the topological interpretation of open-field magnetic helicity as the total, flux-weighted winding of $\boldsymbol{B}$-lines. By open-field magnetic helicity, we mean the *winding (magnetic) helicity* $H^{\mathrm{W}}(\boldsymbol{B})$ defined from the winding gauge $\boldsymbol{A}^{\mathrm{W}}$ (cf. Chapter 5), i.e.,

$$H^{\mathrm{W}}(\boldsymbol{B}) \equiv \int_V \boldsymbol{A}^{\mathrm{W}} \cdot \boldsymbol{B} \, \mathrm{d}V \ . \tag{6.1}$$

We consider foliated domains $V \equiv \mathcal{S}_t \times (0,1)$ from the following three types of surfaces whose information is summarised again in Table 6.1.

Domain V	Foliating Surface $\mathcal{S}$	Surface Normal $\hat{\boldsymbol{n}}$	Foliating (Level) Parameter t	Proof of Theorem 6.1
Euclidean Domains V_{E}	$\mathbb{E}^2$	$\hat{\boldsymbol{e}}_w$	w (vertical)	§6.2
Spherical Doamins V_{s}	S^2	$\hat{\boldsymbol{e}}_r$	r (radial)	§6.3
Periodic Domains V_{p}	$\mathbb{T}^2$	$\hat{\boldsymbol{e}}_w$	w (vertical)	§6.4

Table 6.1: Foliated domains $V = \mathcal{S}_t \times (0,1)$ considered in Chapters 5 and 6 and the associated foliating surfaces $\mathcal{S}$.

Recall that $\boldsymbol{B}$-lines are defined as the field lines or the integral curves of $\boldsymbol{B}$, i.e.,

$$\frac{\mathrm{d}\boldsymbol{x}}{\mathrm{d}t} = \frac{\boldsymbol{B}[\boldsymbol{x}(t)]}{B_n[\boldsymbol{x}(t)]}\,, \qquad \text{where } B_n \equiv \hat{\boldsymbol{n}}\cdot\boldsymbol{B}\,, \tag{6.2}$$

with suitable initial conditions. Thus, we can state the equivalence theorem as follows:

Theorem 6.1 (Winding Magnetic Helicity; Prior and Yeates 2014; Xiao, Prior, and Yeates 2023a, 2024). *Winding helicity $H^{\mathrm{W}}(\boldsymbol{B})$ in foliated domains $V = V_{\mathrm{E}}, V_{\mathrm{s}}$, and V_{p} is equivalent to the total, flux-weighted pairwise winding of $\boldsymbol{B}$-lines, i.e.,*

$$H^{\mathrm{W}}(\boldsymbol{B}) = \frac{1}{2\pi}\int_0^1 \int_{\mathcal{S}_t}\int_{\mathcal{S}_t} \omega\big[t;\gamma(\boldsymbol{x}),\gamma'(\boldsymbol{x}')\big]\,B_n(\boldsymbol{x})B_n(\boldsymbol{x}')\,\mathrm{d}^2\boldsymbol{x}'\,\mathrm{d}^2\boldsymbol{x}\,\mathrm{d}t\,. \tag{6.3}$$

Here, $\mathcal{S}_t$ is the foliating surface at level t, ω is the domain-specific pairwise winding rate defined in Chapters 2 - 4, and γ,γ' are the respective $\boldsymbol{B}$-lines through $\boldsymbol{x}$ and $\boldsymbol{x}'$ at level t. The double surface integral is taken over all possible pairs of field lines rooted at the base surface $\mathcal{S}_0$.

By interpreting the winding helicity $H^{\mathrm{W}}(\boldsymbol{B})$ as an intrinsic, topological quantity defined from the field itself, Theorem 6.1 provides a meaningful and unambiguous definition for open-field helicity, resolving the issue of gauge dependence. The proofs of Theorem 6.1 will be given in §6.2 for Euclidean domains V_{E}, in §6.3 for spherical domains V_{s}, and in §6.4 for periodic domains V_{p}. Two toy examples are included in §6.5 to illustrate the novel properties of spherical and periodic winding helicity.

We remark that that while the proofs of Theorem 6.1 presented in this chapter will only cover the case when $\boldsymbol{B}$-lines are t-monotonic, the general case is in fact implicitly implied but it is beyond the scope of this thesis.

6.2. Euclidean Case

In Euclidean domains V_{E}, the first direct proof of Theorem 6.1 was given in Prior and Yeates 2014, and it is reviewed in §6.2.1. Then, in §6.2.2, a new proof is presented following Xiao, Prior, and Yeates 2023a, which establishes the foundation of the proof for spherical domains in §6.3.

6.2.1. Proof by Prior and Yeates 2014

In ibid., the authors considered a Euclidean tubular domain V_{E} of the form

$$V_{\mathrm{E}} = S_w \times (0,1)\,, \tag{6.4}$$

where surfaces $S_w \subset \mathbb{E}^2 \times \{w\}$ (with vertical coordinate w) are simply-connected and their boundary ∂S_w varies continuously with w. The boundary of V is $\partial V = S_0 \cup S_1 \cup S_s$, where

$$S_s = \{\partial S_w : w \in (0,1)\}\,, \quad \text{on which } B_n = 0\,. \tag{6.5}$$

Note that this choice of domain has finite horizontal extent and is therefore more general than that considered in §6.2.2.

The authors proposed, for the first time, the winding gauge $\boldsymbol{A}^{\mathrm{W}}$ in the Euclidean domain, defined by,

$$\boldsymbol{A}^{\mathrm{W}}(\boldsymbol{x}) \equiv \frac{1}{2\pi} \int_{S_w} \boldsymbol{B}(\boldsymbol{x}') \times \frac{\boldsymbol{x} - \boldsymbol{x}'}{|\boldsymbol{x} - \boldsymbol{x}'|^2}\, \mathrm{d}^2\boldsymbol{x}'\,. \tag{6.6}$$

Note that (6.6) satisfies the property of vanishing horizontal divergence, cf. §5.3.2,

$$\boldsymbol{\nabla}_{\mathcal{S}} \cdot \boldsymbol{A}^{\mathrm{W}} = 0\,. \tag{6.7}$$

Via computation, they verified that $\boldsymbol{A}^{\mathrm{W}}$ is indeed an admissible vector potential, i.e.,

$$\boldsymbol{\nabla} \times \boldsymbol{A}^{\mathrm{W}} = \boldsymbol{B}\,. \tag{6.8}$$

A crucial step in the proof was to apply the boundary condition (6.5).

Then, it follows that, by writing the surface magnetic field as $\boldsymbol{B}_{\mathcal{S}} = (B_x, B_y, 0)$ and

position vectors at level w as $\boldsymbol{x} = (x, y, w)$ and $\boldsymbol{x}' = (x', y', w)$, we have

$$\boldsymbol{A}^{\mathrm{W}}(\boldsymbol{x}) \cdot \boldsymbol{B}(\boldsymbol{x}) = \left(\frac{1}{2\pi} \int_{S_w} \boldsymbol{B}(\boldsymbol{x}') \times \frac{\boldsymbol{x} - \boldsymbol{x}'}{|\boldsymbol{x} - \boldsymbol{x}'|^2} \, \mathrm{d}^2\boldsymbol{x}' \right) \cdot \boldsymbol{B}(\boldsymbol{x}) \tag{6.9}$$

$$= \frac{1}{2\pi} \int_{S_w} [B_w(\boldsymbol{x}')\boldsymbol{B}_{\mathcal{S}}(\boldsymbol{x}) - B_w(\boldsymbol{x})\boldsymbol{B}_{\mathcal{S}}(\boldsymbol{x}')] \cdot \hat{\boldsymbol{e}}_w \times \frac{\boldsymbol{x} - \boldsymbol{x}'}{|\boldsymbol{x} - \boldsymbol{x}'|^2} \, \mathrm{d}^2\boldsymbol{x}' \tag{6.10}$$

$$= \frac{1}{2\pi} \int_{S_w} \left[\frac{\boldsymbol{B}_{\mathcal{S}}(\boldsymbol{x})}{B_w(\boldsymbol{x})} - \frac{\boldsymbol{B}_{\mathcal{S}}(\boldsymbol{x}')}{B_w(\boldsymbol{x}')} \right] \cdot \frac{(y' - y, x - x', 0)^T}{|\boldsymbol{x} - \boldsymbol{x}'|^2} B_w(\boldsymbol{x}) B_w(\boldsymbol{x}') \, \mathrm{d}^2\boldsymbol{x}' \, . \tag{6.11}$$

Substituting the defining equation of $\boldsymbol{B}$-lines (6.2) into (6.11) gives

$$\boldsymbol{A}^{\mathrm{W}} \cdot \boldsymbol{B} = \frac{1}{2\pi} \int_{S_w} \frac{\mathrm{d}}{\mathrm{d}w} (x - x', y - y', 0)^T \cdot \frac{(y' - y, x - x', 0)^T}{|\boldsymbol{x} - \boldsymbol{x}'|^2} \, B_w(\boldsymbol{x}) B_w(\boldsymbol{x}') \, \mathrm{d}^2\boldsymbol{x}' \, . \tag{6.12}$$

Recall that the Cartesian representation of the Euclidean winding rate ω_{E} is given by, as reviewed in (2.5) in Chapter 2,

$$\omega_{\mathrm{E}}(w; \boldsymbol{x}, \boldsymbol{x}') \equiv \frac{\mathrm{d}}{\mathrm{d}w} \arctan\left(\frac{y - y'}{x - x'} \right) = \frac{1}{|\boldsymbol{x} - \boldsymbol{x}'|^2} \left[(x - x') \frac{\mathrm{d}(y - y')}{\mathrm{d}w} - (y - y') \frac{\mathrm{d}(x - x')}{\mathrm{d}w} \right] , \tag{6.13}$$

so that by comparing (6.12) with (6.13) we obtain

$$\boldsymbol{A}^{\mathrm{W}} \cdot \boldsymbol{B} = \frac{1}{2\pi} \int_{S_w} \omega_{\mathrm{E}}(w; \boldsymbol{x}, \boldsymbol{x}') B_w(\boldsymbol{x}) B_w(\boldsymbol{x}') \, \mathrm{d}^2\boldsymbol{x}' \, . \tag{6.14}$$

Thus, Theorem 6.1 is proved by integrating (6.14) over $V_{\mathrm{E}} = S_w \times (0, 1)$.

6.2.2. Proof by Xiao, Prior, and Yeates 2023a

STEP I. First, we prove that winding helicity $H^{\mathrm{W}}(\boldsymbol{B})$ may be written as

$$H^{W}(\boldsymbol{B}) \equiv \int_{V_{\mathrm{E}}} \boldsymbol{A}^{\mathrm{W}} \cdot \boldsymbol{B} \, \mathrm{d}V = \int_0^1 \int_{S_w} \int_{S_w} \mathcal{H}(\boldsymbol{B}; \boldsymbol{x}, \boldsymbol{x}') \, \mathrm{d}^2\boldsymbol{x}' \, \mathrm{d}^2\boldsymbol{x} \, \mathrm{d}w \, , \tag{6.15}$$

in the Euclidean domain $V_{\mathrm{E}} = \mathcal{S}_w \times (0, 1)$, with the *(Euclidean) winding helicity density* $\mathcal{H}(\boldsymbol{B}; \boldsymbol{x}, \boldsymbol{x}')$ given by

$$\mathcal{H}(\boldsymbol{B}; \boldsymbol{x}, \boldsymbol{x}') \equiv \boldsymbol{B}(\boldsymbol{x}') \cdot \boldsymbol{B}_{\mathcal{S}}(\boldsymbol{x}) \times \boldsymbol{\nabla}_{\mathcal{S}} G_{\mathrm{E}}(\boldsymbol{x}, \boldsymbol{x}') + \boldsymbol{B}(\boldsymbol{x}) \cdot \boldsymbol{B}_{\mathcal{S}}(\boldsymbol{x}') \times \boldsymbol{\nabla}'_{\mathcal{S}} G_{\mathrm{E}}(\boldsymbol{x}, \boldsymbol{x}') \, , \tag{6.16}$$

in terms of the Euclidean Green's function $G_{\mathrm{E}}(\boldsymbol{x},\boldsymbol{x}')$ for Laplacian, cf. (5.56),

$$G_{\mathrm{E}}(\boldsymbol{x},\boldsymbol{x}') = \frac{1}{2\pi}\log|\boldsymbol{x}-\boldsymbol{x}'| = \frac{1}{2\pi}\log\xi = \frac{1}{2\pi}\log\xi' \,. \tag{6.17}$$

To show this, recall that the winding gauge $\boldsymbol{A}^{\mathrm{W}}$ for this domain choice is given by the generalised poloidal-toroidal decomposition, (5.71),as

$$\boldsymbol{A}^{\mathrm{W}} = \hat{\boldsymbol{e}}_w T + \boldsymbol{\nabla}\times(\hat{\boldsymbol{e}}_w P)\,, \tag{6.18}$$

and the flux functions P and T have explicit expressions (5.54) and (5.55), copied below as

$$P(\boldsymbol{x}) = -\int_{\mathcal{S}_w} B_w(\boldsymbol{x}')\; G_{\mathrm{E}}(\boldsymbol{x};\boldsymbol{x}')\;\mathrm{d}^2\boldsymbol{x}'\;, \tag{6.19}$$

$$T(\boldsymbol{x}) = -\int_{\mathcal{S}_w} J_w(\boldsymbol{x}')\; G_{\mathrm{E}}(\boldsymbol{x};\boldsymbol{x}')\;\mathrm{d}^2\boldsymbol{x}'\;. \tag{6.20}$$

Then, substituting (6.17), (6.19), and (6.20) into (6.18) gives

$$\boldsymbol{A}^{\mathrm{W}}(\boldsymbol{x}) = \frac{-1}{2\pi}\int_{\mathcal{S}_w}\left[B_w(\boldsymbol{x}')\left(-\hat{\boldsymbol{e}}_x\frac{\partial\ln\xi}{\partial y}+\hat{\boldsymbol{e}}_y\frac{\partial\ln\xi}{\partial x}\right)+\hat{\boldsymbol{e}}_w\left(\frac{\partial B_y(\boldsymbol{x}')}{\partial x'}-\frac{\partial B_x(\boldsymbol{x}')}{\partial y'}\right)\ln\xi\right]\mathrm{d}^2\boldsymbol{x}'\;, \tag{6.21}$$

where Cartesian coordinates $\boldsymbol{x}=(x,y,w)$ and $\boldsymbol{x}'=(x',y',w)$ at level w are explicitly used.

Using integration by parts, we claim that

$$\int_{\mathcal{S}_w}\left(\frac{\partial B_y(\boldsymbol{x}')}{\partial x'}-\frac{\partial B_x(\boldsymbol{x}')}{\partial y'}\right)\ln\xi\,\mathrm{d}^2\boldsymbol{x}' = \int_{\mathcal{S}_w}\left(B_y(\boldsymbol{x}')\frac{\partial\ln\xi}{\partial x'}-B_x(\boldsymbol{x}')\frac{\partial\ln\xi}{\partial y'}\right)\mathrm{d}^2\boldsymbol{x}'\;. \tag{6.22}$$

To justify (6.22), note that, for any scalar function $f(\boldsymbol{x})$, the following integrals over the open disk $\mathcal{D}(\boldsymbol{x},\epsilon)$ converge to zero, as $\epsilon\to 0$:

$$0 \le \left|\int_{\mathcal{D}(\boldsymbol{x},\epsilon)} f(\boldsymbol{x}')\ln|\boldsymbol{x}-\boldsymbol{x}'|\,\mathrm{d}^2\boldsymbol{x}'\right| \le \sup_{\mathcal{D}(\boldsymbol{x},\epsilon)}|f|\left|\int_0^\epsilon \ln\xi\cdot 2\pi\xi\,\mathrm{d}\xi\right| \to 0\,, \tag{6.23}$$

$$0 \le \left|\int_{\mathcal{D}(\boldsymbol{x},\epsilon)} \frac{f(\boldsymbol{x}')}{|\boldsymbol{x}-\boldsymbol{x}'|}\,\mathrm{d}^2\boldsymbol{x}'\right| \le \sup_{\mathcal{D}(\boldsymbol{x},\epsilon)}|f|\left|\int_0^\epsilon \frac{1}{\xi}\cdot 2\pi\xi\,\mathrm{d}\xi\right| \to 0\,, \tag{6.24}$$

where $\sup_{\mathcal{D}(\boldsymbol{x},\epsilon)}|f|$ is bounded, so the singularity $\boldsymbol{x}=\boldsymbol{x}'$ does not contribute in the inte-

gration. Applying Stokes' theorem in two dimensions to $\mathcal{S}_w \setminus \mathcal{D}(\boldsymbol{x}, \epsilon)$ and assuming that $\boldsymbol{B}$ decays sufficiently fast at infinity, the remaining boundary integral evaluates to zero:

$$\hat{\boldsymbol{e}}_w \cdot \int_{\mathcal{S}_w \setminus \mathcal{D}(\boldsymbol{x},\epsilon)} \boldsymbol{\nabla}' \times [\boldsymbol{B}(\boldsymbol{x}') \ln \xi] \, \mathrm{d}^2\boldsymbol{x}' = \hat{\boldsymbol{e}}_w \cdot \oint_{C(\boldsymbol{x},\epsilon)} \hat{\boldsymbol{n}}_2 \times \boldsymbol{B}(\boldsymbol{x}') \ln \xi \, \mathrm{d}\boldsymbol{x}' \xrightarrow{\epsilon \to 0} 0 \,, \tag{6.25}$$

since $\oint_{C(\boldsymbol{x},\epsilon)} \hat{\boldsymbol{n}}_2 \, \mathrm{d}l' \to \boldsymbol{0}$ as $\epsilon \to 0$. Here, $\boldsymbol{\nabla}'$ differentiates with respect to $\boldsymbol{x}'$ and $C(\boldsymbol{x}, \epsilon)$ is an infinitesimal loop around the singularity $\boldsymbol{x}$ with the outwards normal $\hat{\boldsymbol{n}}_2$. We have thus proved (6.22).

Next, by expanding $\boldsymbol{\nabla}' \times (\boldsymbol{B}(\boldsymbol{x}') \ln \xi)$ and taking inner products with $\boldsymbol{B}(\boldsymbol{x})$, we get

$$\boldsymbol{A}^{\mathrm{W}}(\boldsymbol{x}) \cdot \boldsymbol{B}(\boldsymbol{x}) = \int_{\mathcal{S}_w} \left[\boldsymbol{B}(\boldsymbol{x}') \cdot \boldsymbol{B}_{\mathcal{S}}(\boldsymbol{x}) \times \boldsymbol{\nabla}_{\mathcal{S}} G_{\mathrm{E}}(\boldsymbol{x}, \boldsymbol{x}') + \boldsymbol{B}(\boldsymbol{x}) \cdot \boldsymbol{B}_{\mathcal{S}}(\boldsymbol{x}') \times \boldsymbol{\nabla}'_{\mathcal{S}} G_{\mathrm{E}}(\boldsymbol{x}, \boldsymbol{x}') \right] \mathrm{d}^2\boldsymbol{x}' \,. \tag{6.26}$$

Integrating over $V_{\mathrm{E}} = \mathcal{S}_w \times (0, 1)$ leads to (6.15) and thus concludes STEP I.

STEP II. Recall that in §2.2.1, for any distinct points $\boldsymbol{x}, \boldsymbol{x}' \in \mathcal{S}_w$, we defined the following right-handed, orthonormal Euclidean winding basis, with $\hat{\boldsymbol{e}}_w = \hat{\boldsymbol{e}}'_w$,

$$\hat{\boldsymbol{e}}_\xi \equiv \frac{\boldsymbol{x}' - \boldsymbol{x}}{|\boldsymbol{x}' - \boldsymbol{x}|}, \quad \hat{\boldsymbol{e}}_\chi \equiv \hat{\boldsymbol{e}}_w \times \hat{\boldsymbol{e}}_\xi \,; \quad \hat{\boldsymbol{e}}'_\xi \equiv \frac{\boldsymbol{x} - \boldsymbol{x}'}{|\boldsymbol{x} - \boldsymbol{x}'|}, \quad \hat{\boldsymbol{e}}'_\chi \equiv \hat{\boldsymbol{e}}'_w \times \hat{\boldsymbol{e}}'_\xi \,. \tag{6.27}$$

In this basis, we have rewritten the Green's function as (6.17) which has surface gradients:

$$\boldsymbol{\nabla}_{\mathcal{S}} G_{\mathrm{E}}(\boldsymbol{x}, \boldsymbol{x}') = \frac{\hat{\boldsymbol{e}}_\xi}{2\pi\xi} \,, \qquad \boldsymbol{\nabla}'_{\mathcal{S}} G_{\mathrm{E}}(\boldsymbol{x}, \boldsymbol{x}') = \frac{\hat{\boldsymbol{e}}'_\xi}{2\pi\xi'} \,. \tag{6.28}$$

Then, the first term in $\mathcal{H}(\boldsymbol{B}; \boldsymbol{x}, \boldsymbol{x}')$, (6.16), becomes

$$\begin{aligned} \boldsymbol{B}(\boldsymbol{x}') \cdot \boldsymbol{B}_{\mathcal{S}}(\boldsymbol{x}) \times \boldsymbol{\nabla}_{\mathcal{S}} G_{\mathrm{E}}(\boldsymbol{x}, \boldsymbol{x}') &= \frac{1}{2\pi\xi} \boldsymbol{B}(\boldsymbol{x}') \cdot [B_\xi(\boldsymbol{x}) \hat{\boldsymbol{e}}_\xi + B_\chi(\boldsymbol{x}) \hat{\boldsymbol{e}}_\chi] \times \hat{\boldsymbol{e}}_\xi & (6.29) \\ &= \frac{1}{2\pi\xi} \boldsymbol{B}(\boldsymbol{x}') \cdot B_\chi(\boldsymbol{x})(-\hat{\boldsymbol{e}}_w) & (6.30) \\ &= -\frac{1}{2\pi\xi} B_w(\boldsymbol{x}') B_\chi(\boldsymbol{x}) \,, & (6.31) \end{aligned}$$

and similarly for $\boldsymbol{B}(\boldsymbol{x}) \cdot \boldsymbol{B}_{\mathcal{S}}(\boldsymbol{x}') \cdot \boldsymbol{\nabla}'_{\mathcal{S}} G_{\mathrm{E}}$. This leads to

$$\mathcal{H}(\boldsymbol{B}; \boldsymbol{x}, \boldsymbol{x}') = -\frac{1}{2\pi\xi}[B_w(\boldsymbol{x}')B_\chi(\boldsymbol{x}) + B_w(\boldsymbol{x})B_\chi(\boldsymbol{x}')]\,. \tag{6.32}$$

STEP III. We are now ready to prove Theorem 6.1. Let $\boldsymbol{x}, \boldsymbol{x}' : [0,1] \to V_{\mathrm{E}}$ be (w-monotonic) $\boldsymbol{B}$-lines of an open magnetic field $\boldsymbol{B}$, then the defining equation for $\boldsymbol{x}(w)$ in the $\boldsymbol{x}$-centred winding basis is given as (cf. §2.2.1)

$$\frac{\mathrm{d}\xi}{\mathrm{d}w}\hat{\boldsymbol{e}}_\xi + \xi\frac{\mathrm{d}\chi}{\mathrm{d}w}\hat{\boldsymbol{e}}_\chi + \hat{\boldsymbol{e}}_w = B_\xi\hat{\boldsymbol{e}}_\xi + B_\chi\hat{\boldsymbol{e}}_\chi + B_w\hat{\boldsymbol{e}}_w\,, \tag{6.33}$$

and similarly for $\boldsymbol{x}'(w)$, so that

$$\frac{\mathrm{d}\chi}{\mathrm{d}w} = \frac{1}{\xi}\frac{B_\chi(\boldsymbol{x})}{B_w(\boldsymbol{x})}, \qquad \frac{\mathrm{d}\chi'}{\mathrm{d}w} = \frac{1}{\xi'}\frac{B_\chi(\boldsymbol{x}')}{B_w(\boldsymbol{x}')}\,. \tag{6.34}$$

Recall that the Euclidean winding rate $\omega_{\mathrm{E}}(w; \boldsymbol{x}, \boldsymbol{x}')$, (2.29), is

$$\omega_{\mathrm{E}}(w; \boldsymbol{x}, \boldsymbol{x}') \equiv -\left(\frac{\mathrm{d}\chi}{\mathrm{d}w} + \frac{\mathrm{d}\chi'}{\mathrm{d}w}\right), \tag{6.35}$$

which can be written in terms of magnetic field components using (6.34) as

$$\omega_{\mathrm{E}}(w; \boldsymbol{x}, \boldsymbol{x}') = -\frac{1}{\xi}\left[\frac{B_\chi(\boldsymbol{x})}{B_w(\boldsymbol{x})} + \frac{B_\chi(\boldsymbol{x}')}{B_w(\boldsymbol{x}')}\right] \tag{6.36}$$

$$= -\frac{1}{\xi}\frac{B_w(\boldsymbol{x}')B_\chi(\boldsymbol{x}) + B_w(\boldsymbol{x})B_\chi(\boldsymbol{x}')}{B_w(\boldsymbol{x})B_w(\boldsymbol{x}')}\,. \tag{6.37}$$

Substituting (6.36) into the simplified integrand (6.32) and then the full integral (6.15) proves Theorem 6.1, i.e.,

$$H^W(\boldsymbol{B}) = \frac{1}{2\pi}\int_0^1 \int_{\mathcal{S}_w}\int_{\mathcal{S}_w} \omega_{\mathrm{E}}(w; \boldsymbol{x}, \boldsymbol{x}')B_w(\boldsymbol{x})B_w(\boldsymbol{x}')\ \mathrm{d}^2\boldsymbol{x}'\,\mathrm{d}^2\boldsymbol{x}\,\mathrm{d}w\ . \tag{6.38}$$

6.3. Spherical Case: Xiao, Prior, and Yeates 2023a

STEP I. Analogous to the second proof of Theorem 6.1 (in §6.2.2) in the Euclidean case, we start by showing that winding helicity $H^{\mathrm{W}}(\boldsymbol{B})$ has the following form

$$H^{\mathrm{W}}(\boldsymbol{B}) \equiv \int_{V_{\mathrm{s}}} \boldsymbol{A}^{\mathrm{W}} \cdot \boldsymbol{B} \, \mathrm{d}V = \int_0^1 \int_{\mathcal{S}_r} \int_{\mathcal{S}_r} \mathcal{H}(\boldsymbol{B}; \boldsymbol{x}, \boldsymbol{x}'), \mathrm{d}^2\boldsymbol{x}' \, \mathrm{d}^2\boldsymbol{x} \, \mathrm{d}r \,, \tag{6.39}$$

in the spherical domain $V_{\mathrm{s}} = \mathcal{S}_r \times (0,1)$, where the *(spherical) winding helicity density* $\mathcal{H}(\boldsymbol{B}; \boldsymbol{x}, \boldsymbol{x}')$ is given by

$$\mathcal{H}(\boldsymbol{B}; \boldsymbol{x}, \boldsymbol{x}') = \boldsymbol{B}(\boldsymbol{x}') \cdot \boldsymbol{B}_{\mathcal{S}}(\boldsymbol{x}) \times \boldsymbol{\nabla}_{\mathcal{S}} G_{\mathrm{s}}(\boldsymbol{x}, \boldsymbol{x}') + \boldsymbol{B}(\boldsymbol{x}) \cdot \boldsymbol{B}_{\mathcal{S}}(\boldsymbol{x}') \times \boldsymbol{\nabla}'_{\mathcal{S}} G_{\mathrm{s}}(\boldsymbol{x}, \boldsymbol{x}') \,, \tag{6.40}$$

in terms of the generalised Green's function $G_{\mathrm{s}}(\boldsymbol{x}, \boldsymbol{x}')$ for the spherical surface Laplacian (5.57), copied below as

$$G_{\mathrm{s}}(\boldsymbol{x}, \boldsymbol{x}') = \frac{1}{4\pi} \log\!\big(1 - \boldsymbol{x} \cdot \boldsymbol{x}'/r^2\big) = \frac{1}{4\pi} \log\!\big(1 - \cos\xi\big) = \frac{1}{4\pi} \log\!\big(1 - \cos\xi'\big) \,. \tag{6.41}$$

To prove (6.39), recall that the winding gauge $\boldsymbol{A}^{\mathrm{W}}$ for this domain choice is given by the generalised poloidal-toroidal decomposition in V_{s} as (5.71), or

$$\boldsymbol{A}^{\mathrm{W}} = \hat{\boldsymbol{e}}_r T + \boldsymbol{\nabla} \times (\hat{\boldsymbol{e}}_r P) \,, \tag{6.42}$$

and the flux functions P and T have explicit expressions (5.54) and (5.55), i.e.,

$$P(\boldsymbol{x}) = -\int_{\mathcal{S}_r} B_r(\boldsymbol{x}') \; G_{\mathrm{s}}(\boldsymbol{x}; \boldsymbol{x}') \;\; \mathrm{d}^2\boldsymbol{x}' \,, \tag{6.43}$$

$$T(\boldsymbol{x}) = -\int_{\mathcal{S}_r} J_r(\boldsymbol{x}') \; G_{\mathrm{s}}(\boldsymbol{x}; \boldsymbol{x}') \;\; \mathrm{d}^2\boldsymbol{x}' \,. \tag{6.44}$$

Then, substituting flux functions (6.41), (6.43), and (6.44) into (6.42) gives

$$\boldsymbol{A}^{\mathrm{W}}(\boldsymbol{x}) = \int_{\mathcal{S}_r} \left[\frac{B_r(\boldsymbol{x}')}{r} \left(\frac{\hat{\boldsymbol{e}}_\theta}{\sin\theta} \frac{\partial G_{\mathrm{s}}}{\partial \phi} - \hat{\boldsymbol{e}}_\phi \frac{\partial G_{\mathrm{s}}}{\partial \theta} \right) + \frac{\hat{\boldsymbol{e}}_r G_{\mathrm{s}}}{r \sin\theta'} \left(\frac{\partial}{\partial \theta'} (B_\phi(\boldsymbol{x}') \sin\theta') - \frac{\partial B_\theta(\boldsymbol{x}')}{\partial \phi'} \right) \right] \mathrm{d}^2\boldsymbol{x}' \,, \tag{6.45}$$

explicitly written in some reference spherical polar coordinates $\boldsymbol{x} = (r, \theta, \phi)$ and $\boldsymbol{x}' = (r, \theta', \phi')$ at radius r. Note that $\{\hat{\boldsymbol{e}}_r, \hat{\boldsymbol{e}}_\theta, \hat{\boldsymbol{e}}_\phi\}$ are the *orthonormal* basis vectors at $\boldsymbol{x}$ (as opposed to the orthogonal, coordinate basis vectors in §3.1.3).

Using integration by parts, we claim that the radial component of (6.45) is given by

$$\int_{\mathcal{S}_r} \frac{G_\mathrm{s}}{r' \sin\theta'} \left(\frac{\partial}{\partial \theta'} (B_\phi(\boldsymbol{x}') \sin\theta') - \frac{\partial B_\theta(\boldsymbol{x}')}{\partial \phi'} \right) \mathrm{d}^2\boldsymbol{x}' = \int_{\mathcal{S}_r} \left(- \frac{B_\phi(\boldsymbol{x}')}{r'} \frac{\partial G_\mathrm{s}}{\partial \theta'} + \frac{B_\theta(\boldsymbol{x}')}{r' \sin\theta'} \frac{\partial G_\mathrm{s}}{\partial \phi'} \right) \mathrm{d}^2\boldsymbol{x}' \,. \tag{6.46}$$

To justify this step, we need to isolate the singularity $\boldsymbol{x} = \boldsymbol{x}'$. For the term involving $\partial/\partial\theta'$, it suffices to consider the case $\phi' = \phi$ and

$$G_\mathrm{s}(\boldsymbol{x}, \boldsymbol{x}') = G_\mathrm{s}(\theta, \theta') = \frac{1}{4\pi} \ln\cos(\theta - \theta') \,. \tag{6.47}$$

We can divide the θ'-range into $S_1 \cup \mathcal{B}(\theta, \epsilon) \cup S_2$ where $S_1 = [0, \theta - \epsilon)$ and $S_2 = (\theta - \epsilon, \pi]$. There is no singularity in $S_1 \cup S_2$, so integration by parts can be used, i.e.,

$$\int_{S_1 \cup S_2} \frac{G_\mathrm{s}}{r' \sin\theta'} \frac{\partial}{\partial \theta'} \big[B_\phi(\boldsymbol{x}') \sin\theta' \big] \; r^2 \sin\theta' \, \mathrm{d}\theta' = \int_{S_1 \cup S_2} - \frac{B_\phi(\boldsymbol{x}')}{r'} \frac{\partial G_\mathrm{s}}{\partial \theta'} \; r^2 \sin\theta' \, \mathrm{d}\theta' \,, \tag{6.48}$$

where the boundary term vanishes due to the continuity of $B_\phi(\boldsymbol{x}')$ and the fact that $G_\mathrm{s}(\theta, \theta - \epsilon) = G_\mathrm{s}(\theta, \theta + \epsilon)$. When $\theta' \in \mathcal{B}(\theta, \epsilon)$, define $t \equiv \theta' - \theta$ with $|t| < \epsilon \ll 1$, we have $G_\mathrm{s}(\theta, \theta') = \ln\big(t^2/4\big) + O(t^2)$ and

$$\int_{\theta_-}^{\theta_+} \left(\frac{G_\mathrm{s}}{r \sin\theta'} \frac{\partial}{\partial \theta'} (B_\phi(\boldsymbol{x}') \sin\theta') \right) r^2 \sin\theta' \, \mathrm{d}\theta' = \int_{-\epsilon}^{\epsilon} G_\mathrm{s}(\theta, \theta') \frac{\partial}{\partial t} \big[B_\phi(\boldsymbol{x}') \sin\theta' \big] r \, \mathrm{d}t \to 0 \,, \tag{6.49}$$

where $\theta_\pm \equiv \theta \pm \epsilon$, since $\partial(B'_\phi \sin\theta')/\partial t$ is assumed smooth and $\int_{-\epsilon}^{\epsilon} \ln\big(t^2/4\big) \, \mathrm{d}t \to 0$ as $\epsilon \to 0$. The integral involving $\partial/\partial\phi'$ can be similarly evaluated.

Hence, the step (6.46) is valid which can be substituted in (6.45) to give

$$\boldsymbol{A}^\mathrm{W}(\boldsymbol{x}) = \int_{\mathcal{S}_r} \left[\frac{B_r(\boldsymbol{x}')}{r} \left(\frac{\hat{\boldsymbol{e}}_\theta}{\sin\theta} \frac{\partial G_\mathrm{s}}{\partial \phi} - \hat{\boldsymbol{e}}_\phi \frac{\partial G_\mathrm{s}}{\partial \theta} \right) + \hat{\boldsymbol{e}}_r \left(- \frac{B_\phi(\boldsymbol{x}')}{r'} \frac{\partial G_\mathrm{s}}{\partial \theta'} + \frac{B_\theta(\boldsymbol{x}')}{r' \sin\theta'} \frac{\partial G_\mathrm{s}}{\partial \phi'} \right) \right] \mathrm{d}^2\boldsymbol{x}' \,. \tag{6.50}$$

Taking inner product with $\boldsymbol{B}(\boldsymbol{x})$, we have

$$\begin{aligned}&\boldsymbol{A}^{\mathrm{W}}(\boldsymbol{x})\cdot\boldsymbol{B}(\boldsymbol{x})\\&=\int_{\mathcal{S}_r}\left(\frac{B_r(\boldsymbol{x}')}{r}\left[\frac{B_\theta(\boldsymbol{x})}{\sin\theta}\frac{\partial G_{\mathrm{s}}}{\partial\phi}-B_\phi(\boldsymbol{x})\frac{\partial G_{\mathrm{s}}}{\partial\theta}\right]+\frac{B_r(\boldsymbol{x})}{r}\left[\frac{B_\theta(\boldsymbol{x}')}{\sin\theta'}\frac{\partial G_{\mathrm{s}}}{\partial\phi'}-B_\phi(\boldsymbol{x}')\frac{\partial G_{\mathrm{s}}}{\partial\theta'}\right]\right)\mathrm{d}^2\boldsymbol{x}'\,.\end{aligned}\tag{6.51}$$

Finally, note that

$$\boldsymbol{\nabla}_{\mathcal{S}}=\frac{\hat{\boldsymbol{e}}_\theta}{r}\frac{\partial}{\partial\theta}+\frac{\hat{\boldsymbol{e}}_\phi}{r\sin\theta}\frac{\partial}{\partial\phi}\,,\qquad\boldsymbol{\nabla}'_{\mathcal{S}}=\frac{\hat{\boldsymbol{e}}'_\theta}{r}\frac{\partial}{\partial\theta'}+\frac{\hat{\boldsymbol{e}}'_\phi}{r\sin\theta'}\frac{\partial}{\partial\phi'}\,;\tag{6.52}$$

and by comparing with (6.51) we have

$$\boldsymbol{A}^{\mathrm{W}}(\boldsymbol{x})\cdot\boldsymbol{B}(\boldsymbol{x})=\int_{\mathcal{S}_r}\left[\boldsymbol{B}(\boldsymbol{x}')\cdot\boldsymbol{B}_{\mathcal{S}}(\boldsymbol{x})\times\boldsymbol{\nabla}_{\mathcal{S}}G_{\mathrm{s}}(\boldsymbol{x},\boldsymbol{x}')+\boldsymbol{B}(\boldsymbol{x})\cdot\boldsymbol{B}_{\mathcal{S}}(\boldsymbol{x}')\times\boldsymbol{\nabla}'_{\mathcal{S}}G_{\mathrm{s}}(\boldsymbol{x},\boldsymbol{x}')\right]\mathrm{d}^2\boldsymbol{x}'\,.\tag{6.53}$$

Integrating over $V_{\mathrm{s}}=\mathcal{S}_r\times(0,1)$ yields the desired result (6.39) and concludes STEP I.

STEP II. Recall that in §3.2.1, for any distinct and non-antipodal points $\boldsymbol{x},\boldsymbol{x}'\in\mathcal{S}_r$, we defined following the right-handed, orthonormal spherical winding basis,

$$\hat{\boldsymbol{\mathfrak{e}}}_\xi\equiv\frac{-\cos\xi\boldsymbol{x}+\boldsymbol{x}'}{r\sin\xi}\,,\quad\hat{\boldsymbol{\mathfrak{e}}}_\chi\equiv\frac{\hat{\boldsymbol{e}}_r\times\hat{\boldsymbol{\mathfrak{e}}}_\xi}{|\hat{\boldsymbol{e}}_r\times\hat{\boldsymbol{\mathfrak{e}}}_\xi|}\,;\quad\hat{\boldsymbol{\mathfrak{e}}}'_\xi\equiv\frac{-\cos\xi\boldsymbol{x}'+\boldsymbol{x}}{r\sin\xi}\,,\quad\hat{\boldsymbol{\mathfrak{e}}}'_\chi\equiv\frac{\hat{\boldsymbol{e}}'_r\times\hat{\boldsymbol{\mathfrak{e}}}'_\xi}{|\hat{\boldsymbol{e}}'_r\times\hat{\boldsymbol{\mathfrak{e}}}'_\xi|}\,.\tag{6.54}$$

In this basis, the generalised spherical Green's function $G_{\mathrm{s}}(\boldsymbol{x},\boldsymbol{x}')$ can be written as (6.41), and its surface gradients are given by, noting that $\xi=\xi'$,

$$\boldsymbol{\nabla}_{\mathcal{S}}G_{\mathrm{s}}(\boldsymbol{x},\boldsymbol{x}')=\frac{\sin\xi\;\hat{\boldsymbol{\mathfrak{e}}}_\xi}{4\pi r(1-\cos\xi)}\,,\qquad\boldsymbol{\nabla}'_{\mathcal{S}}G_{\mathrm{s}}(\boldsymbol{x},\boldsymbol{x}')=\frac{\sin\xi'\;\hat{\boldsymbol{\mathfrak{e}}}'_\xi}{4\pi r(1-\cos\xi)}\,.\tag{6.55}$$

Then, substituting (6.55) to the integrand $\mathcal{H}(\boldsymbol{B};\boldsymbol{x},\boldsymbol{x}')$, (6.40), we have

$$\mathcal{H}(\boldsymbol{B};\boldsymbol{x},\boldsymbol{x}')=-\frac{\sin\xi}{4\pi r(1-\cos\xi)}[B_r(\boldsymbol{x}')B_\chi(\boldsymbol{x})+B_r(\boldsymbol{x})B_\chi(\boldsymbol{x}')]\,.\tag{6.56}$$

Note that the spherical expression (6.56) is almost identical to its Euclidean counterpart (6.32), only differing by the coordinate-specific decomposition of magnetic fields (B_r

vs. B_w and different meanings of B_χ) and the pre-factor

$$\Gamma(\xi) \equiv \frac{\sin\xi}{1-\cos\xi} = \cot\left(\frac{\xi}{2}\right) = \frac{1}{R(\xi)}\,. \tag{6.57}$$

Here, recall that $R(\xi) = \tan(\xi/2)$ is the radial coordinate (3.22) of the stereographic projection σ as review in §3.1.4.

In fact, the spherical expression (6.56) reduces to the Euclidean counterpart (6.32) when curvature effects are small. To see this, consider the Laurent expansion of $\Gamma(\xi)$ at $\xi = 0$,

$$\frac{\sin\xi}{4\pi r(1-\cos\xi)} = \frac{1}{4\pi r}\left[\frac{2}{\xi} - \frac{\xi}{6} - \frac{\xi^3}{360} + O(\xi^5)\right]. \tag{6.58}$$

By recognising $r\xi = |\boldsymbol{x}-\boldsymbol{x}'|$ as the Euclidean distance between $\boldsymbol{x}$ and $\boldsymbol{x}'$, the leading term in (6.58) is precisely that of the pre-factor in (6.32), which is expected as the sphere is locally flat. Using (6.58), we can crudely estimate the percentage error between spherical and Euclidean results: approximately 2% for $\xi = 30°$, 10% for $\xi = 60°$ and 20% for $\xi = 90°$. A detailed case study follows in Chapter 7.

STEP III. In spherical winding coordinates, let $\boldsymbol{x}, \boldsymbol{x}' : (0,1) \to V_{\mathrm{s}}$ be r-monotonic $\boldsymbol{B}$-lines of an open magnetic field $\boldsymbol{B}$, then the defining equation for $\boldsymbol{x}(r)$ can be written in the local, $\boldsymbol{x}$-centred spherical winding basis as

$$r\frac{\mathrm{d}\xi}{\mathrm{d}r}\hat{\boldsymbol{e}}_\xi + r\sin\xi\frac{\mathrm{d}\chi}{\mathrm{d}r}\hat{\boldsymbol{e}}_\chi + \hat{\boldsymbol{e}}_r = B_\xi\hat{\boldsymbol{e}}_\xi + B_\chi\hat{\boldsymbol{e}}_\chi + B_r\hat{\boldsymbol{e}}_r\,, \tag{6.59}$$

and similarly for $\boldsymbol{x}'$. It then follows that,

$$\frac{\mathrm{d}\chi}{\mathrm{d}r} = \frac{1}{r\sin\xi}\frac{B_\chi(\boldsymbol{x})}{B_r(\boldsymbol{x})}, \qquad \frac{\mathrm{d}\chi'}{\mathrm{d}r} = \frac{1}{r\sin\xi'}\frac{B_\chi(\boldsymbol{x}')}{B_r(\boldsymbol{x}')}\,. \tag{6.60}$$

Recall that the spherical winding rate $\omega_{\mathrm{s}}(r;\boldsymbol{x},\boldsymbol{x}')$, (3.48), is given by

$$\omega_{\mathrm{s}}(r;\boldsymbol{x},\boldsymbol{x}') = -\frac{1}{2}(1+\cos\xi)\left(\frac{\mathrm{d}\chi}{\mathrm{d}r} + \frac{\mathrm{d}\chi'}{\mathrm{d}r}\right), \tag{6.61}$$

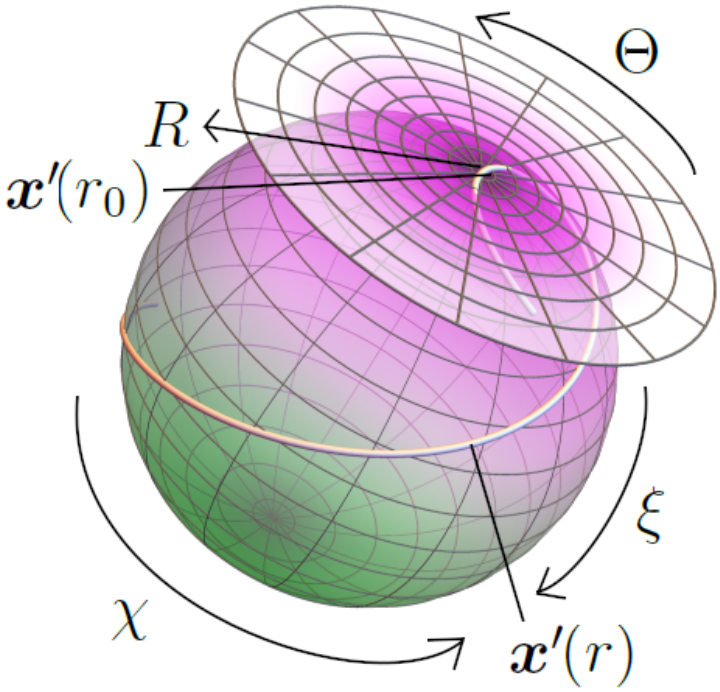

(a)

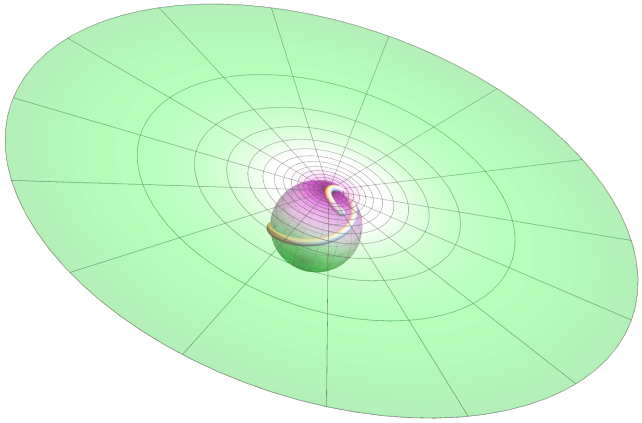

(b)

Figure 6.1: Visualisations of the dilating effect of the stereographic map σ projecting from the antipodal point of $\boldsymbol{x}'(r)$ with matched colouring on both domains. Panel (a) depicts the $\boldsymbol{x}'$-Northed winding coordinates (ξ, χ) on S^2 and the plane polar coordinates (R, Θ) on $\mathbb{E}^2$, showing part of the projected, Northern hemisphere. Panel (b) includes the projection for the Southern hemisphere where projected area elements are more diffused.

so that, by noting that $\xi = \xi'$, we have

$$\omega_{\mathrm{s}}(r;\boldsymbol{x},\boldsymbol{x}') = -\frac{1+\cos\xi}{2r\sin\xi}\left[\frac{B_\chi(\boldsymbol{x})}{B_r(\boldsymbol{x})}+\frac{B_\chi(\boldsymbol{x}')}{B_r(\boldsymbol{x}')}\right] \tag{6.62}$$

$$= -\frac{1+\cos\xi}{2r\sin\xi}\,\frac{B_r(\boldsymbol{x}')B_\chi(\boldsymbol{x})+B_r(\boldsymbol{x})B_\chi(\boldsymbol{x}')}{B_r(\boldsymbol{x})B_r(\boldsymbol{x}')}\,. \tag{6.63}$$

Comparing with the simplified integrand (6.56) and the full integral (6.39), we have thus proved Theorem 6.1 for spherical domains, i.e.,

$$H^{\mathrm{W}}(\boldsymbol{B}) = \frac{1}{2\pi}\int_0^1\int_{\mathcal{S}_r}\int_{\mathcal{S}_r}\omega_{\mathrm{s}}(r;\boldsymbol{x},\boldsymbol{x}')B_r(\boldsymbol{x})B_r(\boldsymbol{x}')\;\mathrm{d}^2\boldsymbol{x}'\,\mathrm{d}^2\boldsymbol{x}\,\mathrm{d}r\;. \tag{6.64}$$

6.4. Periodic Case: Xiao, Prior, and Yeates 2024

In this section, Theorem 6.1 is proved for the periodic domain $V_{\mathrm{p}} = \mathcal{S}_w \times (0,1)$, where $\mathcal{S}_w = \mathbb{T}^2 \times \{w\}$ or the doubly-periodic square at level w. A complex formulation will be used to exploit existing expressions of periodic winding rates ω_{p} in Chapter 5, as opposed to the vector approach for the Euclidean proof in §6.2.2 or the spherical proof in §6.3.

In §5.3.1, we defined the winding gauge $\boldsymbol{A}^{\mathrm{W}}$ in the periodic domain V_{p} as (5.71), i.e.,

$$\boldsymbol{A}^{\mathrm{W}} = \hat{\boldsymbol{e}}_w T + \boldsymbol{\nabla}\times(\hat{\boldsymbol{e}}_w P) + \boldsymbol{A}_0^{\mathrm{W}}\,, \tag{6.65}$$

such that its harmonic flux $\boldsymbol{A}_0^{\mathrm{W}}$ satisfies (5.73), or,

$$\int_{V_{\mathrm{p}}} \boldsymbol{A}_0^{\mathrm{W}}\cdot\boldsymbol{\nabla}\times\boldsymbol{A}_0^{\mathrm{W}}\;\mathrm{d}V = 0\,. \tag{6.66}$$

Consequently, it follows that $\boldsymbol{A}^{\mathrm{W}}$ has no contribution to the helicity integral, cf. (5.78),

$$\int_{V_{\mathrm{p}}} \boldsymbol{A}_0^{\mathrm{W}}\cdot\boldsymbol{B}\;\mathrm{d}V = 0\,, \tag{6.67}$$

and it now suffices to compute

$$H^{\mathrm{W}}(\boldsymbol{B}) \equiv \int_{V_{\mathrm{p}}} \boldsymbol{A}^{\mathrm{W}} \cdot \boldsymbol{B}\, \mathrm{d}V = \int_{V_{\mathrm{p}}} \tilde{\boldsymbol{A}}^{\mathrm{W}} \cdot \boldsymbol{B}\, \mathrm{d}V\,, \quad \text{where } \tilde{\boldsymbol{A}}^{\mathrm{W}} \equiv \boldsymbol{A}^{\mathrm{W}} - \boldsymbol{A}_0^{\mathrm{W}}\,. \tag{6.68}$$

Consider

$$\tilde{\boldsymbol{A}}^{\mathrm{W}} \cdot \boldsymbol{B} = B_x \partial_y P - B_y \partial_x P + B_w T = -2\,\mathrm{Im}(\mathcal{B}\partial_z P) + B_w T\,. \tag{6.69}$$

In the last equality, we defined $\mathcal{B} \equiv B_x + \mathrm{i}B_y$ as the complexified surface magnetic field. Recall that P and T are real-valued flux functions given by (5.54) and (5.55), i.e.,

$$P(z,w) = -\int_{\mathcal{S}_w} B_w(z')\, G_{\mathrm{p}}(z,z')\, \mathrm{d}A_{z'}\,, \tag{6.70}$$

$$T(z,w) = -\int_{\mathcal{S}_w} J_w(z')\, G_{\mathrm{p}}(z,z')\, \mathrm{d}A_{z'}\,; \tag{6.71}$$

where we used the complex variable $(z,w) = (x+\mathrm{i}y, w)$, the fact that $J_w = 2\,\mathrm{Im}(\partial_z \mathcal{B})$, and $\mathrm{d}A_z = \mathrm{d}\bar{z} \wedge \mathrm{d}z\,/(2\mathrm{i})$ is the area form on $\mathbb{C}$. The generalised Green's function $G_{\mathrm{p}}(z,z')$ for Laplacian (4.32) is introduced §4.2.2, given by

$$G_{\mathrm{p}}(z,z') = \frac{1}{2\pi} \log|\vartheta_1(z-z')| - \frac{1}{2}[\mathrm{Im}(z-z')]^2\,. \tag{6.72}$$

Substituting (6.70)-(6.71) into (6.69) then gives,

$$\tilde{\boldsymbol{A}}^{\mathrm{W}} \cdot \boldsymbol{B} = 2\,\mathrm{Im} \int_{\mathcal{S}_w} \mathcal{B}(z) B_w(z') \partial_z \big[G_{\mathrm{p}}(z,z')\big]\, \mathrm{d}A_{z'} - 2\int_{\mathcal{S}_w} B_w(z)\,\mathrm{Im}\left[\partial_{z'}\mathcal{B}(z')\right] G_{\mathrm{p}}(z,z')\, \mathrm{d}A_{z'} \tag{6.73}$$

$$= 2\,\mathrm{Im} \int_{\mathcal{S}_w} \Big(B_w(z')\mathcal{B}(z) \partial_z \big[G_{\mathrm{p}}(z,z')\big] + B_w(z)\mathcal{B}(z') \partial_{z'} \big[G_{\mathrm{p}}(z,z')\big] \Big)\, \mathrm{d}A_{z'}\,, \tag{6.74}$$

where we used integration by parts and the boundary integral vanishes due to periodicity.

Next, recall that the complexified equation for w-monotonic $\boldsymbol{B}$-lines is given by

$$\frac{\mathrm{d}z}{\mathrm{d}w} = \frac{\mathcal{B}[z(w)]}{B_w[z(w)]}\,, \tag{6.75}$$

assuming $B_w \neq 0$, which can be substituted into (6.74) to give

$$\tilde{\boldsymbol{A}}^{\mathrm{W}} \cdot \boldsymbol{B} = 2 \int_{\mathcal{S}_w} B_w(z') B_w(z) \operatorname{Im} \left(\frac{\mathrm{d}z}{\mathrm{d}w} \partial_z \left[G_{\mathrm{p}}(z, z') \right] + \frac{\mathrm{d}z'}{\mathrm{d}w} \partial_{z'} \left[G_{\mathrm{p}}(z, z') \right] \right) \mathrm{d}A_{z'} \tag{6.76}$$

$$= 2 \int_{\mathcal{S}_w} B_w(z) B_w(z') \operatorname{Im} \left[\frac{\mathrm{d}(z - z')}{\mathrm{d}w} \partial_z G_{\mathrm{p}}(z, z') \right] \mathrm{d}A_{z'} \ . \tag{6.77}$$

In the last equality, we used the fact that $\partial_{z'} G_{\mathrm{p}}(z, z') = -\partial_z G_{\mathrm{p}}(z, z')$.

From Chapter 5, the pairwise periodic winding rate ω_{p}, (4.37) for two w-parameterised curves γ, γ' respectively through z, z' (seen as projection on $\mathcal{S}$) is defined as

$$\omega_{\mathrm{p}}(w; \gamma, \gamma') = 4\pi \operatorname{Im} \left[\frac{\mathrm{d}(z - z')}{\mathrm{d}w} \partial_z G_{\mathrm{p}}(z, z') \right] . \tag{6.78}$$

Comparing with (6.77), we have

$$\tilde{\boldsymbol{A}}^{\mathrm{W}} \cdot \boldsymbol{B} = \frac{1}{2\pi} \int_{\mathcal{S}_w} \omega_{\mathrm{p}}(w; \gamma, \gamma') B_w(z) B_w(z') \ \mathrm{d}A_{z'} \ . \tag{6.79}$$

In the case when $B_w = 0$, the integrand of (6.79) vanishes, which can be used to *define* the excluded (and isolated) points. By integrating (6.77) over $V_{\mathrm{p}} = \mathcal{S}_w \times [0, 1]$, we have thus proved Theorem (6.1) in the periodic domains, i.e.,

$$H^{\mathrm{W}}(\boldsymbol{B}) = \frac{1}{2\pi} \int_0^1 \int_{\mathcal{S}_w} \int_{\mathcal{S}_w} \omega_{\mathrm{p}}[w; \gamma(z), \gamma'(z')] B_w(z) B_w(z') \ \mathrm{d}A_{z'} \, \mathrm{d}A_z \, \mathrm{d}w \ . \tag{6.80}$$

The complex formulation allows the periodic winding helicity to be computed more easily. Note that (6.3) would reduce to the Euclidean results (1.28) if ω_{p} was replaced with ω_{E}, noting that $\mathrm{d}A_z$ is the complex equivalent of $\mathrm{d}A$.

6.4.1. Properties of Periodic Winding Helicity

As outlined in Berger 1996, any meaningful definition of (open-field) helicity $H(\boldsymbol{B})$ in the periodic domain $V_{\mathrm{p}} = \mathbb{T}^2 \times [0, 1]$ should satisfy the following properties:

(P1) $H(\boldsymbol{B})$ must reduce to its non-periodic counterpart in suitable limits;

(P2) $H(\boldsymbol{B})$ is independent of translations and rotations of the representative of $\mathbb{T}^2$;

(P3) $H(\boldsymbol{B})$ is computable directly and unambiguously from $\boldsymbol{B}$;

(P4) $H(\boldsymbol{B})$ is conserved in ideal magnetohydrodynamic (MHD) flows with fixed endpoints of $\boldsymbol{B}$-lines on bounding surfaces;

(P5) $H(\boldsymbol{B})$ can be topologically interpreted as winding of $\boldsymbol{B}$-lines.

Periodic winding helicity $H^{\mathrm{W}}(\boldsymbol{B})$ clearly satisfies (P1)-(P3) and (P5), while (P4) will be proved shortly, thus providing an candidate for the open problem posed by Berger 1996. Meanwhile, we proceed to study how $H^{\mathrm{W}}(\boldsymbol{B})$ relates to helicity obtained in periodic domains from Fourier series (e.g., Berger 1996; Cattaneo, Bodo, and Tobias 2020; K. E. Yang, Wheatland, and Gilchrist 2020).

Time Conservation in Ideal MHD Flows

To show (P4), we need to include time evolution by introducing a flow velocity $\boldsymbol{u}$ (with the required periodicity; same below for other variables). In ideal MHD flows, $\boldsymbol{B}$ and $\boldsymbol{u}$ are related via the *induction equation* (e.g., see Moffatt and Dormy 2019) as

$$\frac{\partial \boldsymbol{B}}{\partial t} = \boldsymbol{\nabla} \times (\boldsymbol{u} \times \boldsymbol{B}) \,. \tag{6.81}$$

Assuming $\Phi \equiv \langle \hat{\boldsymbol{e}}_w, \boldsymbol{B} \rangle = 0$, there exists some vector potential $\boldsymbol{A}$ such that $\boldsymbol{B} = \boldsymbol{\nabla} \times \boldsymbol{A}$ and from (6.81) we obtain

$$\frac{\partial \boldsymbol{A}}{\partial t} = \boldsymbol{u} \times \boldsymbol{B} + \boldsymbol{\nabla} \chi + \left(\frac{\partial \boldsymbol{A}}{\partial t} \right)_0 , \tag{6.82}$$

accounting for possible gauge transformations (5.47). Here, the subscript 0 indicates the corresponding harmonic components. Thus,

Proposition 6.1 (P4). *Periodic winding helicity $H^{\mathrm{W}}(\boldsymbol{B})$ in V_{p} is conserved under ideal MHD evolution, given that on ∂V_{p} either (i) $\boldsymbol{B} \cdot \hat{\boldsymbol{e}}_w = \boldsymbol{u} \cdot \hat{\boldsymbol{e}}_w = 0$ or (ii) $\boldsymbol{B} \cdot \hat{\boldsymbol{e}}_w \neq 0$, $\boldsymbol{u} = \boldsymbol{0}$.*

Proof. Recall from (6.68) that for $\tilde{\boldsymbol{A}}^{\mathrm{W}} \equiv \boldsymbol{A}^{\mathrm{W}} - \boldsymbol{A}_0^{\mathrm{W}}$ we have $H^{\mathrm{W}}(\boldsymbol{B}) = \int_{V_{\mathrm{p}}} \tilde{\boldsymbol{A}}^{\mathrm{W}} \cdot \boldsymbol{B} \, \mathrm{d}V$. Since

V_{p} is fixed, it follows that

$$\frac{\mathrm{d}H^{\mathrm{W}}}{\mathrm{d}t} = \int_{V_{\mathrm{p}}} \frac{\partial}{\partial t}(\tilde{\boldsymbol{A}}^{\mathrm{W}} \cdot \boldsymbol{B})\, \mathrm{d}V \tag{6.83}$$

$$= \int_{V_{\mathrm{p}}} \left[\tilde{\boldsymbol{A}}^{\mathrm{W}} \cdot \boldsymbol{\nabla} \times (\boldsymbol{u} \times \boldsymbol{B}) + \boldsymbol{\nabla}\chi \cdot \boldsymbol{B}\right] \mathrm{d}V \tag{6.84}$$

$$= \int_{\partial V_{\mathrm{p}}} \left[\chi(\boldsymbol{B} \cdot \hat{\boldsymbol{e}}_w) + (\tilde{\boldsymbol{A}}^{\mathrm{W}} \cdot \boldsymbol{B})(\boldsymbol{u} \cdot \hat{\boldsymbol{e}}_w) - (\tilde{\boldsymbol{A}}^{\mathrm{W}} \cdot \boldsymbol{u})(\boldsymbol{B} \cdot \hat{\boldsymbol{e}}_w)\right] \mathrm{d}A\,. \tag{6.85}$$

Note that we substituted (6.81) and (6.82) in (6.84) and used $\boldsymbol{\nabla} \cdot \boldsymbol{B} = 0$, and for the last equality we applied Stokes' theorem. It is immediate that (i) implies $\mathrm{d}H^{\mathrm{W}}/\mathrm{d}t = 0$. For (ii), applying $\boldsymbol{\nabla}_S \cdot$ to (6.82) while using $\boldsymbol{\nabla}_S \cdot \boldsymbol{A}^{\mathrm{W}} = 0$ gives

$$\Delta_S \chi = 0 \implies \chi = \chi(w)\,. \tag{6.86}$$

Given that $\Phi \equiv \langle \hat{\boldsymbol{e}}_w, \boldsymbol{B} \rangle = 0$ for each $\mathcal{S}_w \equiv \mathbb{T}^2 \times \{w\}$, we have, on $\partial V = \mathcal{S}_0 \cup \mathcal{S}_1$,

$$\frac{\mathrm{d}H^{\mathrm{W}}}{\mathrm{d}t} = \chi(1)\, \langle \hat{\boldsymbol{e}}_w, \boldsymbol{B} \rangle_{\mathcal{S}_1} - \chi(0)\, \langle \hat{\boldsymbol{e}}_w, \boldsymbol{B} \rangle_{\mathcal{S}_0} = 0\,. \tag{6.87}$$

□

We remark that the above proof can be viewed as a simplified version of the conservation of relative helicity in multiply-connected domains by MacTaggart and Valli 2019, 2023 which satisfies (P1)-(P4). However, relative helicity is too general to have a topological interpretation. Interested readers are referred to Prior and Yeates 2014 for similar discussions on the non-periodic case.

Fourier Approach

Here, we demonstrate that helicity defined in periodic domains via Fourier series can be made equivalent to periodic winding helicity $H^{\mathrm{W}}(\boldsymbol{B})$ under suitable conditions.

Let $\boldsymbol{x}_S \equiv (x, y)$ and $\boldsymbol{k} \equiv (k_x, k_y) = 2\pi(n_x, n_y) \in 2\pi\mathbb{Z}^2$. Then, any periodic vector

potential $\boldsymbol{A}$ can be Fourier expanded as

$$\boldsymbol{A}(\boldsymbol{x}_S, w) = \hat{\boldsymbol{A}}_0(w) + \sum_{\boldsymbol{k}\neq\boldsymbol{0}} \hat{\boldsymbol{A}}_{\boldsymbol{k}}(w) \mathrm{e}^{\mathrm{i}\boldsymbol{k}\cdot\boldsymbol{x}_S}\,, \tag{6.88}$$

where the Fourier coefficients $\hat{\boldsymbol{A}}_{\boldsymbol{k}}$ (including $\boldsymbol{k}=\boldsymbol{0}$) are given by

$$\hat{\boldsymbol{A}}_{\boldsymbol{k}}(w) = \int_{\mathcal{S}_w} \boldsymbol{A}(\boldsymbol{x}_S, w) \mathrm{e}^{-\mathrm{i}\boldsymbol{k}\cdot\boldsymbol{x}_S}\, \mathrm{d}^2\boldsymbol{x}\,. \tag{6.89}$$

Here, the zero-mode $\hat{\boldsymbol{A}}_0$ is precisely the harmonic flux $\boldsymbol{A}_0$ in (5.21) (same below). Then, the smoothness of $\boldsymbol{B}$ allows term-by-term differentiation of (6.88), i.e., $\boldsymbol{B} = \boldsymbol{\nabla}\times\boldsymbol{A}$ and

$$\boldsymbol{B}(\boldsymbol{x}_S, w) = \boldsymbol{\nabla}\times\hat{\boldsymbol{A}}_0(w) + \sum_{\boldsymbol{k}\neq\boldsymbol{0}} \left(\mathrm{i}\boldsymbol{k}\times\hat{\boldsymbol{A}}_{\boldsymbol{k}} + \hat{\boldsymbol{e}}_w \times \frac{\partial \hat{\boldsymbol{A}}_{\boldsymbol{k}}}{\partial w}\right) \mathrm{e}^{\mathrm{i}\boldsymbol{k}\cdot\boldsymbol{x}_S} \tag{6.90}$$

$$\equiv \hat{\boldsymbol{B}}_0(w) + \sum_{\boldsymbol{k}\neq\boldsymbol{0}} \hat{\boldsymbol{B}}_{\boldsymbol{k}}(w)\ \mathrm{e}^{\mathrm{i}\boldsymbol{k}\cdot\boldsymbol{x}_S}\,, \tag{6.91}$$

where $\hat{\boldsymbol{B}}_0(w)$ (zero-mode) and $\hat{\boldsymbol{B}}_{\boldsymbol{k}}(w)$ are the Fourier coefficients of $\boldsymbol{B}$.

For each $\boldsymbol{k}\neq\boldsymbol{0}$, define a right-handed orthonormal wavevector basis $\{\hat{\boldsymbol{e}}_w, \hat{\boldsymbol{e}}_{\boldsymbol{k}\parallel}, \hat{\boldsymbol{e}}_{\boldsymbol{k}\perp}\}$ as

$$\hat{\boldsymbol{e}}_{\boldsymbol{k}\parallel} \equiv \boldsymbol{k}/k = \hat{\boldsymbol{k}} \qquad \hat{\boldsymbol{e}}_{\boldsymbol{k}\perp} \equiv \hat{\boldsymbol{e}}_w \times \hat{\boldsymbol{e}}_{\boldsymbol{k}\parallel}\,, \qquad \text{and} \quad k \equiv |\boldsymbol{k}|\,, \tag{6.92}$$

so that in this basis the Fourier coefficients of $\boldsymbol{A}$ and $\boldsymbol{B}$ are related via

$$\hat{B}_{\boldsymbol{k},w} = \mathrm{i}k\hat{A}_{\boldsymbol{k}\perp}\,, \tag{6.93}$$

$$\hat{B}_{\boldsymbol{k}\perp} = -\mathrm{i}k\hat{A}_{\boldsymbol{k},w} + \frac{\partial \hat{A}_{\boldsymbol{k}\parallel}}{\partial w}\,. \tag{6.94}$$

Note that

$$\hat{\boldsymbol{e}}_w\cdot\boldsymbol{\nabla}\times\boldsymbol{B} = \sum_{\boldsymbol{k}\neq\boldsymbol{0}} \mathrm{i}k\hat{B}_{\boldsymbol{k}\perp}\mathrm{e}^{\mathrm{i}\boldsymbol{k}\cdot\boldsymbol{x}_S} = \sum_{\boldsymbol{k}\neq\boldsymbol{0}} \left(k^2\hat{A}_{\boldsymbol{k},w} + \mathrm{i}k\frac{\partial\hat{A}_{\boldsymbol{k}\parallel}}{\partial w}\right)\mathrm{e}^{\mathrm{i}\boldsymbol{k}\cdot\boldsymbol{x}_S}\,, \tag{6.95}$$

and

$$\hat{\boldsymbol{e}}_w\cdot\boldsymbol{B} = \sum_{\boldsymbol{k}\neq\boldsymbol{0}} \hat{B}_{\boldsymbol{k},w}\mathrm{e}^{\mathrm{i}\boldsymbol{k}\cdot\boldsymbol{x}_S} = \sum_{\boldsymbol{k}\neq\boldsymbol{0}} (\mathrm{i}k\hat{A}_{\boldsymbol{k}\perp})\mathrm{e}^{\mathrm{i}\boldsymbol{k}\cdot\boldsymbol{x}_S}\,. \tag{6.96}$$

Thus, if we define

$$P = \sum_{\boldsymbol{k}\neq\boldsymbol{0}} \hat{P}_{\boldsymbol{k}} \mathrm{e}^{\mathrm{i}\boldsymbol{k}\cdot\boldsymbol{x}_S} \equiv \sum_{\boldsymbol{k}\neq\boldsymbol{0}} (\mathrm{i}\hat{A}_{\boldsymbol{k}\perp}/k)\ \mathrm{e}^{\mathrm{i}\boldsymbol{k}\cdot\boldsymbol{x}_S}\,, \tag{6.97}$$

$$T = \sum_{\boldsymbol{k}\neq\boldsymbol{0}} \hat{T}_{\boldsymbol{k}} \mathrm{e}^{\mathrm{i}\boldsymbol{k}\cdot\boldsymbol{x}_S} \equiv \sum_{\boldsymbol{k}\neq\boldsymbol{0}} \hat{A}_{\boldsymbol{k},w} \mathrm{e}^{\mathrm{i}\boldsymbol{k}\cdot\boldsymbol{x}_S}\,; \tag{6.98}$$

and *impose additionally* that for each $\boldsymbol{k} \neq \boldsymbol{0}$ that

$$\hat{A}_{\boldsymbol{k}\parallel} = 0 \iff \boldsymbol{\nabla}_S \cdot \boldsymbol{A} = 0\,, \tag{6.99}$$

and the global condition (5.73) for the zero-mode $\hat{\boldsymbol{A}}_0$, namely,

$$\int_{V_\mathrm{p}} \hat{\boldsymbol{A}}_0 \cdot \boldsymbol{\nabla} \times \hat{\boldsymbol{A}}_0 \,\mathrm{d}V = \int_{V_\mathrm{p}} \hat{\boldsymbol{A}}_0 \cdot \hat{\boldsymbol{B}}_0 \,\mathrm{d}V = 0\,, \tag{6.100}$$

we obtain precisely the winding gauge $\boldsymbol{A}^\mathrm{W}$ defined in §5.3.

This shows the necessity of the two extra constraints (6.99) and (6.100) for helicity to have a topological, winding-based interpretation, in addition to the usual Hodge decomposition. It is worth noting that Glasser 1974 proved that the periodic Green's functions (4.32) can be derived from Fourier series.

6.5. Examples

In this section, we present two toy examples to illustrate the novel properties of winding helicity in spherical (§6.5.1) and periodic (§6.5.2) domains, respectively.

6.5.1. Bipolar Magnetic Regions in a Global Dipole Field

In §3.3, we considered spherical winding of curves that are not necessarily as $\boldsymbol{B}$-lines. When curves do originate from a divergence-free field, spherical winding helicity $H^W(\boldsymbol{B})$ — total flux-weighted spherical winding of $\boldsymbol{B}$-lines — is a topological invariant under ideal evolution if end-points remain fixed on bounding surfaces (Yeates and Page 2018).

Here, we numerically compute winding helicity on a toy model for solar active regions. Our configuration, as shown in Figure 6.2(a), consists of two localised bipolar magnetic regions (BMRs) centred on the equator, embedded within a (current-free) global dipole field aligned with the polar axis. The BMRs have identical structures with analytical expressions given by Mackay and Ballegooijen 2001; Yeates, Mackay, and van Ballegooijen 2008, and both have a negative twist parameter giving them (negative) "self" helicity, in addition to any "mutual" helicity with each other or the overlying dipole field. Their strengths, denoted B_1 and B_2, are varied. For example, when $B_1 = -B_2$ the two BMRs have opposite polarities. The latter case is shown in Figure 6.2(a) with $\boldsymbol{B}$-lines shown in white and surface magnetic strengths displayed in greyscale.

For an independent verification, we used a spherical implementation of the numerical method of Yeates and Page 2018 which calculates the "minimal helicity" (see also Yeates 2020) by imposing $\boldsymbol{\nabla}_{\mathcal{S}} \cdot \boldsymbol{A}^{\mathrm{W}} = 0$ on bounding surfaces $\mathcal{S}_{r_1}$ and $\mathcal{S}_{r_2}$, equivalent to spherical winding helicity $H^W(\boldsymbol{B})$. The solid lines in Figure 6.2(b) display $H^W(\boldsymbol{B})$ for three cases against the (equatorial) angular separation ξ of the centres of BMRs.

The main prediction is the asymptotics shown by dotted lines in Figure 6.2(b) which were computed by scaling and translating the function

$$\left(\frac{\sin\xi}{1-\cos\xi}\right)^2 = [\Gamma(\xi)]^2 = \frac{1}{[R(\xi)]^2}\,, \tag{6.101}$$

to fit far-field values, where $R(\xi)$ is the distance between BMRs in the stereographically projected plane; cf. (6.57). In each case, both the field strength B_2 and the winding of $\boldsymbol{B}$-lines between BMRs and the overlying dipole contribute to the asymptotic behaviour. The heuristic argument for the two multiplicative factors of $1/R$ in (6.101) is as follows. A spherical field component is "flattened" to its Euclidean equivalent from coordinate transformations, which yields one factor of $1/R$. The other $1/R$ arises from the usual decay of Euclidean winding helicity between two localised magnetic sources.

This result demonstrates the "localising" effect of the non-zero curvature: the "mutual" winding helicity between two regions falls off more strongly with (angular) distance than the Euclidean model.

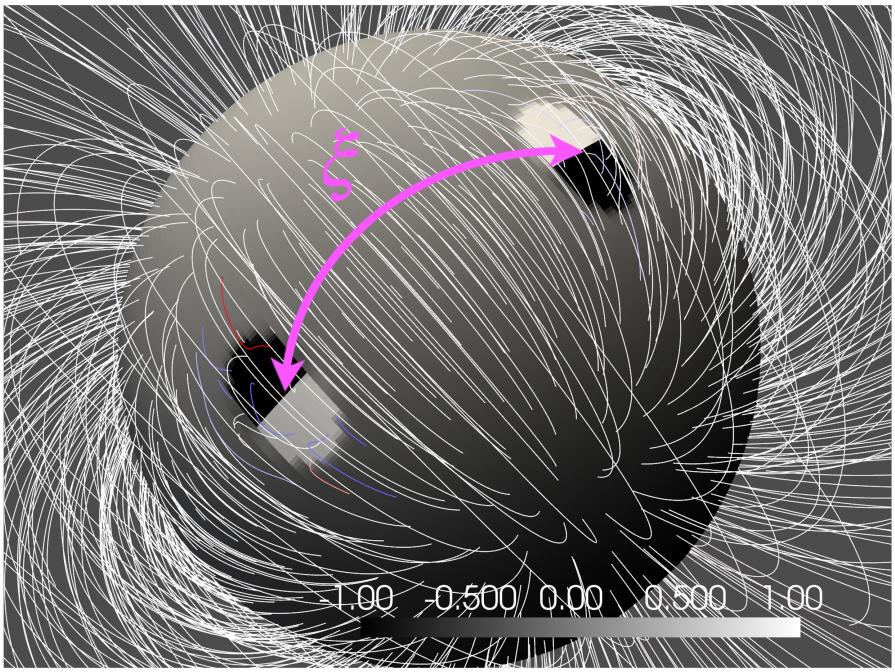

(a)

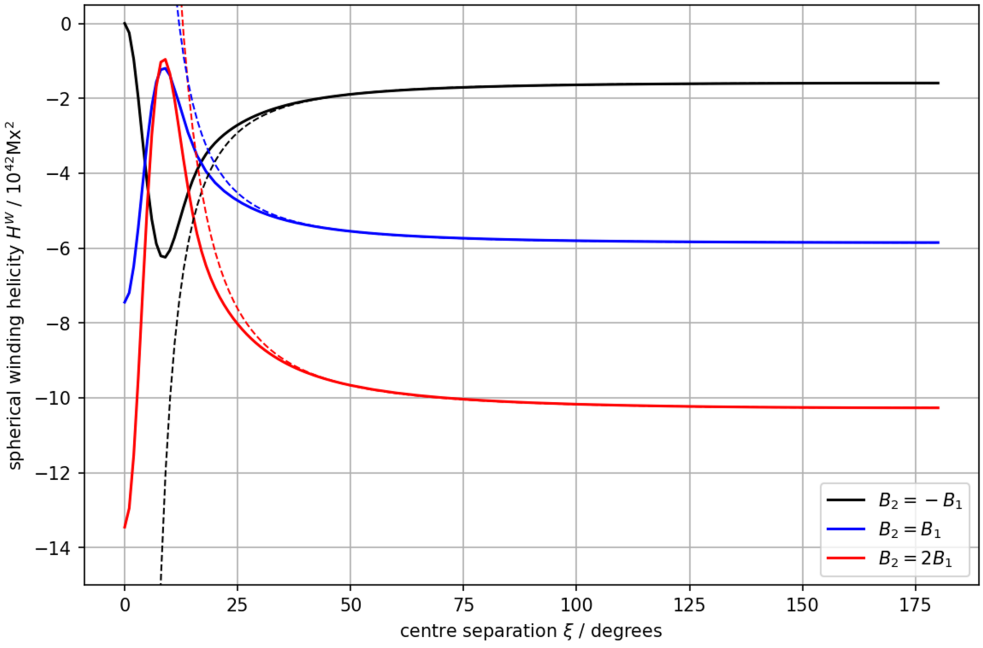

(b)

Figure 6.2: (a). Field lines (in white) and surface magnetic strengths (in greyscale) for a magnetic field composed of two localised BMRs with $B_2 = -B_1$ on the equator and a weak global dipole field that aligns with the polar axis. (b). Spherical winding helicity $H^W(\boldsymbol{B})$ (solid) against the (equatorial) angular separation ξ of the centres of BMRs, with theoretical predictions (6.101) (dotted) for far-field decays.

6.5.2. ABC Field with Additional Harmonic Components

In §4.3, we considered examples of winding of curves in periodic domains V_{p}, observing novel features due to our new concept of winding. Here, we numerically compute periodic winding helicity $H^{\mathrm{W}}(\boldsymbol{B})$ - total, flux-weighted periodic winding of $\boldsymbol{B}$-lines - of the Arnold-Beltrami-Childress (ABC) magnetic field (Dombre et al. 1986) $\boldsymbol{B}_{\mathrm{ABC}}(\boldsymbol{x})$:

$$\boldsymbol{B}_{\mathrm{ABC}}(\boldsymbol{x}) = \big(A\sin\tilde{w} + C\cos\tilde{y}\big)\hat{\boldsymbol{e}}_x + \big(B\sin\tilde{x} + A\cos\tilde{w}\big)\hat{\boldsymbol{e}}_y + \big(C\sin\tilde{y} + B\cos\tilde{x}\big)\hat{\boldsymbol{e}}_w\,, \tag{6.102}$$

with $\tilde{\boldsymbol{x}} \equiv 2\pi\boldsymbol{x}$ and A, B, C as fixed real constants.

Note that $\boldsymbol{B}_{\mathrm{ABC}}$ is periodic in all x, y, and w directions with vanishing harmonic fluxes, $(\boldsymbol{B}_{\mathrm{ABC}})_0 = \boldsymbol{0}$. For reference, Figure 6.3 shows a 3D streamline plot of $\boldsymbol{B}_{\mathrm{ABC}}$ with $A = B = C = 1$, which will be used later. To illustrate the effects of harmonic fluxes, which are newly incorporated features in this formalism, we add a constant harmonic field $\boldsymbol{B}_{\mathrm{H}}$ to $\boldsymbol{B}_{\mathrm{ABC}}$, i.e., we consider helicity of the total field

$$\boldsymbol{B} = \boldsymbol{B}_{\mathrm{ABC}} + \boldsymbol{B}_{\mathrm{H}}\,. \tag{6.103}$$

Also, since $H^{\mathrm{W}}(\boldsymbol{B})$ is a single number for the entire field, we instead consider the finer-grained, spatial distribution of the integrand of (6.3) at some height w (up to a factor), i.e., (periodic) *winding helicity density* $\mathcal{H}_{\mathrm{p}}(z, w; \boldsymbol{B})$ (which integrates to $H^{\mathrm{W}}(\boldsymbol{B})$), defined by

$$\mathcal{H}_{\mathrm{p}}(z, w; \boldsymbol{B}) = \int_{\mathcal{S}_w} \omega_{\mathrm{p}}(w; \gamma, \gamma') B_w(z) B_w(z')\ \mathrm{d}A_{z'}\ . \tag{6.104}$$

Results of $\mathcal{H}_{\mathrm{p}}$ at $w = 0.5$ are plotted in Figure 6.4, as well as its Euclidean analogue $\mathcal{H}_{\mathrm{E}}$ (replacing ω_{p} with ω_{E} and V_{p} with V_{E} in (6.104)) and their differences.

Note that the computation of $\mathcal{H}_{\mathrm{E}}$ assumes $|\boldsymbol{B}| \to 0$ rapidly outside $\mathcal{S}$, also known as "zero padding". For the same choice of $\boldsymbol{B}_{\mathrm{H}}$ (in each row), we have $|\mathcal{H}_{\mathrm{p}}| < |\mathcal{H}_{\mathrm{E}}|$, exhibiting the similar "localising" effect due to periodicity. Meanwhile, the spatial distributions of $\mathcal{H}_{\mathrm{p}}$ display more periodicity (likely inherited from the domain). It is necessary employ the correct expression as it would be difficult to quantify the differences that would arise.

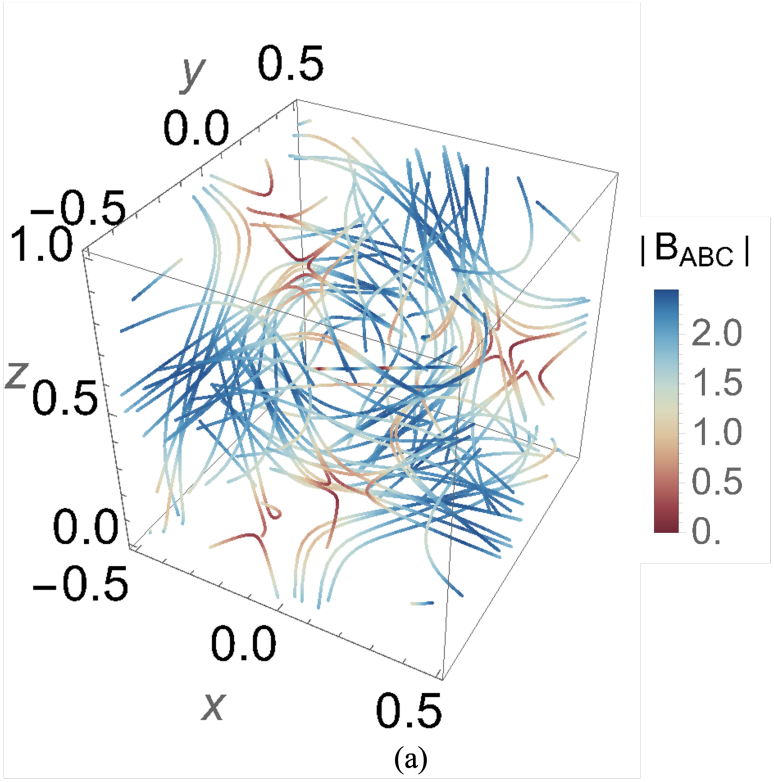

Figure 6.3: (a). $\boldsymbol{B}$-lines of $\boldsymbol{B}_{\mathrm{ABC}}$ coloured by the magnitude of field strength and (b). magnetic field strength at $z = 0.5$ in the horizontal direction with uncoloured streamlines.

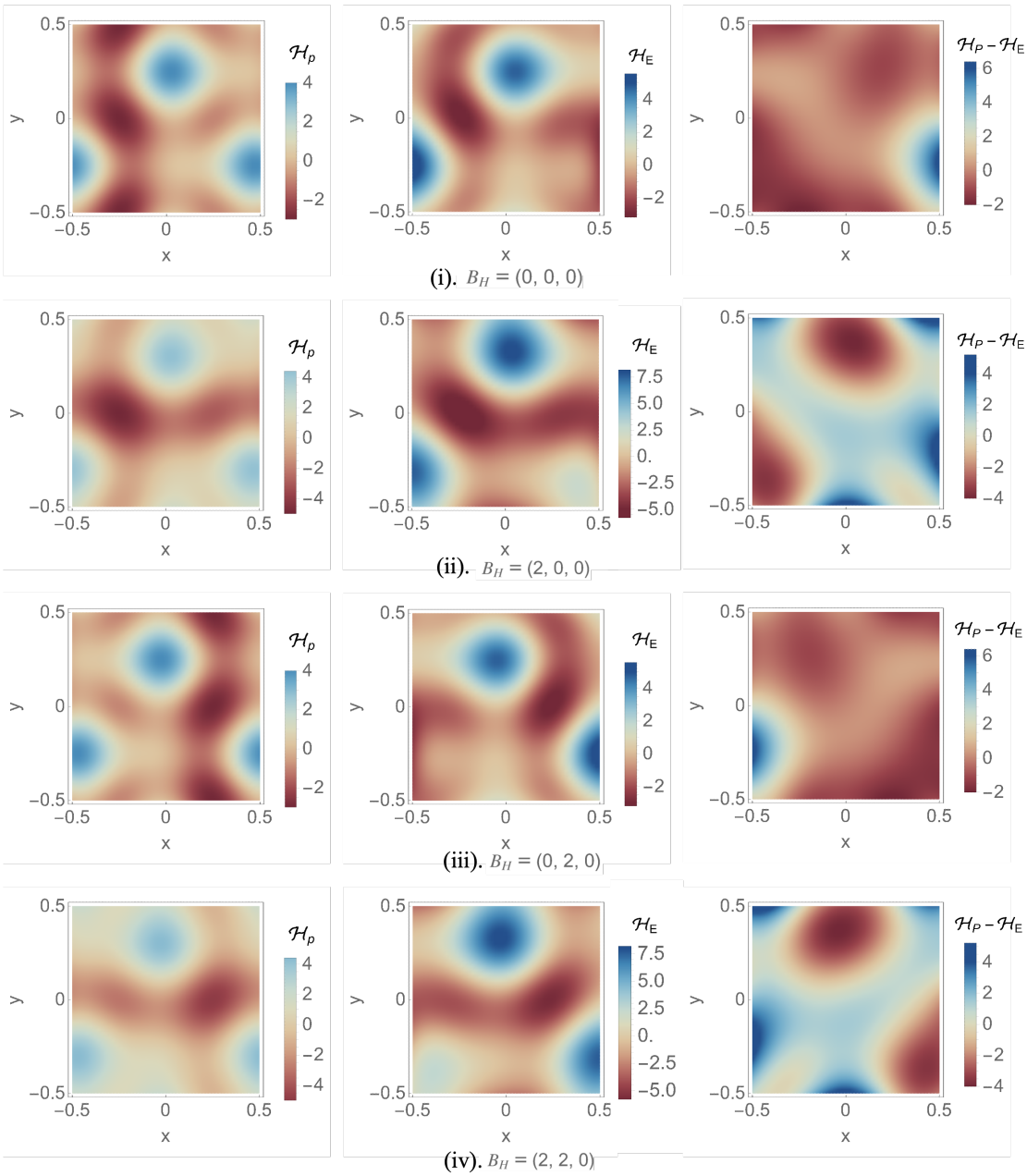

Figure 6.4: Spatial distributions of periodic winding helicity density $\mathcal{H}_{\mathrm{p}}$, (6.104) and its Cartesian version $\mathcal{H}_{\mathrm{E}}$, of $\boldsymbol{B} = \boldsymbol{B}_{\mathrm{ABC}} + \boldsymbol{B}_{\mathrm{H}}$, as well as their differences, for different choices of $\boldsymbol{B}_{\mathrm{H}}$. The same colour scales are used, in the first two panels, for the same $\boldsymbol{B}_{\mathrm{H}}$ in each row.

Chapter 7

Case Study: Spherical Winding Magnetic Helicity for SHARP Magnetograms

In this chapter[1], results from a case study are presented to exhibit the quantitative influence of spherical geometry on (magnetic) winding and winding (magnetic) helicity. The data source is SHARP (Space-weather HMI Active Region Patches) magnetograms from the Helioseismic and Magnetic Imager (HMI) onboard the NASA spacecraft Solar Dynamical Observatory (SDO). §7.1 presents the astrophysical motivation and provides necessary background for general readers. §7.2 is a brief review of the definitions of winding and winding helicity in both Euclidean and spherical domains. §7.3 introduces key properties of the cylindrical equal-area (CEA) projection used by SHARP magnetograms in previous Euclidean approximations. Then, in §7.4, the densities of winding and winding helicity are computed in both geometries for an analysis of the absolute and relative errors that would have been incurred. The key findings are summarised in §7.5.

[1]Adapted from D. Xiao, C. B. Prior, and A. R. Yeates (2023b). "Computation of Winding-Based Magnetic Helicity and Magnetic Winding Density for SHARP Magnetograms in Spherical Coordinates". In: *Solar Phys.* 298, p. 116.

7.1. Motivation

For solar magnetically active regions (AR), significant changes in winding and/or helicity correspond to magnetic reconnection events and are often correlated with the onset of solar eruption and coronal mass ejections (e.g., LaBonte, Georgoulis, and Rust 2007; Soós et al. 2022; Thalmann, Moraitis, Linan, et al. 2019; Wyper, S. Antiochos, and DeVore 2017). However, since ARs mostly have open (magnetic) fields[2], alternative definitions of helicity immune to gauge ambiguities must be used for helicity to be compared for different ARs, as reviewed in §1.3.1. This includes the uses of relative helicity introduced in §1.3.3 (e.g., Hawkes and Yeates 2019; Liu and Schuck 2013) and winding helicity considered throughout and in this chapter (see also e.g., Raphaldini, Prior, and MacTaggart 2022).

Although the ARs that are responsible for some of the most powerful solar activities span a large proportion of the solar disc (e.g., the one shown in Figure 7.2), the intrinsic curvature of the photosphere has been only partially accounted for in studies involving helicity and/or winding (e.g., Liu and Schuck 2012; MacTaggart and Prior 2021; Vemareddy 2019). Magnetic field components in spherical coordinates are incorrectly used on Euclidean projections of photospheric patches, mostly in CEA projections, to match vector magnetograms provided by SHARP (Hoeksema, Liu, Hayashi, et al. 2014). Nevertheless, several studies have started including the full spherical geometry in their computation of relative helicity (see Moraitis, Pariat, Savcheva, et al. 2018 and references therein).

Given the little consensus on which definitions, assumptions, and approximations should be adopted, the geometrical formalism proposed in Chapter 4 and §6.3 (Xiao, Prior, and Yeates 2023a) seems a promising candidate. It provides intrinsically spherical, closed-form expressions for winding helicity and winding directly in terms of the observed magnetic field in the native spherical coordinates, which can facilitate a numerical investigation into the rôle of spherical geometry in winding and helicity computations. The primary goal here is to confirm quantitatively that curvature effects indeed become more significant as AR sizes increase, as first predicted qualitatively in Gary and Hagyard

[2]with respect to a domain with the photosphere, or the visible solar surface, as the lower boundary.

1990.

7.2. Winding & Winding Helicity in Euclidean & Spherical Domains

Here, the geometrical definition of Euclidean and spherical winding helicity derived in Chapter 6 will be briefly reviewed for reference (also from Chapters 2 and 3).

On a certain (vertical) w-level, recall that the mutual entanglement of a pair of $\boldsymbol{B}$-lines through points $\boldsymbol{x}$ and $\boldsymbol{x}'$ along the w-direction can be measured by the *Euclidean (pairwise) winding rate*, defined by

$$\omega_{\mathrm{E}}(w;\boldsymbol{x},\boldsymbol{x}') = \frac{-1}{2\pi|\boldsymbol{x}-\boldsymbol{x}'|}\left[\frac{B_\chi(\boldsymbol{x})}{B_w(\boldsymbol{x})}+\frac{B_\chi(\boldsymbol{x}')}{B_w(\boldsymbol{x}')}\right], \tag{7.1}$$

with components

$$B_w(\boldsymbol{x}) = \boldsymbol{B}(\boldsymbol{x})\cdot\hat{\boldsymbol{e}}_w(\boldsymbol{x}), \qquad B_\chi(\boldsymbol{x}) = \boldsymbol{B}(\boldsymbol{x})\cdot\hat{\boldsymbol{e}}_w(\boldsymbol{x})\times\frac{\boldsymbol{x}'-\boldsymbol{x}}{|\boldsymbol{x}'-\boldsymbol{x}|}; \tag{7.2}$$

and similarly for $B_w(\boldsymbol{x}')$ and $B_\chi(\boldsymbol{x}')$ with $\boldsymbol{x}\leftrightarrow\boldsymbol{x}'$ (same below).

In the spherical case, the analogous spherical winding rate in the (radial) r-direction for $\boldsymbol{B}$-lines through $\boldsymbol{x}$ and $\boldsymbol{x}'$ at the same r-level is given by

$$\omega_{\mathrm{s}}(r;\boldsymbol{x},\boldsymbol{x}') = \frac{-1}{4\pi r}\frac{\sin\xi}{1-\cos\xi}\left[\frac{B_\chi(\boldsymbol{x})}{B_r(\boldsymbol{x})}+\frac{B_\chi(\boldsymbol{x}')}{B_r(\boldsymbol{x}')}\right], \tag{7.3}$$

where $\xi(\boldsymbol{x},\boldsymbol{x}') = \arccos\big(\boldsymbol{x}\cdot\boldsymbol{x}'/r^2\big)$ is the spherical distance between $\boldsymbol{x}$ and $\boldsymbol{x}'$, and relevant field components are defined as

$$B_r(\boldsymbol{x}) = \boldsymbol{B}(\boldsymbol{x})\cdot\hat{\boldsymbol{e}}_r(\boldsymbol{x}), \qquad B_\chi(\boldsymbol{x}) = \boldsymbol{B}(\boldsymbol{x})\cdot\frac{\hat{\boldsymbol{e}}_r(\boldsymbol{x})\times\boldsymbol{x}'}{|\hat{\boldsymbol{e}}_r(\boldsymbol{x})\times\boldsymbol{x}'|}. \tag{7.4}$$

Here, $\hat{\boldsymbol{e}}_r(\boldsymbol{x}) = \boldsymbol{x}/r$ and $|\boldsymbol{x}\times\boldsymbol{x}'| = r^2\sin\xi$. Both the Euclidean and spherical winding rates are illustrated in Figure 7.1, and they only depend on pointwise information about the

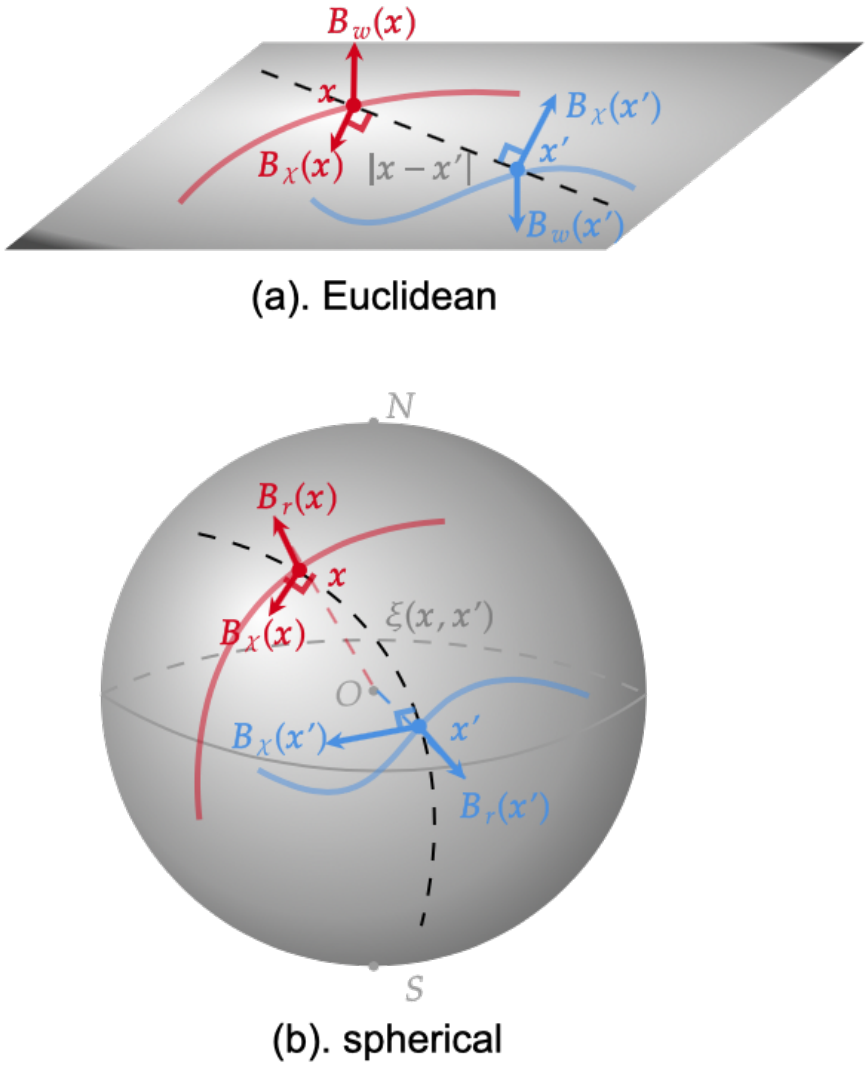

Figure 7.1: Pairwise winding rates defined on (a) Euclidean planes and (b) spheres.

magnetic fields.

By integrating them over all pairs of points on each ζ-level S_ζ, where ζ is either w (Euclidean) or r (spherical), and then over all ζ, *(magnetic) winding* is defined as (see also Prior and MacTaggart 2020)

$$L^{\mathrm{W}}(\boldsymbol{B}) = \int_{\zeta_0}^{\zeta_1} \int_{S_\zeta} \int_{S_\zeta} \omega(\zeta; \boldsymbol{x}, \boldsymbol{x}') \, \mathrm{d}^2\boldsymbol{x}' \, \mathrm{d}^2\boldsymbol{x} \, \mathrm{d}\zeta \,, \tag{7.5}$$

and *winding (magnetic) helicity* as

$$H^{\mathrm{W}}(\boldsymbol{B}) = \int_{\zeta_0}^{\zeta_1} \int_{S_\zeta} \int_{S_\zeta} \omega(\zeta; \boldsymbol{x}, \boldsymbol{x}') B_\zeta(\boldsymbol{x}) B_\zeta(\boldsymbol{x}') \, \mathrm{d}^2\boldsymbol{x}' \mathrm{d}^2\boldsymbol{x} \, \mathrm{d}\zeta \,. \tag{7.6}$$

In both case, L^{W} and H^{W} are topological invariants based only on the magnetic field and the domain (Prior and Yeates 2021).

In this case study, instead of the full integrals (7.5) and (7.6), we will only consider the photospheric ($\zeta = \zeta_0$) contributions in *finite* S_{ζ_0} patches that correspond to individual SHARPs. Specifically, when referring to winding or helicity, we mean:

$$L^{\mathrm{W}}(\zeta_0) = \int_{S_{\zeta_0}} \left(\int_{S_{\zeta_0}} \omega(\zeta; \boldsymbol{x}, \boldsymbol{x}') \mathrm{d}^2\boldsymbol{x}' \right) \mathrm{d}^2\boldsymbol{x} = \int_{S_{\zeta_0}} \mathcal{L}^{\mathrm{W}}(\boldsymbol{x}; \zeta_0) \mathrm{d}^2\boldsymbol{x}, \tag{7.7}$$

and

$$H^{\mathrm{W}}(\zeta_0) = \int_{S_{\zeta_0}} \left(\int_{S_{\zeta_0}} \omega(\zeta; \boldsymbol{x}, \boldsymbol{x}') B_\zeta(\boldsymbol{x}) B_\zeta(\boldsymbol{x}') \mathrm{d}^2\boldsymbol{x}' \right) \mathrm{d}^2\boldsymbol{x} = \int_{S_{\zeta_0}} \mathcal{H}^{\mathrm{W}}(\boldsymbol{x}; \zeta_0) \mathrm{d}^2\boldsymbol{x} \,. \tag{7.8}$$

The inner integrals $\mathcal{L}^{\mathrm{W}}(\boldsymbol{x}; \zeta_0)$ and $\mathcal{H}^{\mathrm{W}}(\boldsymbol{x}; \zeta_0)$ are spatial distributions which serve as finer-grained measures than $L^{\mathrm{W}}(\boldsymbol{B})$ and $H^{\mathrm{W}}(\boldsymbol{B})$. We outline two reasons for choosing finite surface densities over full volume integrals:

1. Magnetograms are *only* available as finite patches on the photosphere $\zeta = \zeta_0$, and it is standard to perform computations of helicity and winding on finite domains (e.g., Liu and Schuck 2012; MacTaggart, Prior, et al. 2021; Pariat, Nindos, et al. 2006). Assuming particular boundary conditions or field extrapolations would prejudice the results, whereas the winding-based definition of helicity allows meaningful and

consistent comparisons between two geometries even in finite domains.

2. Winding helicity (or winding) density has a very similar form to that for helicity (or winding) flux through the photosphere, except that the latter also involves plasma velocities (e.g., Liu and Schuck 2013; MacTaggart and Prior 2021; Pariat, Démoulin, and Berger 2005). More uncertainties, however, would be introduced from computing the latter from velocity inversions (e.g., Schuck 2008; S. Yang, Zhang, and Büchner 2009) which we would like to avoid. The comparisons between Euclidean and spherical helicity (or winding) calculations can be used as an indicator of the effect of ignoring spherical geometry in helicity (or winding) flux calculations.

7.3. SHARP Magnetograms in Cylindrical Equal-Area (CEA) Projection

SHARP magnetograms are available in two projected coordinates: CCD image coordinates (keyword `hmi.sharp_720s`) and re-centred cylindrical equal-area (CEA) projection coordinates (keyword `hmi.sharp_cea_720s`), as illustrated in Figure 7.2 for SHARP 4920.

The standard CEA projection maps a point with spherical coordinates (λ, ϕ) to CEA coordinates (x^*, y^*) as follows (see e.g., Calabretta and Greisen 2002):

$$x^* = \phi, \tag{7.9}$$

$$y^* = \sin\lambda, \tag{7.10}$$

where $\lambda = \pi/2 - \theta$ is the latitude. Figure 7.3(a) provides an example when (7.9) and (7.10) are applied to the Earth, first known as the Lambert's[3] equal-area projection (Lambert 1759). Note that lines of constant λ and ϕ are mapped to a rectangular grid, manifesting the *cylindrical* nature. It is called *equal-area* since each CEA pixel corresponds to the same area on the sphere, so (relative) region sizes can be accurately captured and magnetic flux can be directly computed from magnetograms. However, the CEA projection is not

[3]Johann Heinrich Lambert, French (or Swiss), 1728-1777

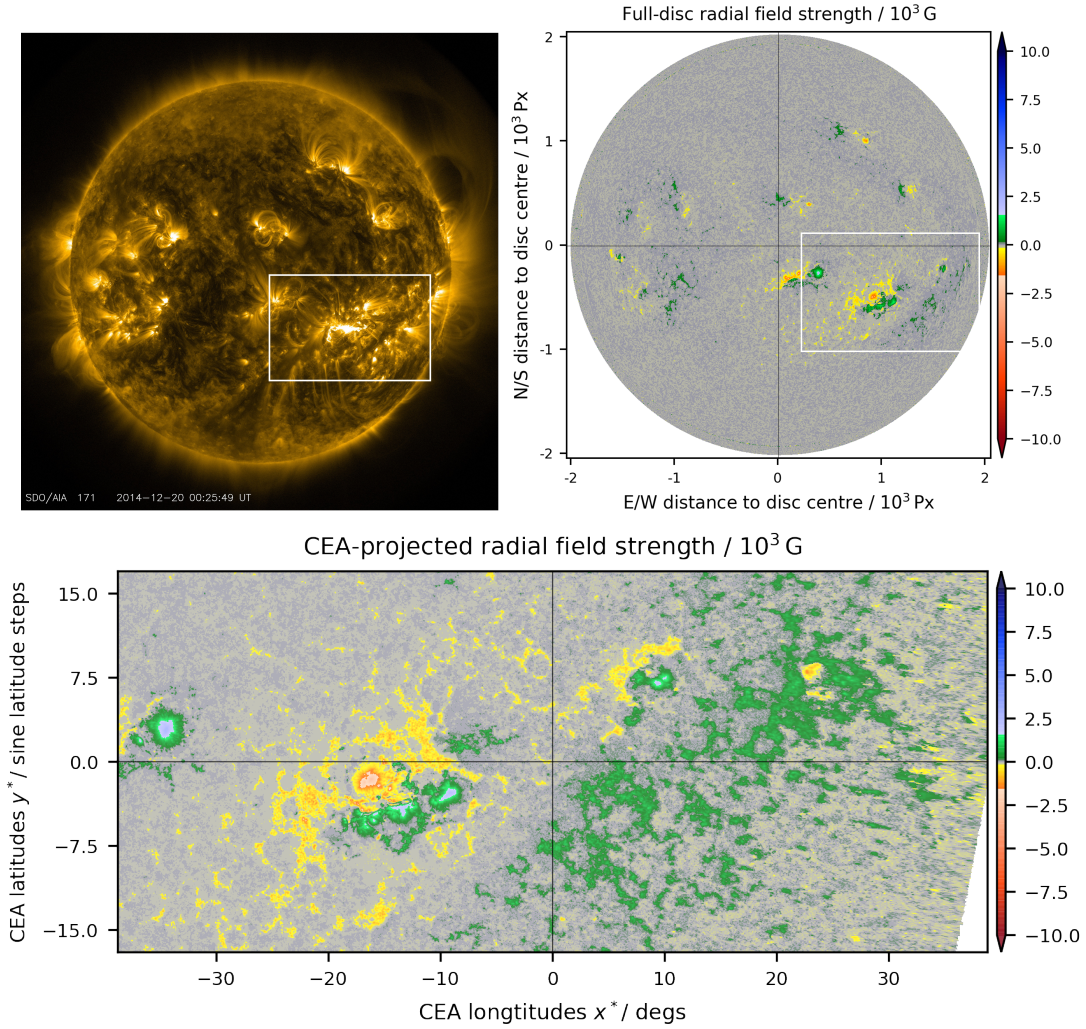

Figure 7.2: SHARP 4920 on 20 December 2014 at 00:24:00 is shown in CCD coordinates in the 171Å EUV channel (upper left, white box) and in the full-disc radial magnetogram (upper right, indicated by the white box), as well as in the re-centred CEA magnetogram (bottom).

conformal or angle-preserving, and angular distortions could lead to significant errors in helicity and winding which are both based on angular measures.

This deformation, however, can be greatly reduced by choosing the projection centre close to the region of interest. Figure 7.3(b), for instance, displays a CEA-projected European map that is re-centred to Royal Greenwich Observatory in London with $(\lambda_C, \phi_C) = (+51.5°, 0)$, so that Europe appears much less distorted.

7.3.1. Derivation of the Re-centred CEA Projection

In what follows is a comprehensive yet elementary derivation of the re-centred CEA projection which may be difficult to obtain directly from literature, e.g., Calabretta and Greisen 2002; Sun 2022. The key idea is to pre-compose the standard version, (7.9)-(7.10), with a spherical rotation, as shown in Figure 7.4. Here, $\Upsilon(0,0)$ is the projection centre and $\lambda = 0$ is the reference circle (through Υ and its antipodal point). Note that local distortions are quantified by the Jacobian of (7.9) and (7.10),

$$J = \cos\lambda\,, \tag{7.11}$$

so regions closer to the equator $\lambda = 0$ appear less distorted. This suggests that by choosing a new projection centre $C(\lambda_\mathrm{C}, \phi_\mathrm{C})$ and a new reference circle, regions of interest can be mapped by the CEA projection to more accurate images.

Let $\mathsf{R}_i(\theta)$ be an anticlockwise rotation of angle θ about the (current) Cartesian axis $i \in \{x, y, w\}$. Then, the combined spherical rotation,

$$\mathsf{R} = \mathsf{R}_y(-\lambda_\mathrm{C})\mathsf{R}_w(\phi_\mathrm{C}) = \begin{pmatrix} \cos\lambda_\mathrm{C} & 0 & -\sin\lambda_\mathrm{C} \\ 0 & 1 & 0 \\ \sin\lambda_\mathrm{C} & 0 & -\cos\lambda_\mathrm{C} \end{pmatrix} \begin{pmatrix} \cos\phi_\mathrm{C} & -\sin\phi_\mathrm{C} & 0 \\ \sin\phi_\mathrm{C} & \cos\phi_\mathrm{C} & 0 \\ 0 & 0 & 1 \end{pmatrix}, \tag{7.12}$$

transforms the underlying coordinates. Under R, the new projection centre $C(\lambda_\mathrm{C}, \phi_\mathrm{C})$ has rotated coordinates $C(\tilde{\lambda}_\mathrm{C}, \tilde{\phi}_\mathrm{C}) = (0, 0)$, i.e.,

$$\mathsf{R}[C(\lambda_\mathrm{C}, \phi_\mathrm{C})] = \mathsf{R} \begin{pmatrix} \cos\lambda_\mathrm{C}\cos\phi_\mathrm{C} \\ \cos\lambda_\mathrm{C}\sin\phi_\mathrm{C} \\ \sin\lambda_\mathrm{C} \end{pmatrix} = \begin{pmatrix} 1 \\ 0 \\ 0 \end{pmatrix} \implies C(\tilde{\lambda}_\mathrm{C}, \tilde{\phi}_\mathrm{C}) = (0, 0)\,, \tag{7.13}$$

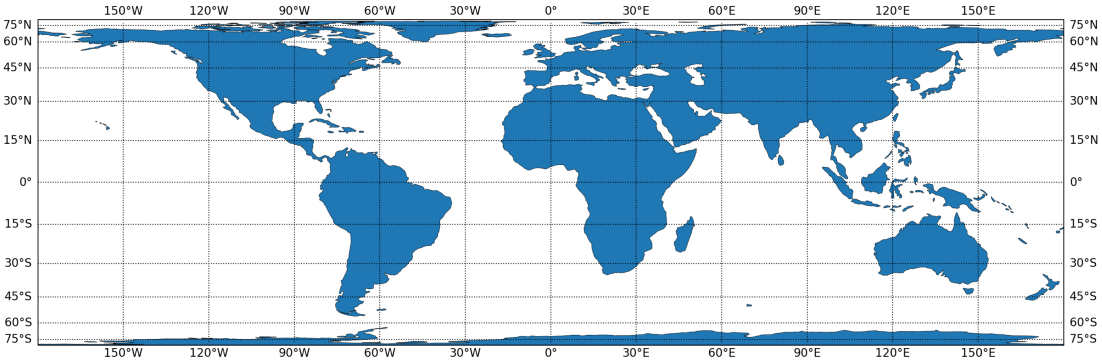

(a)

(b)

Figure 7.3: Cylindrical equal-area projection applied to the world map in (a) centred on $(\lambda_C, \phi_C) = (0, 0)$, and in (b) centred on Greenwich (marked with a star) with $(\lambda_C, \phi_C) = (+51.5°, 0)$. Distortions in Europe are clearly reduced once the projection is re-centred.

which is also shown in Figure 7.4. Now, note that

$$\mathsf{R}[P(\lambda,\phi)] = \mathsf{R}\begin{pmatrix}\cos\lambda\cos\phi\\ \cos\lambda\sin\phi\\ \sin\lambda\end{pmatrix} = \begin{pmatrix}\sin\lambda\sin\lambda_{\mathrm{C}} + \cos\lambda_{\mathrm{C}}\cos\lambda\cos(\phi-\phi_{\mathrm{C}})\\ \cos\lambda\sin(\phi-\phi_{\mathrm{C}})\\ \cos\lambda_{\mathrm{C}}\sin\lambda - \sin\lambda_{\mathrm{C}}\cos\lambda\cos(\phi-\phi_{\mathrm{C}})\end{pmatrix}, \tag{7.14}$$

so P has rotated coordinates $(\tilde{\lambda},\tilde{\phi})$ given by

$$\tilde{\lambda} = \arcsin\left[\cos\lambda_{\mathrm{C}}\sin\lambda - \sin\lambda_{\mathrm{C}}\cos\lambda\cos(\phi-\phi_{\mathrm{C}})\right], \tag{7.15}$$

$$\tilde{\phi} = \texttt{atan2}\left[\frac{\cos\lambda\sin(\phi-\phi_{\mathrm{C}})}{\sin\lambda\sin\lambda_{\mathrm{C}} + \cos\lambda_{\mathrm{C}}\cos\lambda\cos(\phi-\phi_{\mathrm{C}})}\right], \tag{7.16}$$

where `atan2` is the signed arctan function. Combining with the standard CEA projection (7.9) and (7.10) yields the re-centred version:

$$x^* = \tilde{\phi}, \tag{7.17}$$

$$y^* = \sin\tilde{\lambda}. \tag{7.18}$$

7.3.2. Representation of Magnetic Fields in SHARP

In SHARP magnetograms (Bobra, Sun, Hoeksema, et al. 2014; Hoeksema, Liu, Hayashi, et al. 2014), magnetic field components are provided in the local spherical basis $(\hat{\boldsymbol{e}}_r, \hat{\boldsymbol{e}}_\theta, \hat{\boldsymbol{e}}_\phi)$ and the numerical grid is CEA-projected, both converted from CCD coordinates. Here, $\hat{\boldsymbol{e}}_r$ is normal to solar surface, $\hat{\boldsymbol{e}}_\theta$ (or $\hat{\boldsymbol{e}}_\phi$) points southward (or westward) in the direction of solar rotation. In most studies that we are aware of, helicity and winding for SHARP and ARs are computed using the Euclidean equations (7.1) and (7.2), approximating both the CEA grid and the spherical field components as Euclidean. In particular, $(\hat{\boldsymbol{e}}_\theta, \hat{\boldsymbol{e}}_\phi)$ is treated as $(\hat{\boldsymbol{e}}_{y^*}, -\hat{\boldsymbol{e}}_{x^*})$, where the inherent CEA basis vectors $\hat{\boldsymbol{e}}_{x^*}$ and $\hat{\boldsymbol{e}}_{y^*}$ point along lines of constant x^* or y^*. Key information is summarised in Table 7.1.

Taking SHARP 4920 in Figure 7.2 as an example, we computed, according to Equation (9) in Sun 2022, the misalignment between the two bases, as shown in Figure 7.5. Significant discrepancies that are greater than 10° can be observed towards patch corners. However, the errors involved therein can still be challenging to be quantified. Using the

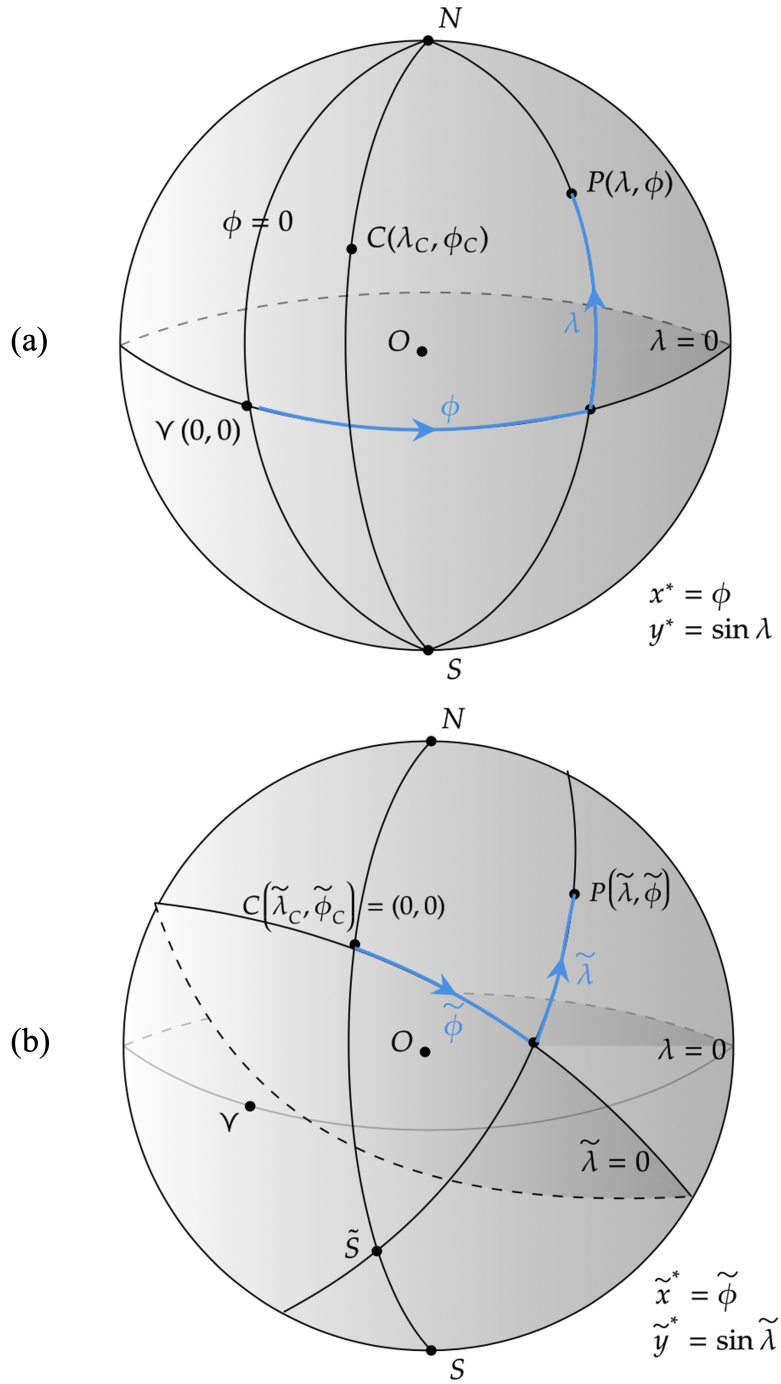

Figure 7.4: (a) Standard and (b) re-centred CEA maps with projection centres at $(0, 0)$ and (λ_C, ϕ_C), respectively. Tildes are used to indicate the rotated spherical coordinates under R.

Approach	Key Expressions	Geometry	Numerical Grid	Field Components
Euclidean/CEA	(7.1), (7.2), (7.7), (7.8)	Euclidean	CEA	(B_r, B_θ, B_ϕ)
Spherical	(7.3), (7.4), (7.7), (7.8)	Spherical	Spherical	(B_r, B_θ, B_ϕ)

Table 7.1: Summary of Euclidean/CEA and spherical approaches.

fully spherical formalism of winding and winding helicity reviewed in §7.2, it is natural to examine the extent to which Euclidean approximations fail to be accurate for SHARP magnetograms.

For subsequent computations, it is worth noting that SHARP sizes are measured in either CEA-projected degrees x^* (longitudes) and y^* (latitudes) or photospheric areas in units of millionths of a solar hemisphere (mH). From Bobra, Sun, Hoeksema, et al. 2014, each CEA pixel has a constant x^*-dimension of $\Delta x^* = 0.03°$ in heliographic degrees, so the x^*-coordinate of the nth pixel is given by

$$x^*_n = n\Delta x^* \,, \tag{7.19}$$

where n is an integer and $n = 0$ corresponds to the patch/projection centre. In contrast, y^* are measured in constant steps of sines, which implies the nth pixel's y^*-dimension, denoted by $\Delta y^*(y^*_n)$, is a *non-linear* function of its y^*-coordinate y^*_n:

$$\sin\left[\Delta y^*(y^*_n)\right] - \sin\left[\Delta y^*(y^*_{n-1})\right] = 0.03° \times \frac{\pi}{180°} \,, \tag{7.20}$$

where $\Delta y^*(y^*_0) = 0.03°$. This recursively gives

$$y^*_n = y^*_{n\pm1} + \Delta y^*(y_{n\pm1}) \,, \tag{7.21}$$

with $+$ (or $-$) for $n > 0$ (or $n < 0$). Moreover, each CEA pixel has an area of 1.3×10^{15} cm^2, used in the comparisons between Euclidean and spherical results.

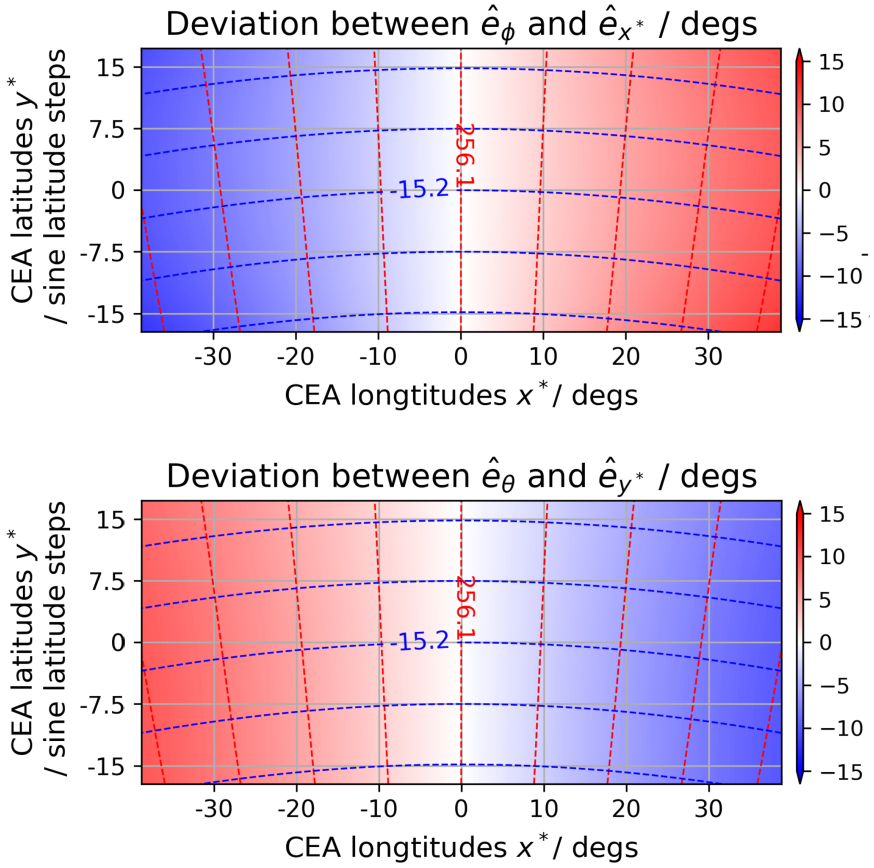

Figure 7.5: Angular deviation between the spherical basis $(\hat{e}_\theta, \hat{e}_\phi)$ used for field components and the CEA basis $(\hat{e}_{x^*}, \hat{e}_{y^*})$ for the underlying numerical grid, both computed for SHARP 4920 in Figure 7.2. The CEA-origin coincides with the patch/projection centre $(\lambda_c, \phi_c) = (-15.2°, 256.1°)$. Parallels (blue) and meridians (red) with step-sizes 7.5° and 10°, respectively, are also shown.

7.4. Numerical Results

In this section, we compute and compare densities of winding-based helicity $H^{\mathrm{W}}(\zeta_0)$ and winding $L^{\mathrm{W}}(\zeta_0)$ for a selection of SHARP magnetograms from Solar Cycle 24 (December 2008 - December 2019), in both Euclidean and spherical coordinates. Note that, to implement the spherical approach, the numerical grid of a given SHARP magnetogram first needs to be converted to spherical coordinates using the relevant re-centred CEA projection (7.17) and (7.18). The YY.MM.DD format is used for observation dates and HH.MM for observation times, both in the Universal Time. We adopt the CGS system of units, so magnetic field strengths are measured in units of gauss (G), flux in maxwell (Mx), helicity density in $\mathrm{G}^2 \cdot \mathrm{cm}^3 = \mathrm{Mx}^2/\mathrm{cm}$ from (7.8), and winding density in cm^3 from (7.7).

7.4.1. Spatial Distributions of Errors

We first compute spatial distributions of local winding helicity density $\mathcal{H}^{\mathrm{W}}(\boldsymbol{x};\zeta_0)$ from (7.8) and winding density $\mathcal{L}^{\mathrm{W}}(\boldsymbol{x};\zeta_0)$ from (7.7) in both Euclidean and spherical coordinates. Note that the surface-integrated helicity and winding, $H^{\mathrm{W}}(\zeta_0)$ and $L^{\mathrm{W}}(\zeta_0)$, can be recovered from integrating the local quantities over the patch on $\zeta = \zeta_0$. To analyse the results, we use both the absolute errors $P_{\mathrm{Euc}} - P_{\mathrm{sph}}$ (i.e., the difference between Euclidean approximation and spherical value) and relative errors $(P_{\mathrm{Euc}} - P_{\mathrm{sph}})/P_{\mathrm{sph}}$, where P denotes local helicity or winding density and the subscript denotes the method used. We choose snapshots of two SHARP, 3926 (medium-sized, relatively quiet) and 4920 (large-sized, very active and flaring); see Table 7.2 for details.

SHARP No.	NOAA AR No.	Date & Time	Solar Location	Projected Size (CEA degs)	Area (10^3 mH)	Flare?
3926	12022	14.04.01_00:00	Near centre	$28.0° \times 10.9°$	6.2	No
4920	12242+	14.12.20_00:24	Near limb	$77.6° \times 34.0°$	31.0	Yes

Table 7.2: SHARP chosen for (field line) helicity and winding computations in Figures 7.6 and 7.7, where "12242+" stands for 12235, 12237, 12238, 12242.

Results are shown in Figure 7.6 and key observations are summarised as follows:

(a) Absolute errors are greatest near regions with strong fields or large actual values of helicity or winding. In contrast, relative errors generally do not exhibit such behaviour - most large values are physically insignificant caused by near-zero denominators.

(b) Errors in helicity are more localised likely due to sharp drops in field strengths outside ARs, but errors in winding are more disperse likely because winding is not flux-weighted.

(c) Compared to the actual values, the smaller, quieter SHARP 3926 has maximum absolute errors an order of magnitude lower, whereas for the larger, more active SHARP 4920 they are of the same order of magnitude. This confirms that the patch size and/or total flux are contributing factors to the differences between the two methods, as expected from §7.2.

7.4.2. Time Series of Errors

Errors in the Euclidean approximation for one particular snapshot could have been caused by observational noise, so it is important to test the robustness of errors over extended periods. Here, we compute time series for both absolute and relative errors (defined in §7.4.1) of the surface-integrated helicity $H^{\mathrm{W}}(\zeta_0)$ from (7.8) and winding densities $L^{\mathrm{W}}(\zeta_0)$ from (7.7) in both spherical and Euclidean coordinates. For consistency, the same SHARP 3926 and 4920 are used with relevant temporal information in Table 7.3.

No.	Start Date & Time	End Date & Time	Cadence	Total Snapshots	≥M Flares
3926	14.03.29_00:00	14.04.07_00:00	60 mins	216	No
4920	14.12.19_20:00	14.12.20_06:00	12 mins	50	Yes

Table 7.3: Temporal information of SHARP chosen for helicity and winding computations in Figure 7.7.

From results plotted in Figure 7.7, both series exhibit persistent errors of comparable order of magnitude to the actual values. Excluding non-physically large values, relative

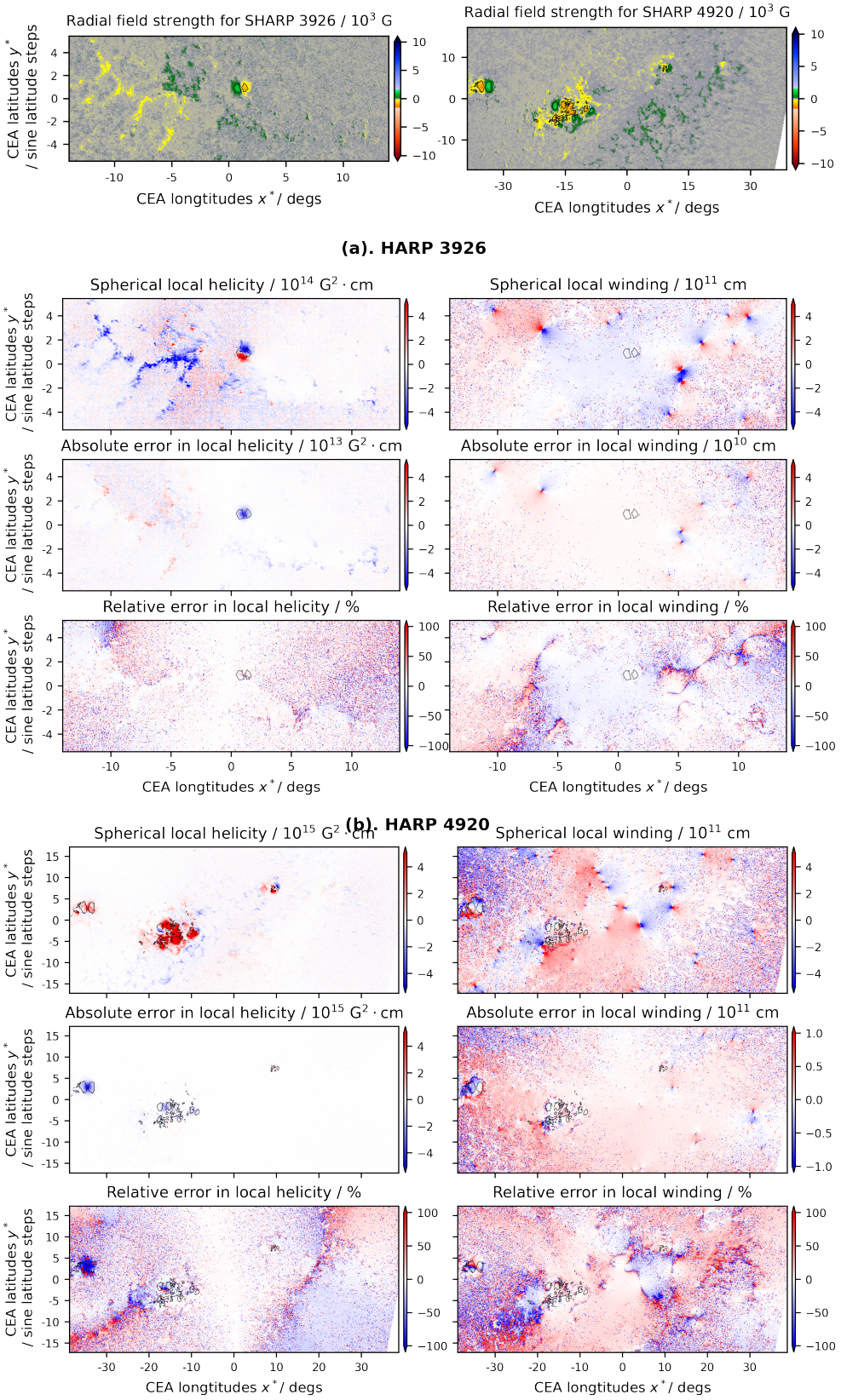

Figure 7.6: Spatial distributions of absolute and relative errors for local helicity $\mathcal{H}^{\mathrm{W}}(\boldsymbol{x};\zeta_0)$ and winding $\mathcal{L}^{\mathrm{W}}(\boldsymbol{x};\zeta_0)$ for (a) SHARP 3926 on 1 April 2014 at 00:00:00, and (b) SHARP 4920 on 20 December 2014 at 00:24:00. For reference, (radial) magnetograms are shown for both SHARP, top left for 3926 and top right for 4920. Contours of constant field strengths are superimposed on all plots, with thresholds ± 450G for 3926 and ± 550G for 4920.

errors for 3926 are moderate - 5% for helicity and 20% for winding. They are more significant for 4920 - around 15% for helicity and 25% for winding. Note that the time series for helicity show smoother variations than those for winding. This is partly because winding, unlike helicity, is not flux-weighted and tends to be dominated by the more variable field components near the polarity inversion line and/or on the patch edges (Prior and MacTaggart 2020).

7.4.3. Correlation Analysis Against Indicators

The results obtained in §7.4.1 and 7.4.2 coincide with the theoretical prediction in §7.2 that errors from the Euclidean approximation of helicity are greater for larger patches and/or those with greater net magnetic flux. In this subsection, we numerically confirm such correlations for a larger sample of SHARP from the year of 2014 (solar maximum) and of 2017 (towards solar minimum), listed in Table 7.4. Indicators related to patch sizes include de-projected patch area (keyword `AREA`) and number of CEA-projected pixels. The unsigned magnetic flux (keyword `USFLUX`) is used.

No.	Date	No.	Date	No.	Date	No.	Date	No.	Date
3535	14.01.01	4166	14.06.01	4718	14.11.01	6972	17.04.01	7110	17.09.01
3586	14.01.15	4218	14.06.15	4781	14.11.15	6983	17.04.15	7131	17.09.15
3668	14.02.01	4272	14.07.01	4851	14.12.01	6994	17.05.01	7144	17.10.01
3711	14.02.14	4328	14.07.15	4900	14.12.15	7010	17.05.15	7161	17.10.15
3779	14.03.01	4379	14.08.01	6894	17.01.01	7030	17.06.01	7169	17.11.01
3824	14.03.15	4440	14.08.15	6910	17.01.15	7045	17.06.15	7189	17.11.15
3894	14.04.01	4477	14.09.01	6930	17.02.01	7058	17.07.01	7192	17.12.01
3978	14.04.15	4530	14.09.15	6949	17.02.14	7075	17.07.15	7204	17.12.15
4042	14.05.01	4591	14.10.01	6952	17.03.01	7096	17.08.01	3926	14.04.01
4097	14.05.15	4655	14.10.15	6966	17.03.16	7107	17.08.16	4920	14.12.20

Table 7.4: The list of SHARP for correlation analysis in Figure 7.8. On each date at midnight, the SHARP with the smallest number and no blank pixels is chosen.

Results are shown in scatter plots in Figure 7.8. While there is an absence of a clear

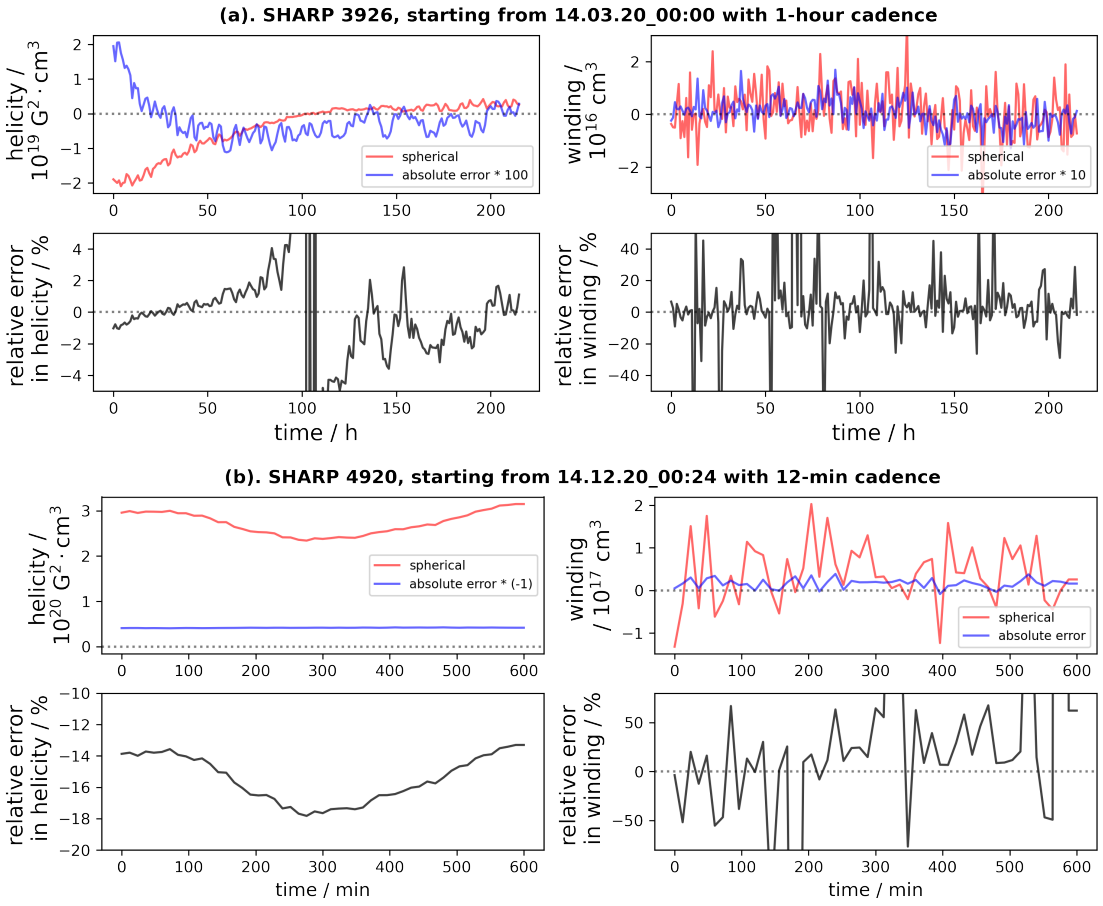

Figure 7.7: Time series of spherical helicity $H^{\mathrm{W}}(r_0)$ and winding $L^{\mathrm{W}}(r_0)$ (both red curves), and corresponding absolute and relative errors (blue and black curves, respectively), for SHARP (a). 3926 and (b). 4920. Note that the absolute errors are suitably scaled both in (a) by a factor of 100 and in (b) by a factor of -1.

correlation for relative errors, absolute errors are strongly correlated with all these indicators. It again demonstrates the necessity to perform helicity and winding computations in the native spherical coordinates for large SHARP (often containing multiple ARs with localised strong magnetic fields).

7.5. Conclusion

Magnetic helicity and winding are of increasing importance in modelling magnetic fields in ARs and predicting extreme solar events. It is necessary to have an unambiguous, accurate, and efficient method for computing both quantities in the native spherical coordinates. The spherical winding and winding helicity are promising candidates with simple and closed-form expressions based only on the observed magnetic fields, allowing direct and meaningful comparisons for configurations with different boundary conditions.

In this case study, by performing helicity and winding computations in both the approximated, Euclidean/CEA approach and the exact, spherical version for SHARP magnetograms, we have quantitatively investigated the extent to which spherical curvature manifests. Persistent and sometimes significant errors are found in both quantities, especially for ARs with large spatial extents or strong fields (usually leading to flares and coronal mass ejections). Also, absolute errors of both quantities seem to correlate strongly with patch sizes and magnetic flux, numerically confirming the predictions in Gary and Hagyard 1990. Since the spherical approach is computationally as efficient as the Euclidean one, it is apparent that the new formalism should be preferred in future studies.

As mentioned in §7.2, we expect errors of similar orders of magnitude in helicity and winding flux computations as they share almost identical forms as helicity and winding densities discussed in this work. However, velocity inversions are needed in flux computations which would potentially involve more uncertainties, since they require more observational data such as Doppler spectrograms in addition to vector magnetograms. A fully spherical formalism for velocity inversions and the incorporation into flux computations are not yet available, which could be a future direction for generalisation.

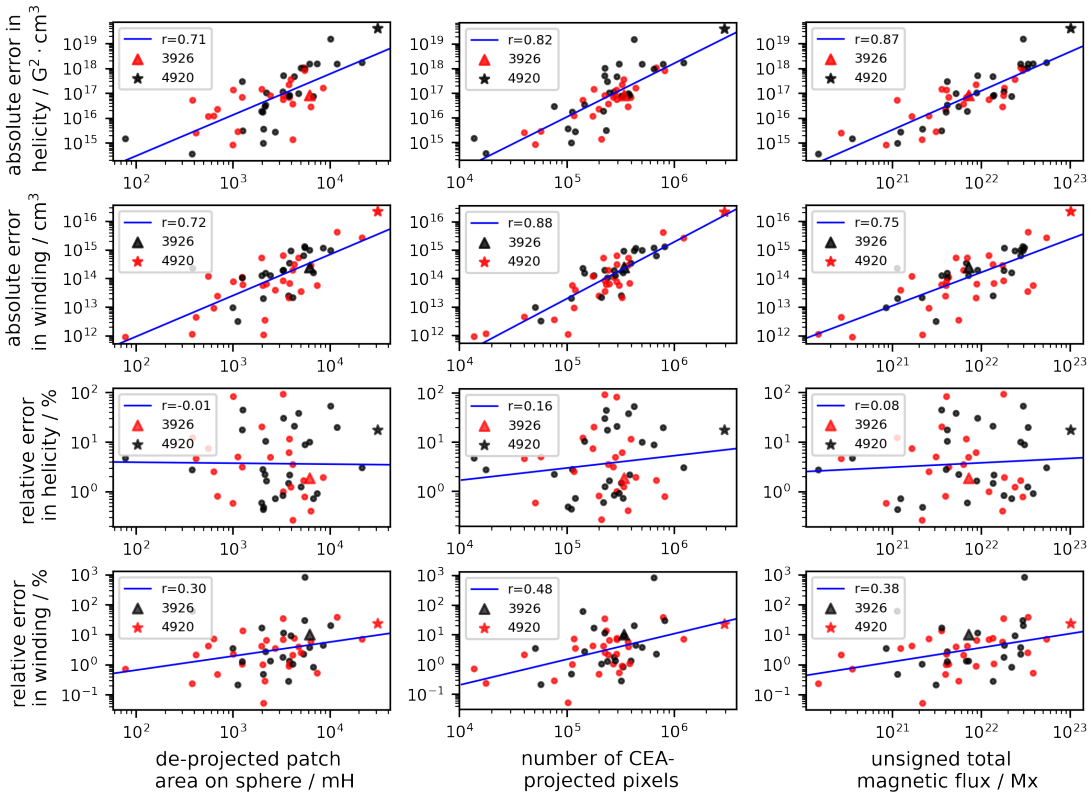

Figure 7.8: Log-log scatter plots of unsigned absolute and relative errors in helicity and winding against potential indicators for a selection of SHARP from 2014 and 2017 (including SHARP 3926 and 4920 used in §7.4.1 and 7.4.2) listed in Table 7.4. Best-fit lines are shown with respective Pearson correlation coefficients or r-values. Colours are used to indicate the actual signs of errors, red for positive and black for negative.

Chapter 8

Possible Future Works

They cannot look out far.
They cannot look in deep.
But when was that ever a bar
To any watch they keep?

— Robert Frost (1874-1963), *Neither Out Far Nor In Deep*

This thesis demonstrated the potential of employing concepts and techniques from mathematics in topological fluid dynamics, i.e., by constructing spherical and periodic winding rates of open curves and proving Theorem 6.1 for spherical and periodic winding (magnetic) helicity. Here, we provide three possible future directions of research that could build on the results from this thesis.

The generalisation of winding rates of open curves to general two-dimensional surfaces would extend the formalism of winding magnetic helicity even further. This could include investigating the shape term proposed in Berger and Hornig 2018 and justifying works such as Prior and Yeates 2021 which involves foliation of possibly highly distorted surfaces.

Despite its success in the modelling and predictions for solar eruptions, helicity is a single number associated with the entire field configuration. It is too coarse-grained for the intricate structures of solar magnetic fields since, for example, it is well-known that a field with vanishing helicity can have a non-trivial topology. The prospects of using

finer-scale measures such as field-line helicity (see e.g. Yeates and Hornig 2016; Yeates and Page 2018) or even its higher-order versions are promising (see e.g., Berger 1990, 2001).

Lastly, discussions of geometric phases have been in focus since the discovery of the Aharonov-Bohm effect (Aharonov and Bohm 1959), Berry's phase (Berry 1984), and Witten's invention of topological quantum field theory (Witten 1988). It is perhaps important to relate the findings in this thesis to a broader perspective in theoretical physics.

Bibliography

Aharonov, Y. and Bohm, D. (1959). "Significance of Electromagnetic Potentials in the Quantum Theory". In: *Phys. Rev.* **115** (3), pp. 485-491.

Alfvén, H. (1942). "Existence of Electromagnetic-Hydrodynamic Waves". In: *Nature* **150**, pp. 405-406.

— (1943). "On the existence of electromagnetic-hydrodynamic waves." In: *Ark. Mat. Astr. Fys.* **29B** (2), pp. 1-7.

— (1950). *Cosmical electrodynamics*. Clarendon Press.

Arfken, G. B. and Weber, H. J. (2005). *Mathematical Methods For Physicists - International Student Edition*. 6th ed. Academic Press.

Arnol'd, V. I. (1974). "The asymptotic Hopf invariant and its applications (in Russian)". In: *Proc. Summer School in Diflerential Equations, Erevan*.

Arnold, V. I. and Khesin, B. A. (1998). *Topological Methods in Hydrodynamics*. Springer New York.

Backus, G. (1958). "A Class of Self-Sustaining Dissipative Spherical Dynamos". In: *Ann. Phys.* **4**, pp. 372-447.

Berger, M. A. (1985). "Topological invariants of field lines rooted to planes". In: *Geophys. Astrophys. Fluid Dyn.* **34** (1-4), pp. 265-281.

— (1990). "Third-order link integrals". In: *J. Phys. A: Math. Gen.* **23**, pp. 2787-2793.

— (1993). "Energy-crossing number relations for braided magnetic fields". In: *Phys. Rev. Lett.* **70** (6), pp. 705-708.

— (1994). "Minimum crossing numbers for 3-braids". In: *J. Phys. A: Math. Gen.* **27**, pp. 6205-6213.

Berger, M. A. (1996). "Magnetic helicity in a periodic domain". In: *J. Geophys. Res.* **102**, pp. 2637-2644.

— (1999). "Introduction to Magnetic Helicity". In: *Plasma Phys. Control. Fusion* **41**, B167.

— (2001). "Topological Invariants in Braid Theory". In: *Lett. Math. Phys.* **55**, pp. 181-192.

Berger, M. A. and Field, G. B. (1984). "The topological properties of magnetic helicity". In: *J. Fluid Mech.* **147**, pp. 133-148.

Berger, M. A. and Hornig, G. (2018). "A generalized poloidal-toroidal decomposition and an absolute measure of helicity". In: *J. Phys. A: Math. Theor.* **51** (49), p. 495501.

Berger, M. A. and Prior, C. B. (2006). "The writhe of open and closed curves". In: *J. Phys. A: Math. Theor.* **39** (26), pp. 8321-8348.

Berry, M. V. (1984). "Quantal phase factors accompanying adiabatic changes". In: *Proc. R. Soc. Lond. A* **392**, pp. 45-57.

Biskamp, D. (2003). *Magnetohydrodynamic Turbulence*. Cambridge University Press.

Bobra, M. G., Sun, X., Hoeksema, J. T., et al. (2014). "The Helioseismic and Magnetic Imager (HMI) Vector Magnetic Field Pipeline: SHARPs - Space-Weather HMI Active Region Patches." In: *Sol. Phys.* **289**, pp. 3549-3578.

Bolker, E. D. (1973). "The Spinor Spanner". In: *Am. Math. Mon.* **80** (9), pp. 977-984.

Borrelli, V. et al. (2012). "Flat tori in three-dimensional space and convex integration". In: *Proc. Natl. Acad. Sci. U.S.A.* **109** (19), pp. 7218-7223.

Brannan, D. A., Esplen, M. F., and Gray, J. J. (1999). *Geometry*. Cambridge University Press.

Buchwald, J. Z. (1994). *The Creation of Scientific Effects: Heinrich Hertz and Electric Waves*. University of Chicago Press.

Calabretta, M. R. and Greisen, E. W. (2002). "Representations of celestial coordinates in FITS". In: *Astron. Astrophys.* **395**, pp. 1077-1122.

Campbell, J. and Berger, M. A. (2014). "Helicity, linking, and writhe in a spherical geometry". In: *J. Phys. Conf. Ser.* **544** (1), p. 012001.

Cantarella, J., DeTurck, D., and Gluck, H. (2001). "The Biot-Savart operator for application to knot theory, fluid dynamics, and plasma physics". In: *J. Math. Phys.* **42** (2), pp. 876-905.

— (2002). "Vector Calculus and the Topology of Domains in 3-Space". In: *Am. Math. Mon.* **109** (5), pp. 409–442.

Cattaneo, F., Bodo, G., and Tobias, S. (2020). "On magnetic helicity generation and transport in a nonlinear dynamo driven by a helical flow". In: *J. Plasma Phys.* **86** (4), p. 905860408.

Challis, L. (2003). "The Green of Green Functions". In: *Phys. Today* **56** (12), pp. 41–46.

Chandrasekhar, S. and Kendall, P. C. (1957). "On Force-free Magnetic Fields". In: *Astrophys. J* **126**, pp. 457–460.

Conway, J. B. (1978). *Functions of One Complex Variable, Volume I*. 1st ed. Springer New York, NY.

Courant, R. and Hilbert, D. (1989). *Methods of Mathematical Physics*. John Wiley & Sons, Ltd.

Crowdy, D. and Cloke, M. (2003). "Analytical solutions for distributed multipolar vortex equilibria on a sphere". In: *Phys. Fluids* **15** (1), pp. 22–34.

Démoulin, P. (2007). "Recent theoretical and observational developments in magnetic helicity studies". In: *Adv. Space Res.* **39**, pp. 1674–1693.

Dombre, T. et al. (1986). "Chaotic streamlines in the ABC flows". In: *J. Fluid Mech.* **167**, pp. 353–391.

Einstein, A. (1905a). "Über einen die Erzeugung und Verwandlung des Lichtes betreffenden heuristischen Gesichtspunkt [On a Heuristic Viewpoint Concerning the Production and Transformation of Light]". In: *Ann. Phys. (Berl.)* **17**, pp. 132–148.

— (1905b). "Zur Elektrodynamik bewegter Körper [On the Electrodynamics of Moving Bodies]". In: *Ann. Phys. (Berl.)* **17**, pp. 891–921.

Enciso, A., Peralta-Salas, D., and Lizaur, F. T. de (2016). "Helicity is the only integral invariant of volume-preserving transformations". In: *Proc. Natl. Acad. Sci. U.S.A.* **113** (8), pp. 2035–2040.

Evans, L. C. (2010). *Partial Differential Equations*. 2nd ed. American Mathematical Society.

Fadell, E. and Buskirk, J. (1962). "The braid groups of E2 and S2". In: *Duke Math. J.* **29** (22), pp. 243–257.

Faraday, M. (1852). "V. Experimental researches in electricity". In: *Phil. Trans. R. Soc.* **122**, pp. 125–162.

Finn, J. H. and Antonsen, T. M. J. (1985). "Magnetic helicity: what is it and what is it good for". In: *Comments on Plasma Phys. Control. Fusion* 3 (9), pp. 111-126.

Gary, A. G. and Hagyard, M. J. (1990). "Transformation of vector magnetograms and the problems associated with the effects of perspective and the azimuthal ambiguity." In: *Sol. Phys.* **126**, pp. 21-36.

Gauss, C. F. (2011). "NACHLASS". In: *Werke*. Vol. V. Cambridge Library Collection - Mathematics. Cambridge University Press, p. 605.

Glasser, M. (1974). "The evaluation of lattice sums. III: Phase modulated sums". In: *J. Math. Phys.* **15** (2), pp. 188-189.

Goncharov, V. and Gryanik, V. (1986). "Dynamics of solitary dissipative vortices: vortex lattices and their stability". In: *Zh. Eksp. Teor. Fiz.* **91**, pp. 1653-1665.

Hatcher, A. (2009). *Algebraic Topology*. Cambridge University Press.

Hawkes, G. and Yeates, A. R. (2019). "Hemispheric injection of magnetic helicity by surface flux transport". In: *Astron. Astrophys.* **631**, A138.

Helmholtz, H. von (1858). "Über Integrale der Hydrodynamische Gleichungen, welche der Wirbelbewegung entsprechen". In: *J. Reine Angew. Math.* **55**, pp. 25-55.

— (1867). "On Integrals of the Hydrodynamical Equations, which Express Vortex-Motion (Translated to English by P. G. Tait)". In: *Lond. Edinb. Dubl. Phil. Mag* **33** (226), pp. 485-512.

Hensley, D. (1994). "The number of lattice points within a contour and visible from the origin". In: *Pac. J. Math.* **166**, pp. 295-304.

Hodge, W. V. D. (1941). *The Theory and Applications of Harmonic Integrals*. Cambridge University Press.

Hoeksema, J. T., Liu, Y., Hayashi, K., et al. (2014). "The Helioseismic and Magnetic Imager (HMI) Vector Magnetic Field Pipeline: Overview and Performance." In: *Sol. Phys.* **289**, pp. 3483-3530.

Hornig, G. (2006). *A Universal Magnetic Helicity Integral*. URL: https://doi.org/10.48550/arXiv.astro-ph/0606694.

Kell, P. (1996). *The Countess of Westmorland's Loadstone*. URL: https://www.mhs.ox.ac.uk/about/sphaera/sphaera-issue-no-4/the-countess-of-westmorlands-loadstone/.

Kudryavtseva, E. A. (2016). "Helicity is the only invariant of incompressible flows whose derivative is continuous in C1-topology". In: *Math. Notes* **99** (4), pp. 611–615.

LaBonte, B., Georgoulis, M., and Rust, D. (2007). "Survey of magnetic helicity injection in regions producing X-class flares". In: *Astrophys. J.* **671** (1), pp. 955–963.

Lambert, J. H. (1759). *Perspective affranchie de l'embarras du plan géometral.*

Lee, J. M. (2019). *Introduction to Riemannian Manifolds.* Springer Cham.

Lin, C. S. and Wang, C. L. (2010). "Elliptic functions, Green functions and the mean field equations on tori". In: *Ann. Math.* **172** (2), pp. 911–954.

Liu, Y. and Schuck, P. W. (2012). "Magnetic energy and helicity in two emerging active regions in the Sun". In: *Astrophys. J.* **761** (2), pp. 105–120.

— (2013). "A Note on Computation of Relative Magnetic-Helicity Flux Across the Photosphere". In: *Sol. Phys.* **283**, pp. 283–294.

Mackay, D. H. and Ballegooijen, A. A. van (2001). "A Possible Solar Cycle Dependence to the Hemispheric Pattern of Filament Magnetic Fields?" In: *Astrophys. J.* **560** (1), pp. 445–455.

MacTaggart, D., Prior, C. B., et al. (2021). "Direct evidence that twisted flux tube emergence creates solar active regions". In: *Nat. Commun.* **12** (1), pp. 1–8.

MacTaggart, D. and Valli, A. (2019). "Magnetic helicity in multiply connected domains". In: *J. Plasma Phys.* **85** (5), p. 775850501.

— (2023). "Relative magnetic helicity in multiply connected domains". In: *J. Phys. A: Math. Theor.* **56**, p. 435701.

MacTaggart, D. and Prior, C. B. (2021). "Helicity and winding fluxes as indicators of twisted flux emergence". In: *Geophys. Astrophys. Fluid Dyn.* **115** (1), pp. 85–124.

Madsen, I. H. and Tornehave, J. (1997). *From Calculus to Cohomology.* Cambridge University Press.

Maxwell, J. C. (1861). "XXV. On physical lines of force". In: *Lond. Edinb. Dubl. Phil. Mag.* **21** (139), pp. 161–175.

— (1865). "VIII. A dynamical theory of the electromagnetic field". In: *Phil. Trans. R. Soc.* **155**, pp. 459–512.

Moffatt, H. K. (2010). "Vortex Dynamics: the Legacy of Helmholtz and Kelvin". In: *IUTAM Symposium on Hamiltonian Dynamics, Vortex Structures, Turbulence*. Ed. by A. Borisov et al. Springer, pp. 1-10.

— (1969). "The degree of knottedness of tangled vortex lines". In: *J. Fluid Mech.* **35** (1), pp. 117-129.

Moffatt, H. K. and Dormy, E. (2019). *Self-Exciting fluid dynamos*. Cambridge University Press.

Moffatt, H. K. and Ricca, R. L. (1992). "Helicity and the Călugăreanu invariant". In: *Proc. R. Soc. A* **439**, pp. 411-429.

Moraitis, K., Pariat, É., Savcheva, A., et al. (2018). "Computation of Relative Magnetic Helicity in Spherical Coordinates". In: *Sol. Phys.* **293**.92.

Moreau, J. J. (1961). "Constantes d'un îlot tourbillonnaire en fluide parfait barotrope". In: *C. r. hebd. séances Acad.* **252**, pp. 2810-2812.

Needham, J. (1959). *Science and Civilisation in China - Volume 3. Mathematics and the Sciences of the Heavens and the Earth*. Cambridge University Press.

Nobel Prize Outreach AB (May 16, 2024). *The Nobel Prize in Physics 1965*. URL: https://www.nobelprize.org/prizes/physics/1965/summary/.

O'Neil, K. (1989). "On the Hamiltonian dynamics of vortex lattices". In: *J. Math. Phys.* **30**, pp. 1373-1379.

Ogilvie, G. I. (2016). "Astrophysical fluid dynamics". In: *J. Plasma Phys.* **82** (3), p. 205820301.

Panagiotou, E. (2015). "The linking number in systems with Periodic Boundary Conditions". In: *J. Comput. Phys.* **300**, pp. 533-573.

Pariat, É., Démoulin, P., and Berger, M. A. (2005). "Photospheric flux density of magnetic helicity". In: *Astron. Astrophys.* **439** (3), pp. 1191-1203.

Pariat, É., Nindos, A., et al. (2006). "What is the spatial distribution of magnetic helicity injected in a solar active region?" In: *Astron. Astrophys.* **452**, pp. 623-630.

Paul, R. (2019). *Lecure Notes on Partial Differential Equations III (Math 423) at Oregon Institute of Technology*. URL: http://math.oit.edu/~paulr/Upper/Math_42x/Math_423/Lectures/GenGreens.pdf.

Pfefferlé, D., Noakes, L., and Perrella, D. (2021). "Gauge freedom in magnetostatics and the effect on helicity in toroidal volumes". In: *J. Math. Phys.* **62** (9), p. 093505.

Poulton, C. G. et al. (1999). "Source-neutral Green's functions for periodic problems in electrostatics, and their equivalents in electromagnetism". In: *Proc. R. Soc. Lond. A.* **455**, pp. 1107–1123.

Priest, E. (2014). *Magnetohydrodynamics of the Sun*. Cambridge University Press.

Prior, C. B. and MacTaggart, D. (2020). "Magnetic winding: what is it and what is it good for?" In: *Proc. R. Soc. A* **476**, p. 20200483.

Prior, C. B. and Yeates, A. R. (2014). "On the helicity of open magnetic fields". In: *Astrophys. J.* **787** (2), pp. 100–112.

— (2021). "Intrinsic winding of braided vector fields in tubular subdomains". In: *J. Phys. A: Math. Theor.* **54**, p. 465701.

Raphaldini, B., Prior, C. B., and MacTaggart, D. (2022). "Magnetic Winding as an Indicator of Flare Activity in Solar Active Regions". In: *Astrophys. J.* **927** (2), pp. 156–179.

Reusken, A. (2018). "Stream function formulation of surface Stokes equations". In: *IMA J. Numer. Anal.* **40** (1), pp. 109–139.

Ricca, R. L. and Nipoti, B. (2011). "Gauss' linking number revisited". In: *J. Knot Theory Ramif.* **20** (10), pp. 1325–1343.

Rice, O. E. K. and Yeates, A. R. (2023). "Eruptivity Criteria for Solar Coronal Flux Ropes in Magnetohydrodynamic and Magnetofrictional Models". In: *Astrophys. J.* **955** (2), pp. 114–129.

Riemann, B. (2013). "Grundlagen für eine allgemeine Theorie der Functionen eiuer veränderlichen complexen Grösse (1851)". In: *Bernard Riemann's Gesammelte Mathematische Werke Und Wissenschaftlicher Nachlass*. Ed. by R. Dedekind and H. M. Weber. Cambridge Library Collection - Mathematics. Cambridge University Press. Chap. 1, pp. 3–47.

Schleifer, N. (1983). "Differential forms as a basis for vector analysis—with applications to electrodynamics". In: *Am. J. Phys.* 12 (51), pp. 1139–1145.

Schuck, P. W. and Antiochos, S. K. (2019). "Determining the Transport of Magnetic Helicity and Free Energy in the Sun's Atmosphere". In: *Astrophys. J.* **882** (2), pp. 151–174.

Schuck, P. W. (2008). "Tracking vector magnetograms with the magnetic induction equation". In: *Astrophys. J.* **683** (2), pp. 1134–1152.

Sheffield, J. (1994). "The physics of magnetic fusion reactors". In: *Rev. Mod. Phys.* **66** (3), pp. 1015–1103.

Soós, S. et al. (2022). "On the differences in the periodic behavior of magnetic helicity flux in flaring active regions with and without X-class events". In: *Astrophys. J.* **925** (2), pp. 129–140.

Stern, D. P. (2002). "A Millennium of Geomagnetism". In: *Rev. Geophys.* **40** (3), pp. 1-1–1–30.

Sun, X. (2022). "On the Coordinate System of Space-Weather HMI Active Region Patches (SHARPs): A Technical Note". In: DOI: 10.48550/arXiv.1309.2392.

Sutherland, W. A. (2009). *Introduction to metric and topological spaces*. 2nd ed. Oxford University Press.

Thalmann, J. K., Dumbović, M., et al. (2023). "Tracking magnetic flux and helicity from the Sun to Earth - Multi-spacecraft analysis of a magnetic cloud and its solar source". In: *Astron. Astrophys.* **669**, A72.

Thalmann, J. K., Moraitis, K., Linan, L., et al. (2019). "Magnetic helicity budget of solar active regions prolific of eruptive and confined flares". In: *Astrophys. J.* **887** (1), pp. 64–71.

Vemareddy, P. (2019). "Very fast helicity injection leading to critically stable state and large eruptive activity in solar active region NOAA 12673". In: *Astrophys. J.* **872** (2), pp. 182–197.

Whittaker, E. T. and Watson, G. N. (1996). *A Course of Modern Analysis*. 4th ed. Cambridge University Press.

Witten, E. (1988). "Topological quantum field theory". In: *Comm. Math. Phys.* **117** (3), pp. 353–386.

Woltjer, L. (1958). "A theorem on force-free magnetic fields". In: *Proc. Natl. Acad. Sci. U.S.A.* **44** (6), pp. 489–491.

Wyper, P., Antiochos, S., and DeVore, C. (2017). "A universal model for solar eruptions". In: *Nature* **544**, pp. 452–455.

Xiao, D., Prior, C. B., and Yeates, A. R. (2023a). "Spherical winding and helicity". In: *J. Phys. A: Math. Theor.* **56**, p. 205201.

— (2023b). "Computation of Winding-Based Magnetic Helicity and Magnetic Winding Density for SHARP Magnetograms in Spherical Coordinates". In: *Solar Phys.* **298**, p. 116.

— (2024). "Winding and Magnetic Helicity in Periodic Domains". In: *(under review)*.

Yang, K. E., Wheatland, M. S., and Gilchrist, S. A. (2020). "Relative Magnetic Helicity Based on a Periodic Potential Field". In: *Astrophys. J.* **894** (2), pp. 151–162.

Yang, S., Zhang, H., and Büchner, J. (2009). "Magnetic helicity accumulation and tilt angle evolution of newly emerging active regions". In: *Astron. Astrophys.* **502** (1), pp. 333–340.

Yeates, A. R. (2020). "The minimal helicity of solar coronal magnetic fields". In: *Astrophys. J. Lett.* **898**.L49 (2).

Yeates, A. R. and Hornig, G. (2016). "The global distribution of magnetic helicity in the solar corona". In: *Astron. Astrophys.* **594**.A98.

Yeates, A. R., Mackay, D. H., and van Ballegooijen, A. A. (2008). "Modelling the Global Solar Corona II: Coronal Evolution and Filament Chirality Comparison". In: *Sol. Phys.* **247** (1), pp. 103–121.

Yeates, A. R. and Page, M. H. (2018). "Relative field-line helicity in bounded domains". In: *J. Plasma Phys.* **84** (6), p. 775840602.

Yi, S. and Choe, G. S. (2022). "The toroidal field surfaces in the standard poloidal-toroidal representation of magnetic field". In: *Sci. Rep.* **12**, p. 2944.